# Development of high-damage threshold dispersive coatings

**Ivan B. Angelov**

München 2014

# Development of high-damage threshold dispersive coatings

**Ivan B. Angelov**

Dissertation
an der Fakultät für Physik
der Ludwig–Maximilians–Universität
München

vorgelegt von
Ivan B. Angelov
aus Stara Zagora, Bulgarien

München, den 19.05.2014

Erstgutachter: Prof. Dr. Ferenc Krausz
Zweitgutachter: Prof. Dr. Norbert Kaiser
Tag der mündlichen Prüfung: 09.07.2014

*To my parents*

# Contents

**Zusammenfassung** xv

**Summary** xvii

**List of Publications** xix

**1 Introduction** 1

1.1 Motivation . . . 1
1.2 Background . . . 2
1.3 Goal . . . 3
1.4 Outline . . . 3

**2 Ultrashort pulse propagation in transparent media** 5

2.1 Linear propagation and dispersion . . . 5
2.2 Propagation in multilayer thin-films . . . 7
  2.2.1 Characteristic matrix . . . 8
  2.2.2 Electric field distribution . . . 9
2.3 Optical breakdown . . . 9
  2.3.1 Photoionization . . . 10
  2.3.2 Impact ionization . . . 11

**3 Dispersion control and measurement** 13

3.1 Resonant storage and wavelength-dependent penetration . . . 14
3.2 Resonance scanning interferometer for dispersion measurements . . . 16
  3.2.1 Experimental set-up . . . 18
  3.2.2 Theory . . . 19
  3.2.3 Experimental results . . . 22
3.3 Conclusion . . . 26

**4 Mirror characterization techniques** 29

4.1 Spectrophotometry . . . 29
4.2 Ring-down method for measurement of total losses . . . 30

4.3 Calorimetric absorption measurements . . . . . . . . . . . . . . . . . . . . 31

**5 Damage threshold metrology 33**

5.1 Set-up scheme . . . . . . . . . . . . . . . . . . . . . . . . . . . . . . . 33
5.2 Measurement algorithm and definition of damage . . . . . . . . . . . . . 34
5.3 Calibration . . . . . . . . . . . . . . . . . . . . . . . . . . . . . . . . . 35
5.4 Focus characterization . . . . . . . . . . . . . . . . . . . . . . . . . . . 36
5.5 Calculation of peak fluence . . . . . . . . . . . . . . . . . . . . . . . . 37
5.6 Measurement example . . . . . . . . . . . . . . . . . . . . . . . . . . . 38

**6 Femtosecond optical breakdown of dispersive coatings 41**

6.1 Samples . . . . . . . . . . . . . . . . . . . . . . . . . . . . . . . . . . . 42
6.2 Set-up . . . . . . . . . . . . . . . . . . . . . . . . . . . . . . . . . . . . 43
6.3 Results and discussion . . . . . . . . . . . . . . . . . . . . . . . . . . . 45
  6.3.1 Single layer depositions . . . . . . . . . . . . . . . . . . . . . . . 45
  6.3.2 Dispersive mirrors versus their high-index materials . . . . . . . . 45
  6.3.3 QWOT stacks versus their high-index materials . . . . . . . . . . . 47
  6.3.4 Metal versus dielectric mirrors . . . . . . . . . . . . . . . . . . . . 49
  6.3.5 Precision of the damage threshold measurements . . . . . . . . . . 50
6.4 Conclusion . . . . . . . . . . . . . . . . . . . . . . . . . . . . . . . . . 50

**7 Picosecond optical breakdown at MHz and kHz rates 53**

7.1 Samples . . . . . . . . . . . . . . . . . . . . . . . . . . . . . . . . . . . 54
7.2 Measurement set-up and laser sources . . . . . . . . . . . . . . . . . . . 56
7.3 Results and discussion . . . . . . . . . . . . . . . . . . . . . . . . . . . 59
7.4 Conclusion . . . . . . . . . . . . . . . . . . . . . . . . . . . . . . . . . 65

**8 Conclusion and outlook 67**

**A Fluence of a Gaussian Pulse 71**

A.1 Peak intensity . . . . . . . . . . . . . . . . . . . . . . . . . . . . . . . . 71
A.2 Peak fluence . . . . . . . . . . . . . . . . . . . . . . . . . . . . . . . . . 72

**B Data Archiving 75**

**Bibliography 78**

**List of Acronyms 89**

**Acknowledgments 91**

# List of Figures

3.1 Dispersion via wavelength-dependent penetration (a) and resonant storage (b) . . . 14
3.2 Structure of a broadband high-dispersive mirror. . . . 15
3.3 Typical electric field distribution inside of the layer stack of a dispersive mirror 16
3.4 Michelson-type white-light interferometer for dispersion measurements . . . 17
3.5 Schematic representation of the resonant scanning interferometer (a) in transmission- and (b) in reflection mode (reprinted from [102]). . . . 19
3.6 Merging data from measurements with different spacer thicknesses into a combined grid. (Reprinted from [102]) . . . 21
3.7 (a) and (b): GD and GDD measured using RSI in transmission (green curves) compared to WLI results (red curves) and theoretical data (orange curves). (c) and (d): Comparison of GD and GDD data obtained using RSI in reflection (red curves) and in transmission (green curves). . . . 23
3.8 RSI measurement of dispersion of a broadband dispersive mirror. . . . 25
3.9 (a) and (b): GD and GDD results in a wide range from 940 nm to 1100 nm obtained using WLI (red curves) and RSI (green curves) are compared to theoretical data (orange curves). (c) and (d): Similarly, for the narrower range from 1000 nm to 1040 nm. . . . 26

4.1 Example spectrophotometric measurement of the transmission of a QWOT stack (green curve) and a mirror optimized for electric field distribution (EFI) – orange curve. . . . 30
4.2 Example calorimetric measurement of absorption. The average power (green curve) and the temperature (red curve) are recorded as functions of time. Two exponential functions (blue dash-dot curve) are fitted to the measurement data: one when the the sample was illuminated with the laser beam and another after the beam was blocked. . . . 31

5.1 General scheme of a damage threshold set-up. PD1 – calibrated photodiode; PD2 – photodiode to measure scattered light; 3D – three dimensional translation stage. . . . 33

5.2 Damage detection by monitoring the scattered: (a) non-damaged site and low scattering; (b) damaged site, causing increased scattering. . . . . . . . 34
5.3 Scattering signal versus fluence: example damage threshold measurement. The arrow points to the fluence at which damage occurred. . . . . . . . . . 35
5.4 Example calibration measurement of the photodiode, allowing consequent *in situ* measurements of incident power. . . . . . . . . . . . . . . . . . . . . 36
5.5 Measurement of the beam width across one of the foci. The experimental data was fitted with the Gaussian beam width $w(z)$ as a function of the axial distance $z$ (Eqn. 5.2). . . . . . . . . . . . . . . . . . . . . . . . . . . 37

6.1 Layout of the set-up: F – gradient neutral density filter wheel; BS – beam splitter; L – 1500 mm convex lens; PD1 – calibrated photodiode; PD2 – photodiode to detect scattered light; TS – 3D translation stage (reprinted from [119]). . . . . . . . . . . . . . . . . . . . . . . . . . . . . . . . . . 43
6.2 Layout of the relevant part of the PFS front end system (shortened from [120]). 44
6.3 Threshold fluences of single layer depositions and fused silica substrate. . . 46
6.4 Damage threshold comparison between single layer coatings with the dispersive coatings employing the respective high-index material. . . . . . . . 47
6.5 Threshold fluences of QWOTs compared to that of single layer depositions of different high-refractive index materials. . . . . . . . . . . . . . . . . . . 48
6.6 Comparison between the threshold fluences of metal and dielectric mirrors. 49

7.1 (a) and (b): Layer thickness profile of a QWOT stack of $Ta_2O_5/SiO_2$ (a) and of a layer stack of $Ta_2O_5/SiO_2$ with reduced electric field intensity (EFI) inside the $Ta_2O_5$ layers (b). (c) and (d): Electric field distributions inside of (a) and (b), respectively. The electric field inside $L$ and $H$ layers is represented accordingly by green and red sections, whereas the field in the incident medium is colored in blue. . . . . . . . . . . . . . . . . . . . . . . 55
7.2 Absorption and total losses of the QWOT stacks, on which damage threshold measurements were performed. . . . . . . . . . . . . . . . . . . . . . . . . 56
7.3 Measurement set-up: PD – photodiode, $\lambda/2$ – half-wave plate, TFP – thin-film polarizer. . . . . . . . . . . . . . . . . . . . . . . . . . . . . . . . . . 57
7.4 Autocorrelation trace of a pulse generated by 11.5 MHz mode-locked Yb:YAG thin-disk oscillator. (Reprinted from [49]) . . . . . . . . . . . . . . . . . . 58
7.5 Temporal intensity profile (green color) and temporal phase (orange dashed curve) of the pulses generated by the kHz laser system measured using a FROG technique [130]. The green dots represent measurement data, and the green curve is a Gaussian fit. . . . . . . . . . . . . . . . . . . . . . . . . 59
7.6 Damage fluences of different QWOT stacks versus band gap of the respective high-index materials. . . . . . . . . . . . . . . . . . . . . . . . . . . . . . 60

7.7 Damage threshold values of QWOT stacks and NBP filters made of different high-index materials . . . . . . . . . . . . . . . . . . . . . . . . . . . . . . . . . . 62

7.8 Damage threshold values of EFI and QWOT stacks measured: (a) at MHz repetition rate and (b) at kHz repetition rate. . . . . . . . . . . . . . . . . . . 63

7.9 Theoretical GDD of a QWOT stack and an EFI design around the central wavelength. . . . . . . . . . . . . . . . . . . . . . . . . . . . . . . . . . . . . 64

7.10 Comparison of LOT and QWOT designs made with $TiO_2$ as high-index material. . . . . . . . . . . . . . . . . . . . . . . . . . . . . . . . . . . . . . 65

# List of Tables

6.1 General description and breakdown threshold fluences of the studied samples. The given thicknesses are physical. . . . . . . . . . . . . . . . . . . . . . 42
6.2 Band gap energies ($E_g$) and refractive indices at 800 nm ($n_0$) of the investigated materials. . . . . . . . . . . . . . . . . . . . . . . . . . . . . . . . . . . 45

7.1 General description of samples studied with picosecond pulses . . . . . . . 54

# Zusammenfassung

Vielschichtige Spiegel sind grundlegende Komponenten jedes ultraschnellen Lasersystems. Die Pulsenergie aktueller ultraschneller Hochleistungslaser wird oft durch laserinduzierte Zerstörung der optischen Beschichtungen limitiert. Eine Möglichkeit, dieses Problem zu bewältigen, ist eine Vergrößerung des Laserstrahldurchmessers. Dies ist jedoch in der Regel unerwünscht, da es die Kosten und die Grundfläche des Lasersystems erhöht. Eine Verbesserung der Lichtbeständigkeit der Vielschichtspiegel ist daher für die Entwicklung von kostengünstigen und platzsparenden Lasern von entscheidender Bedeutung. Dies erfordert ein genaues Verständnis des optischen Zerstörungsmechanismus.

In dieser Arbeit haben wir den ultraschnellen optischen Durchbruch dispersiver Spiegel und anderer vielschichtiger Dünnfilme in drei verschiedenen Regimes untersucht: (i) bei 500 Hz Wiederholrate mit 30 fs-Pulsen bei 800 nm Zentralwellenlänge; (ii) bei 11.5 MHz Wiederholrate mit 1 ps-Pulsen bei 1030 nm und (iii) bei 5 kHz Wiederholrate mit 1.4 ps-Pulsen bei 1030 nm. Zusätzlich wurde eine neue Methode für Dispersionsmessungen entwickelt.

Im Femtosekundenregime waren die untersuchten Proben sowohl einschichtige Beschichtungen aus Au, Ag, $Nb_2O_5$, $SiO_2$ und $Ta_2O_5$, sowie $Ta_2O_5/SiO_2$ Mischungen, als auch verschiedene dispersive Spiegel, bestehend aus $SiO_2$ und entweder $Nb_2O_5$, $Ta_2O_5$ oder $HfO_2$. Wir haben ebenfalls einen Ansatz vorgeschlagen, um die Zerstörschwelle von dielektrischen Dünnfilmbeschichtungen zu erhöhen.

Der ultraschnelle optische Durchbruch vielschichtiger Dünnfilme wurde bei einer MHz Wiederholrate und hoher Durchschnittsleistung untersucht. Die optische Zerstörschwelle von drei verschiedenen Arten von Beschichtungen wurde gemessen. Alle Proben wurden entweder mit $TiO_2$, $Ta_2O_5$, $HfO_2$ oder $Al_2O_3$ als hochbrechendem Material und mit $SiO_2$ als Material mit niedrigem Brechungsindex beschichtet. Die gleichen Proben wurden auch bei kHz Wiederholrate vermessen und die Ergebnisse wurden direkt miteinander verglichen. Die Abhängigkeit der Zerstörschwelle von der Bandlücke war in beiden Fällen linear, jedoch war die Abhängigkeit bei einer kHz Wiederholrate steiler als bei einer MHz Wiederholrate. Dies ist eine interessante Feststellung, die weiter untersucht werden soll.

Die entwickelte Methode für Dispersionsmessungen basiert auf der Lokalisierung von Resonanzspitzen in einem Fabry-Pérot-Interferometer. Wir waren in der Lage, eine höhere Auflösung im Vergleich zur konventionellen Methode zu erhalten.

# Summary

Whether it is to form an optical cavity, to control dispersion, or merely to transport the laser beam, multilayer mirrors are fundamental components of every ultrafast laser system. The performance of current state of the art ultrafast high-power lasers in terms of pulse energy is often restrained by optical breakdown of multilayer coatings. One way to overcome this problem is to increase the size of the laser beam, but this is usually undesirable, as it rises the costs and the footprint of the laser system. Therefore, increasing the optical resistance of multilayer mirrors is essential to the development of cost- and space-efficient lasers. In turn, this requires a thorough understanding of the mechanisms behind optical damage.

In this work, we have studied the ultrafast optical breakdown of dispersive mirrors, as well as that of other multilayer thin-films, in three different regimes: (i) at 500 Hz repetition rate with 30 fs pulses, at a central wavelength of 800 nm; (ii) at 11.5 MHz repetition rate with 1 ps pulses, at 1030 nm; (iii) at 5 kHz repetition rate with 1.4 ps pulses at 1030 nm. The results from (ii) and (iii) have been compared side by side. In addition, a novel technique for dispersion measurements has been developed.

In the femstosecond regime, the samples have been: single layer coatings made of $\mathrm{Au}, \mathrm{Ag}, \mathrm{Nb_2O_5}, \mathrm{SiO_2}, \mathrm{Ta_2O_5}$ and mixtures of $\mathrm{Ta_2O_5}$ with silica in different concentrations; and different dispersive coatings, consisting of $\mathrm{SiO_2}$ as the low-index material and different high-index materials $(\mathrm{Nb_2O_5}, \mathrm{Ta_2O_5}, \mathrm{HfO_2})$. We have also given a suggestion as to what is the best approach to increase the damage threshold of thin-film dielectric coatings.

The ultrafast optical breakdown of multilayer thin-films has been investigated at MHz repetition rate and high average power. The optical breakdown threshold of three different types of coatings has been measured. All samples have been coated with either $\mathrm{TiO_2}$, $\mathrm{Ta_2O_5}$, $\mathrm{HfO_2}$, or $\mathrm{Al_2O_3}$ as high-index material and with $\mathrm{SiO_2}$ as low-index material. The same samples have been measured also at kHz repetition rate. The results obtained in both regimes have been compared. The band gap dependencies of damage threshold in both cases were linear. However, the one retrieved at kHz rate was steeper than its MHz counterpart. This is an interesting finding, which must be investigated further.

The developed method for dispersion measurements has been based on the location of resonance peaks in a Fabry-Pérot-type of interferometer. By simultaneously processing data obtained at different spacer thicknesses, we were able to obtain superior resolution compared to the conventional method.

# List of Publications

Most of the results presented in this thesis have been published in peer reviewed journals and presented at international conferences. The rest will be published in the near future.

## Journal articles

- **I. B. Angelov**, M. K. Trubetskov, V. S. Yakovlev, M. Gorjan, H. Barros, F. Krausz, V. Pervak, *Comparative study of ultrashort pulse laser-induced damage at kHz and MHz repetition rates*, (in preparation)
  *Contribution*: designed the experiment, prepared samples, performed measurements, analysed and discussed the results.
- V. Pervak, O. Razskazovskaya, **I. B. Angelov**, K. L. Vodopyanov, M. Trubetskov. *Dispersive mirror technology for ultrafast lasers in the range 220–4500 nm*. Adv. Opt. Techn. **3**, 55–63 (2014)
  *Contribution*: designed and characterized mirrors.
- **I. B. Angelov**, M. Pechmann, M. K. Trubetskov, F. Krausz, V. Pervak. *Optical breakdown of multilayer thin-films induced by ultrashort pulses at MHz repetition rates*. Opt. Express **21**, 31453–31461 (2013)
  *Contribution*: designed the experiment, prepared samples, performed measurements, analysed and discussed the results.
- M. K. Trubetskov, M. Pechmann, **I. B. Angelov**, K. L. Vodopyanov, F. Krausz, V. Pervak. *Measurements of the group delay and the group delay dispersion with resonance scanning interferometer*. Opt. Express **21**, 6658–6669 (2013)
  *Contribution*: performed measurements, analysed and discussed the results.
- T. Amotchkina, M. Trubetskov, A. Tikhonravov, **I. B. Angelov**, V. Pervak. *Reliable optical characterization of e-beam evaporated TiO2 films deposited at different substrate temperatures*. Appl. Opt. **53**, A8 (2013)
  *Contribution*: prepared and characterized samples, discussed the results.
- V. Pervak, O. Pronin, O. Razskazovskaya, J. Brons, **I. B. Angelov**, M. K. Trubetskov, A. V. Tikhonravov, F. Krausz. *High-dispersive mirrors for high power applications*. Opt. Express **20**, 4503 (2012)
  *Contribution*: characterized samples, discussed the results.

- **I. B. Angelov**, A. Conta, S. A. Trushin, Z. Major, S. Karsch, F. Krausz, V. Pervak. *Investigation of the laser-induced damage of dispersive coatings.* In Proceedings of SPIE, Vol. 8190, 81900B (2011). Edited by G. J. Exarhos, V. E. Gruzdev, J. A. Menapace, D. Ristau, and M. J. Soileau
  *Contribution*: characterized samples, performed measurements, analysed and discussed the results.

# Oral talks

**I. B. Angelov**, M. Pechmann, M. K. Trubetskov, O. Pronin, F. Krausz, V. Pervak, *Damage threshold of multilayer thin-films at MHz repetition rates*, Pacific Rim Laser Damage, Shanghai, China, 19-22 May 2013.
**I. B. Angelov**, A. Conta, S. A. Trushin, Z. Major, S. Karsch, F. Krausz, V. Pervak, *Investigation of the laser-induced damage of dispersive coatings*, Laser Damage, Boulder, Colorado, USA, 19-21 September 2011.

# Other conference contributions

V. Pervak, M. K. Trubetskov, M. Pechmann, **I. B. Angelov**, O. Razskazovskaya, E. Fedulova, K. L. Vodopyanov, F. Krausz. *Measurements of the group delay dispersion with resonance scanning interferometer.* In Conference on Lasers and Electro-Optics Pacific Rim (CLEO-PR),, pp. 1–2 (2013)
M. K. Trubetskov, M. Pechmann, **I. B. Angelov**, E. Fedulova, F. Krausz, V. Pervak. *Group Delay Dispersion Measurements with Resonance Scanning Interferometry.* In Optical Interference Coatings, WD–3 (2013). ISBN: 978-1-55752-970-1
M. K. Trubetskov, M. Pechmann, **I. B. Angelov**, E. Fedulova, F. Krausz, V. Pervak. *Resonance Scanning Interferometer for Group Delay Dispersion Measurements.* In Conference on Lasers and Electro-Optics Europe (CLEO Europe), (2013)
O. Pronin, M. Seidel, J. Brons, F. Lücking, **I. B. Angelov**, V. L. Kalashnikov, V. Pervak, A. Apolonski, T. Udem, F. Krausz. *Towards CEP stabilized, high-power, few cycle pulses from a KLM Yb:YAG thin-disk laser.* In Conference on Lasers and Electro-Optics Europe (CLEO Europe), (2013)
O. Pronin, M. Seidel, J. Brons, F. Lücking, C. Grasse, **I. B. Angelov**, V. Pervak, G. Boehm, M.-C. Amann, V. L. Kalashnikov, T. Udem, A. Apolonski, F. Krausz. *Towards CEP-stabilized, high-power, few-cycle pulses from a KLM Yb:YAG disk laser.* In Ultrafast Optics IX,, (2013)
T. Amotchkina, M. K. Trubetskov, A. V. Tikhonravov, **I. B. Angelov**, V. Pervak. *Reliable characterization of e-beam evaporated TiO2 films.* In Optical Interference Coatings, FA.6 (2013). ISBN: 978-1-55752-970-1

# Chapter 1

# Introduction

## 1.1 Motivation

The first motion picture ever made has been recorded to study a phenomenon, which is too fast for the human eye to resolve, namely the motion of a galloping horse [1]. Another example of the early attempts of temporally resolving fast phenomena is the idea underlying modern pump-probe spectroscopy, which has been developed in the nineteenth century to study shock waves [2]. However, observing the temporal evolution of ever faster processes requires shorter and shorter light pulses. The invention of the laser [3–5] has marked a major breakthrough in that respect by making nanosecond pulses feasible. Only two decades later, the first ultrashort pulses have been generated [6] by passive mode-locking of dye lasers [7, 8], opening the door to ultrafast optics [9].

Today, ultrafast lasers are a versatile tool not only in science, but they also have many industrial as well as medical applications [9]. Ultrashort pulses have allowed scientists to explore ultrafast relaxation processes in the microcosm [10–12]. Few-cycle pulses have enabled time-resolved studies of molecular dynamics [13]. However, it has been attosecond pulses [14, 15] that have opened the door to real-time observations of electron dynamics in molecules and atoms [16, 17]. More recently, researchers have also successfully used the optical field of ultrashort pulses to induce and control electric current in dielectrics [18–20]. Furthermore, currently the feasibility of using laser-driven ion accelerators as ion sources for cancer therapy is under active investigation [21–24]. This is promising, because the high peak intensities accessible by focusing energetic ultrashort pulses allow for more efficient energy transfer from laser photons to ions [25–27].

One of the major challenges in generation of ultrashort pulses is that it demands a laser beam with broad electromagnetic spectrum, the components of which have to be in phase with each other in order to form and maintain the shape of the pulse and its duration [28]. That in turn means that the spectral phase of the pulse has to be accurately controlled and the dispersion gained during propagation through a dispersive medium has to be compensated.

A variety of different techniques for dispersion compensation exist. Most of them are either based on diffraction gratings [29], prism pairs [30], dispersive mirrors [31–34], or on a combination thereof [28, 35]. Each technique has its own advantages and disadvantages. For instance, using prisms and gratings, large amounts of dispersion can be obtained, but they are difficult to align and have relatively low efficiency. In addition, they might fail to compensate the spatial chirp that they introduce, and they might insert higher order dispersion. Both of these effects are generally highly undesirable. Dispersive mirrors, on the other hand, can control second- as well as higher order dispersion of broadband pulses with high precision and efficiency. Additionally, they are also easier to align. However, dispersive mirrors can only introduce moderate, bandwidth-dependent amount of dispersion per reflection [36]. Nevertheless, dispersive mirrors are often preferred due to: (i) relative alignment simplicity [37], (ii) ability to control dispersion over a broad spectral range [38, 39], and (iii) low losses for narrow-band applications [37, 40].

Aside from generating ever shorter pulses, the ultrafast optics community strives to achieve ever higher pulse energies at high repetition rates. Recently developed oscillators and amplifiers, based on fiber [41], innoslab [42, 43], and thin-disk technology [44–46], are capable of generating subpicosecond pulses with energies of several tens of µJ at repetition rates of more than 10 MHz, resulting in several hundreds of watts of average output power and multiple megawatts of peak power. Optical damage is among the challenges towards scaling up the power of such systems. Moreover, their output is often intensified further in regenerative amplifiers [47], optical parametric amplification (OPA) stages [48, 49], and inside enhancement cavities [50, 51]. The latter can reach average intracavity power of several tens of kW, which is limited by the damage threshold of optical coatings [50, 52].

One of the weak spots of ultrafast laser systems with respect to laser-induced damage are the optical multilayer mirrors. The straightforward way to deal with optical breakdown is to increase the beam size. However, that requires larger optics and increases the overall footprint of the system, thereby rising the costs substantially. In addition, the larger the size of the optics, the more difficult it becomes to provide uniform surface quality. Furthermore, the damage threshold of the whole optical element is as low as the damage threshold of its weakest spot. Thus, before undertaking the approach of increasing the size of the optical components, it would be beneficial first to try to increase their damage threshold. A study of the processes governing laser damage is prerequisite to such attempts.

## 1.2 Background

In fact, the history of research on laser-induced damage is almost as old as has the history of laser itself [53]. The optical breakdown induced by nanosecond pulses has been the subject of extensive research over many years [53–62] and is still investigated today because of the great variety of industrial applications of nanosecond lasers.

Similarly, the advance of ultrafast lasers has motivated considerable research on ultrashort pulse optical breakdown of both thin-films and bulk dielectrics [60, 62–76]. All of them have been carried out by measuring the laser-induced damage threshold (LIDT) at a low average power, either in single-shot mode or by using a pulse train at a kHz repetition rate. In addition, few studies on LIDT of dispersive mirrors exist. However, as discussed above, the generation of ultrashort pulses often involves dispersive mirrors, and there are many modern applications, which require sources of high energy ultrashort pulses at high repetition rate. This calls for more research on optical breakdown of dispersive mirrors with ultrashort pulses, and at kHz as well as at MHz rates. This work is thus an attempt to address that knowledge gap.

## 1.3 Goal

The goal of this thesis is twofold. First, to investigate the ultrashort pulse optical breakdown of dispersive mirrors, and thereby to provide a rough estimation of how much the LIDT of a dispersive mirror could be increased. Second, to examine the laser damage of multilayer thin-films induced by ultrashort pulses in the previously unexplored regime of µJ pulses at MHz repetition rate and therefore high average power (tens of watts). Additionally, it was important also to compare the results obtained at MHz rate with measurements at kHz rate, while keeping all other measurement parameters akin. To meet these goals, two distinct set-ups were used with three different laser sources.

## 1.4 Outline

The thesis begins with a short theoretical introduction in Chapter 2. The linear propagation of light in uniform dispersive media is described and the term ‘dispersion’ is introduced in Section 2.1, followed by a description of the linear propagation of light in layered media, i.e. in thin-films (Section 2.2). The Chapter concludes with Section 2.3, giving the currently accepted theoretical picture of optical ionization, the process immediately preceding ultrashort pulse laser damage.

Chapter 3 provides in Section 3.1 a brief introduction to the workings of dispersive mirrors. Section 3.2 gives a thorough description of a novel technique for measurements of dispersion of mirrors. Theoretical and experimental details of the method are given, as well as few examples demonstrating its advantages over the currently widely adopted approach. This method was developed partially to facilitate the characterization of the dispersive mirrors investigated later for LIDT. Further techniques to characterize the samples under investigation are described in Chapter 4.

The two set-ups mentioned in Section 1.3 shared the same methods and principles of operation, which are portrayed in Chapter 5. The measurement procedure, the definition of damage, the technique used to to detect it, as well as the expression used for calculating the peak fluence are all given therein.

The experiment of investigating the LIDT of dispersive mirrors with femtosecond pulses is described in Chapter 6. The samples under investigation are given in Section 6.1. Section 6.2 provides the specific details regarding the used laser system and set-up. The results are displayed in Section 6.3.

Chapter 7 presents a direct comparison of LIDT measured at MHz and kHz rates. Section 7.1 contains a description of investigated samples. The measurement setup and the laser sources are described in Section 7.2. Results from measurements carried out at MHz rate are compared in Section 7.3 with measurement results obtained at kHz rate. The Chapter goes on with a discussion of the outcome from the kHz and MHz experiments.

This work has made substantial use of scientific open source software based on the Python programming language. In particular, the acquired LIDT data has been evaluated using the libraries SciPy [77, 78] and SymPy [79]; most graphs in this thesis have been plotted using Matplotlib [80]. Some additional calculations have been carried out using the interactive environments IPython [81] and Sage [82].

# Chapter 2

# Ultrashort pulse propagation in transparent media

This chapter is a short theoretical introduction to the most relevant aspects of the propagation of ultrashort pulses in transparent media. We start by deriving the wave equation in isotropic, nonmagnetic media and give one of its fundamental solutions—the gaussian pulse. Then we define dispersion of first and of second order. The chapter goes on with a brief introduction to the theory of light propagation inside layered media and presents the characteristic matrix of a multilayer thin-film composition. Finally, we sketch the basic mathematical description of ultrafast optical breakdown as understood today.

## 2.1 Linear propagation and dispersion

The classical propagation of electromagnetic waves and particularly of light, is described by the Maxwell equations [83]:

$$\begin{aligned} \nabla \cdot \mathbf{D} &= \rho, && (2.1)\\ \nabla \times \mathbf{H} - \frac{\partial \mathbf{D}}{\partial t} &= \mathbf{J}, && (2.2)\\ \nabla \times \mathbf{E} + \frac{\partial \mathbf{B}}{\partial t} &= 0, && (2.3)\\ \nabla \cdot \mathbf{B} &= 0. && (2.4) \end{aligned}$$

The Eqs. (2.1)–(2.4) are complemented by the material equations:

$$\begin{aligned} \mathbf{D} &= \varepsilon_0 \mathbf{E} + \mathbf{P}, && (2.5)\\ \mathbf{H} &= \frac{1}{\mu_0}\mathbf{B} - \mathbf{M}, && (2.6)\\ \mathbf{J} &= \sigma \mathbf{E}. && (2.7) \end{aligned}$$

In Eqs. (2.1)–(2.7), **E** and **H** are the electric and the magnetic field, respectively; **D** is called electric displacement; **B** is the magnetic induction; **P** and **M** are the electric and the magnetic polarization, respectively; $\sigma$ and $\rho$ are the surface and the free charge density, respectively; and **J** is the free current density. The quantities $\varepsilon_0$ and $\mu_0$ are called respectively vacuum permittivity and vacuum permeability and are related to the speed of light in vacuum $c$ via:

$$c^2 = \frac{1}{\varepsilon_0 \mu_0}. \tag{2.8}$$

We are interested in the solution of the Maxwell equations in nonmagnetic regions space with no free charges and no free currents, so that:

$$\begin{aligned} \rho &= 0, && (2.9) \\ \sigma &= 0, && (2.10) \\ \mathbf{M} &= 0. && (2.11) \end{aligned}$$

It is practical to split the polarization **P** into linear and nonlinear parts:

$$\mathbf{P} = \mathbf{P}^{\mathrm{L}} + \mathbf{P}^{\mathrm{NL}}. \tag{2.12}$$

Then the wave equation is given by [84]:

$$\nabla^2 \mathbf{E} - \frac{n^2}{c^2}\frac{\partial^2 \mathbf{E}}{\partial t^2} = \mu_0 \frac{\partial^2 \mathbf{P}^{\mathrm{NL}}}{\partial t^2}, \tag{2.13}$$

where $n = n(\omega)$ is the frequency dependent refractive index of the material. Here, $\omega$ is the angular frequency.

One of the basic solutions of the wave equation is the gaussian pulse, given along the axis of propagation $z$ by [6, 85]:

$$E(z,t) = A(z,t)e^{i(kz-\omega t)} = A(z,t)e^{i\Phi(t)}, \tag{2.14}$$

where $A(z,t) = |E(z,t)|$ is the amplitude of electric field, and $k$ is the wavenumber. $\Phi(t) \equiv kz - \omega t$ is the temporal phase of the pulse and leads to the definition of instantaneous frequency:

$$\omega_i(t) \equiv \frac{d\Phi(t)}{dt}. \tag{2.15}$$

In dispersive media, the wavenumber depends on $\omega$:

$$k(\omega) = \frac{\omega n(\omega)}{c}. \tag{2.16}$$

Expanding Eq. (2.16) in Taylor series about the central frequency $\omega_0$, we get:

$$k(\omega) = \sum_{m=0}^{\infty} \frac{1}{m!}\frac{d^m k(\omega_0)}{d\omega^m}(\omega - \omega_0)^m. \tag{2.17}$$

The first two derivatives of $k(\omega_0)$ are frequently used separately, thus it is convenient to name them. The first derivative of $k$ over $\omega$ is the inverse group velocity (GV):

$$\frac{1}{v_g(\omega_0)} \equiv \left.\frac{dk}{d\omega}\right|_{\omega_0}. \tag{2.18}$$

The second derivative of $k$ gives information about the dispersion of the medium and is often referred to as group velocity dispersion (GVD):

$$\mathrm{GVD}(\omega_0) \equiv \left.\frac{d^2k}{d\omega^2}\right|_{\omega_0} = \frac{d}{d\omega}\frac{1}{v_g}. \tag{2.19}$$

The spectrum of a gaussian pulse is given by its Fourier transformation:

$$E(\omega) = |E(\omega)|e^{-i\varphi(\omega)}, \tag{2.20}$$

where $|E(\omega)|$ is the spectral amplitude and $\varphi(\omega)$ is the spectral phase. It is useful to expand the spectral phase into Taylor series about the central frequency $\omega_0$:

$$\varphi(\omega) = \sum_{m=0}^{\infty} \frac{1}{m!}\frac{d^m\varphi(\omega_0)}{d\omega^m}(\omega - \omega_0)^m. \tag{2.21}$$

The first derivative of the spectral phase $\varphi(\omega)$ is often used on its own and is called group delay (GD):

$$\mathrm{GD}(\omega_0) \equiv \left.\frac{d\varphi}{d\omega}\right|_{\omega_0}. \tag{2.22}$$

The second derivative of $\varphi(\omega)$ is also known as group delay dispersion (GDD):

$$\mathrm{GDD}(\omega_0) \equiv \left.\frac{d^2\varphi}{d\omega^2}\right|_{\omega_0}. \tag{2.23}$$

GDD is describes the amount of dispersion introduced to a pulse while traveling through a certain length of a dispersive medium. It can also be used to denote the amount of dispersion gained during propagation in a dispersion controlling devise, such as a stretcher or a compressor. Thus, GDD is an important characteristic of any dispersive mirror.

## 2.2 Propagation in multilayer thin-films

There are different methods to describe light propagation inside layered media such as multilayer thin-films [86]. One of the most common approaches is the method of the characteristic matrix, it owes its popularity to its computational simplicity and accurate results.

### 2.2.1 Characteristic matrix

The propagation of an electromagnetic wave in a single thin layer is described by [86, 87]:

$$\begin{pmatrix} u \\ v \end{pmatrix}_{z=z_j} = M_j \begin{pmatrix} u \\ v \end{pmatrix}_{z=z_{j-1}}, \tag{2.24}$$

where $u(z)$ and $v(z)$ are the amplitudes of the electric and the magnetic fields, respectively. The positions of the two layer boundaries on the optical axis are given by $z_{j-1}$ and $z_j$. The factor $M_j$ is called a *characteristic matrix* of $j$-th layer and has the form:

$$M_j = \begin{pmatrix} \cos\varphi_j & i\sin\varphi_j/q_j \\ iq_j\sin\varphi_j & \cos\varphi_j \end{pmatrix} \tag{2.25}$$

where the phase shift gained by the wave after passing at angle $\gamma_j$ through layer $j$ of thickness $d_j$ and complex refractive index $\tilde{n}_j$ is given by:

$$\varphi_j = k\tilde{n}_j d_j \cos\gamma_j. \tag{2.26}$$

The quantity $q_j$ is the optical admittance of $j$-th layer at oblique angle of incidence, and is given by:

$$q_j = \begin{cases} Y_0\tilde{n}_j\cos\gamma_j, & \text{for s-polarization;} \\ Y_0\tilde{n}_j/\cos\gamma_j, & \text{for p-polarization.} \end{cases} \tag{2.27}$$

Here, $\gamma_j$ is the angle of incidence on interface $j+1$. The quantity $Y_0$ is reciprocal of the impedance of free space $Z_0$ and is called *admittance of free space*:

$$Y_0 = \frac{1}{Z_0} = \frac{H}{E} = \sqrt{\frac{\varepsilon_0}{\mu_0}} = \varepsilon_0 c. \tag{2.28}$$

The characteristic matrix of the whole thin-film assembly is equal to the product of the characteristic matrices of the constituent layers:

$$\begin{pmatrix} u \\ v \end{pmatrix}_{z=z_a} = M_m M_{m-1}\dots M_1 \begin{pmatrix} u \\ v \end{pmatrix}_{z=z_0}, \tag{2.29}$$

where $z_a$ is the position of the incident medium interface and $z_0$ is the substrate interface. The characteristic matrix of the whole layer structure is:

$$M = M_m M_{m-1}\dots M_1. \tag{2.30}$$

The characteristic matrix of a composition of thin-films contains information for all properties of the assembly, such as transmittance, reflectance, phase, etc. This topic is covered rigorously and thoroughly in Refs. [86, 87]. Here, we will consider only the distribution of electric field inside a multilayer thin-film assembly.

### 2.2.2 Electric field distribution

For a monochromatic wave, the electric field at an arbitrary position $z$ along the optical axis is given by the following recurrent system of equations [87]:

$$u(z) = u(z_{j-1}) \cos[k\tilde{n}_j \cos\gamma_j\, (z - z_{j-1})] + \frac{i}{q_j} v(z_{j-1}) \sin[k\tilde{n}_j \cos\gamma_j\, (z - z_{j-1})], \tag{2.31}$$

$$v(z) = iq_z u(z_{j-1}) \sin[k\tilde{n}_j \cos\gamma_j (z - z_{j-1})] + v(z_{j-1}) \cos[k\tilde{n}_j \cos\gamma_j (z - z_{j-1})] \tag{2.32}$$

In reality, however, the refractive index depends on frequency, i.e. $\tilde{n} = \tilde{n}(\omega)$. Hence, $q_j = q_j(\omega)$ and consequently $u = u(z, \omega)$ and also $v = v(z, \omega)$.

Ultrashort pulses have broad spectral bandwidth, and the single frequency approximation discussed above is violated. Therefore, to describe the propagation of ultrashort pulses inside a multilayer thin-film structure, we need to consider the electric field distribution in time-domain. It can be obtained by applying the Fourier transformation to $u$ and $v$:

$$u(z, t) = \frac{1}{\sqrt{2\pi}} \int\limits_{-\infty}^{\infty} u(z, \omega) e^{i\omega t} d\omega, \tag{2.33}$$

$$v(z, t) = \frac{1}{\sqrt{2\pi}} \int\limits_{-\infty}^{\infty} v(z, \omega) e^{i\omega t} d\omega. \tag{2.34}$$

Eqs. (2.33) and (2.34) can be used to calculate the time-dependent electric field distribution inside a multilayer stack.

## 2.3 Optical breakdown

The optical breakdown of dielectrics in the ultrashort regime begins by promoting valence electrons to the conduction band. When the density of free carriers reaches some critical value $f_{cr}$, the plasma frequency becomes comparable to the frequency of the incident laser field and starts to absorb strongly, leading to ablation. In SI units, the plasma frequency is given as:

$$\omega_{pe} = \sqrt{\frac{fe^2}{m^* \varepsilon_0}}, \tag{2.35}$$

where $f$ is the concentration of electrons, $e$ is the elementary charge, $m^*$ is the effective electron mass, and $\varepsilon_0$ – the electric constant.

When the critical electron density $f_{cr}$ is reached, the plasma frequency becomes comparable to the frequency of the laser field, i.e., $\omega_{pe} \approx \omega$:

$$f_{cr} \approx \frac{\omega^2 m^* \varepsilon_0}{e^2}. \tag{2.36}$$

Here $\omega$ is the frequency of the laser field. At near ifrared (NIR) frequencies, the critical electron density is in the order of $f_{cr} \approx 10^{21}\,\mathrm{cm}^{-3}$.

Mainly two mechanisms contribute to the promotion of free carriers to the conduction band: photoionization and impact ionization. The first occurs when a valence electron is excited under the influence of the external field whether via multiphoton ionization (MPI) or via tunneling ionization. The impact ionization takes place when an energetic electron in the conduction band interacts with a valence band electron giving it enough energy to reach the conduction band, resulting in two conduction band electrons. This is also known as *avalanche ionization*. These mechanisms are discussed below.

### 2.3.1 Photoionization

The photoionization rate in solids is given by the Keldysh theory [88]:

$$w = \frac{2\omega}{9\pi}\left(\frac{m^*\omega}{\gamma\beta\hbar}\right)^{\frac{3}{2}} Q\left(\gamma,\, \frac{\tilde{U_I}}{\hbar\omega}\right) \exp\left\{-\pi\left\lfloor\frac{\tilde{U_I}}{\hbar\omega}+1\right\rfloor\frac{\mathcal{K}(\gamma\beta)-\mathcal{E}(\gamma\beta)}{\mathcal{E}(\beta)}\right\}, \tag{2.37}$$

where

$$\gamma = \frac{\omega\sqrt{m^*U_I}}{eE} \tag{2.38}$$

is the Keldysh parameter, $\tilde{U_I}$ is the effective ionization potential:

$$\tilde{U_I} = \frac{2\mathcal{E}(\beta)}{\pi\gamma\beta}U_I, \tag{2.39}$$

and

$$\beta \equiv \frac{1}{\sqrt{1+\gamma^2}}. \tag{2.40}$$

Also, we have made use of the floor function:

$$\lfloor x\rfloor = \max\left\{l \in \mathbb{Z} \mid l \leq x\right\}. \tag{2.41}$$

The function $Q(\gamma, \tilde{U_I}/\hbar\omega)$ is of the form:

$$Q(\gamma, x) = \sqrt{\frac{\pi}{2\mathcal{K}(\beta)}}\sum_{n=0}^{\infty}\exp\left\{-n\pi\frac{\mathcal{K}(\gamma\beta)-\mathcal{E}(\gamma\beta)}{\mathcal{E}(\beta)}\right\}\Phi\left\{\pi\sqrt{\frac{2\lfloor x+1\rfloor-2x+n}{2\mathcal{K}(\beta)\mathcal{E}(\beta)}}\right\}, \tag{2.42}$$

where $\Phi(z)$ is the Dawson's integral:

$$\Phi(z) = \int_0^z e^{y^2-z^2}dy. \tag{2.43}$$

In Eqs. (2.37) and (2.42), $\mathcal{K}$ and $\mathcal{E}$ are the complete elliptic integrals of the first and the second kind, respectively:

$$\mathcal{K}(x) = \int\limits_0^{\pi/2} \frac{d\theta}{\sqrt{1 - x^2 \sin^2\theta}}, \qquad \mathcal{E}(x) = \int\limits_0^{\pi/2} \sqrt{1 - x^2 \sin^2\theta}\, d\theta. \tag{2.44}$$

In the case of strong fields and low frequencies when $\gamma \ll 1$, Eq. (2.37) reduces to the formula for tunneling ionization:

$$w = \frac{2}{9\pi^2}\frac{U_I}{\hbar}\left(\frac{m^* U_I}{\hbar^2}\right)^{3/2}\left(\frac{e\hbar E}{\sqrt{m^* U_I^3}}\right)^{5/2} \exp\left\{-\frac{\pi}{2}\frac{\sqrt{m^* U_I^3}}{e\hbar E}\left(1 - \frac{1}{32}\frac{U_I}{U_p}\right)\right\}. \tag{2.45}$$

In the opposite case of high frequencies when $\gamma \gg 1$, we obtain the formula for MPI:

$$w = \frac{2\omega}{9\pi}\left(\frac{m^*\omega}{\hbar}\right)^{3/2} \Phi\left(\sqrt{2l - \frac{2\tilde{U}_I}{\hbar\omega}}\right) \exp\left\{2l\left(1 - \frac{U_p}{U_I}\right)\right\}\left(\frac{U_p}{4U_I}\right)^{l} \tag{2.46}$$

where the effective ionization potential $\tilde{U}_I$ is:

$$\tilde{U}_I = U_I + U_p, \tag{2.47}$$

and $U_p$ is the ponderomotive energy given by:

$$U_p = \frac{e^2 E^2}{4 m^* \omega^2}. \tag{2.48}$$

In Eq. (2.46) $l$ denotes the number of photons needed to overcome the effective ionization potential $\tilde{U}_I$:

$$l = \left\lfloor \frac{\tilde{U}_I}{\hbar\omega} + 1 \right\rfloor. \tag{2.49}$$

### 2.3.2 Impact ionization

Another source for conduction band electrons is the impact ionization, when an energetic electron interacts with a valence band electron and transfers enough of its energy to the valence band electron to promote it to the conduction band. The result of this interaction is two electrons at the bottom of the conduction band.

When the electron density in the conduction band is sufficiently high, an avalanche process can take place, making a significant contribution to the plasma density. The avalanche excitation rate is given by a Drude model [62, 69]

$$w_{av} = \frac{\sigma}{U_I} f I, \tag{2.50}$$

where the cross section

$$\sigma = \frac{k_0 \omega \tau_c}{n_0^2 f_c (1 + \omega^2 \tau_c^2)} \tag{2.51}$$

and the collision time $\tau_c$ is given by

$$\tau_c = \frac{16 \pi \epsilon_0 \sqrt{m E_{kin}^3}}{\sqrt{2} e^4 f}. \tag{2.52}$$

# Chapter 3

# Dispersion control and measurement

The domain of ultrafast optics deals with pulse durations of the order of femtoseconds or less. Given a certain spectrum, the shortest possible pulse is characterized by a flat spectral phase, i.e. when all spectral components are in phase. When a pulse propagates through a medium with normal dispersion, the low-frequency spectral components travel faster than high-frequency spectral components. This process is known as "chirping," and it leads to temporal broadening of the pulse . To counteract this process, dispersion with the same magnitude but an opposite sign must be introduced to the pulse to keep it as short as possible.

Dispersion can be controlled using different techniques. Most are either based on prisms [30], on gratings [29], on dispersive mirrors [31–34] or on a combination thereof [28, 35]. There are advantages and disadvantages to each of these methods. For example, large amount of dispersion can be obtained using prisms or gratings, but they are difficult to align and generally have relatively low efficiency. Moreover, they might introduce spatial chirp, as well as dispersion of higher order, both of which are often undesirable. On the other hand, dispersive mirrors can control second- as well as higher orders dispersion of broadband pulses with high degree of accuracy [38, 39]. When dispersion control is necessary only for a narrow spectral band, dispersive mirrors can be produced with reflectivity higher than 99.9 % [37, 40]. In addition, dispersive mirrors are simpler to install in optical systems with respect to prisms and gratings [37]. However, dispersive mirrors can only introduce moderate, bandwidth-dependent amount of dispersion per reflection [36]. Nevertheless, thanks to their ability to fine-tune dispersion, as well as their user-friendliness, dispersive mirrors are widely used to control dispersion of ultrashort pulses [89].

In this Chapter, we first illustrate qualitatively how dispersion is obtained within dispersive mirrors. Next, we describe a novel technique for quantitative measurements of the dispersion characteristics of mirrors and compare it with the conventional method. Finally, we discuss some issues related to the ultrashort pulse damage of dispersive mirrors.

## 3.1 Resonant storage and wavelength-dependent penetration

Dispersion control by means of specially crafted multilayer mirrors has been reported for the first time almost three decades ago [31]. These first dispersive mirrors had inside their layer stack a spacer layer of half-wave optical thickness which resembles a Gires-Tournois interferometer (GTI) [90]. Inside a GTI, certain resonant frequencies gain nonlinear phase shift, which translates into GD with respect to non-resonance frequencies (Fig. 3.1(b)). This phenomenon is also known as *resonant storage* and allows large amounts of GDD to be introduced. However, due to their nature, the GTI mirrors operate only within a relatively narrow spectral bandwidth.

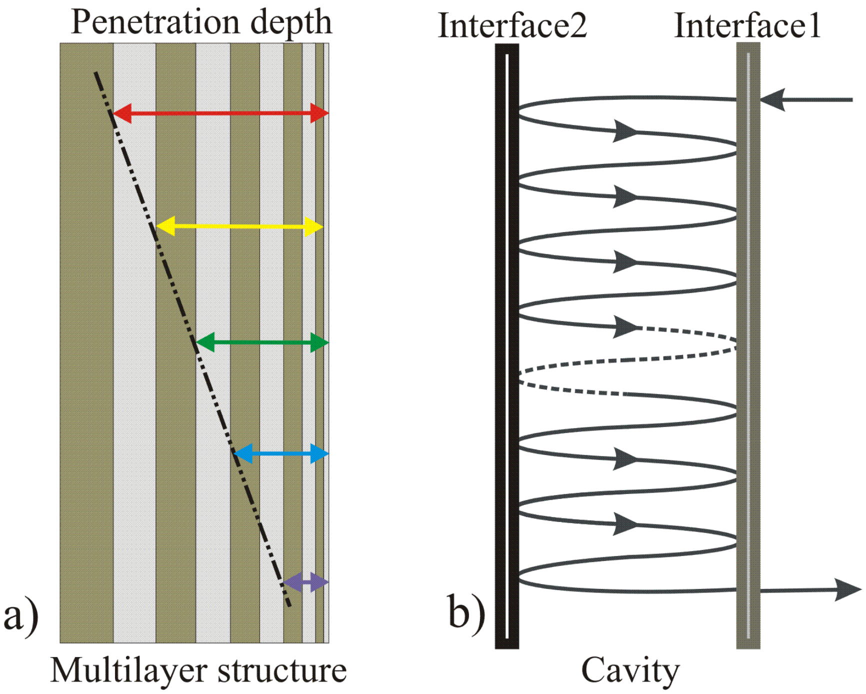

**Figure 3.1:** Dispersion via wavelength-dependent penetration (a) and resonant storage (b). (a) The optical thickness of layers varies gradually in a chirped multilayer structure. This causes different spectral components to penetrate to different depths within the stack and hence to attain different GDs. (b) Two interfaces separated by a half-wavelength optical thickness distance resonantly enclose the incident resonant wave. Such nanoscale GTIs embedded in the multilayer structure can introduce large GDs at selected wavelengths. A combination of both effects allows to overcome the limitations imposed by the two effects when used separately. (Reprinted from [91])

Another approach to dispersion control is provided by the so-called "chirped mirrors" [32]. They were given this name due to the fact that the optical thicknesses of layers change gradually with the layer number, which causes spectral components of different frequencies to penetrate to different depths within the layer stack (Fig. 3.1(a)). Due to this *wavelength-dependent penetration*, different frequencies experience different GDs. Chirped mirrors successfully overcome the bandwidth limitation of GTI mirrors, but fail to introduce large amount of GDD per reflection. The obtainable GDD is limited by the maximum attainable GD difference between the extremes of the reflectivity range [92]. In turn, this is connected to the optical thickness of the coating.

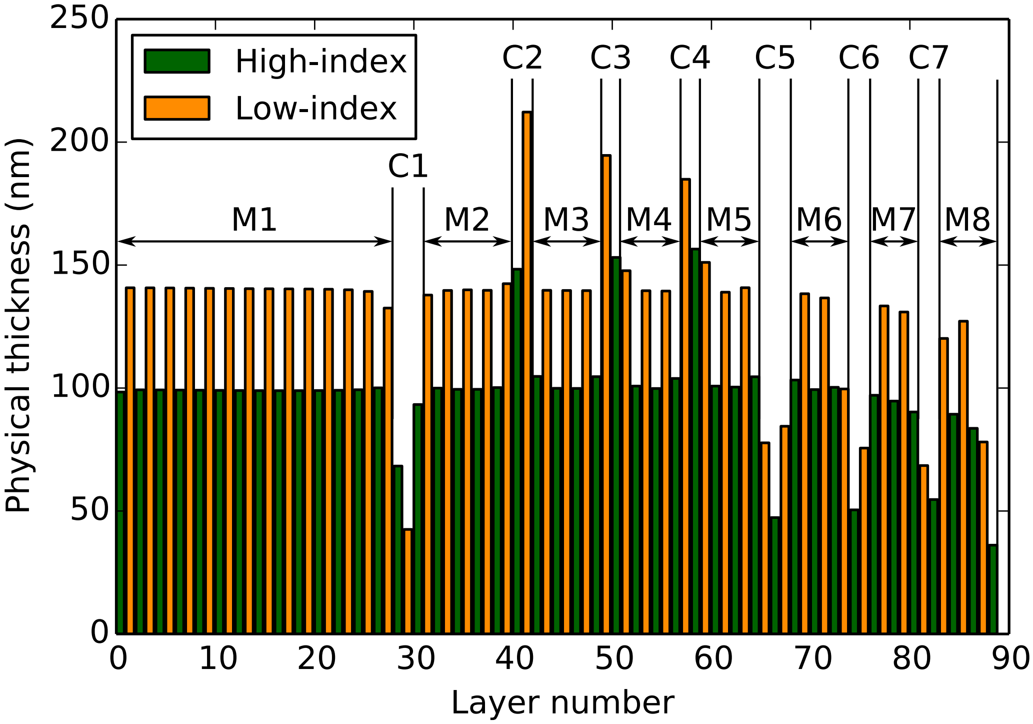

**Figure 3.2:** Physical thicknesses of alternating layers of $Ta_2O_5$ and $SiO_2$ are shown with green and orange columns, respectively. The structure can be viewed as a combination of eight mirrors (M1-M8) and seven resonant cavities (C1-C7). Consequently, the GDD comes from penetration and resonance effects. (Adapted from [91])

In the quest for making broadband high-dispersive mirrors, efforts have been made to improve GTI mirrors [33, 34]. However, it has been the successful combination of the advantages of both chirped mirrors and GTI structures into a single mirror [37, 91] that has overcome the limitations of the conventional approaches. Figure 3.2 shows a physical thickness profile of a high-dispersive mirror, which makes use of both the wavelength-dependent penetration and the resonant storage effects. This becomes apparent when we take a look at the electric field distribution inside of the dielectric stack of the mirror (Fig. 3.3): the high-frequency components are reflected near the top of the stack, whereas the low-frequency components penetrate deeper in the layer stack (wavelength-dependent penetration); the localized enhancements of the electric field indicate that resonance frequencies are "stored" inside certain layers (resonant storage).

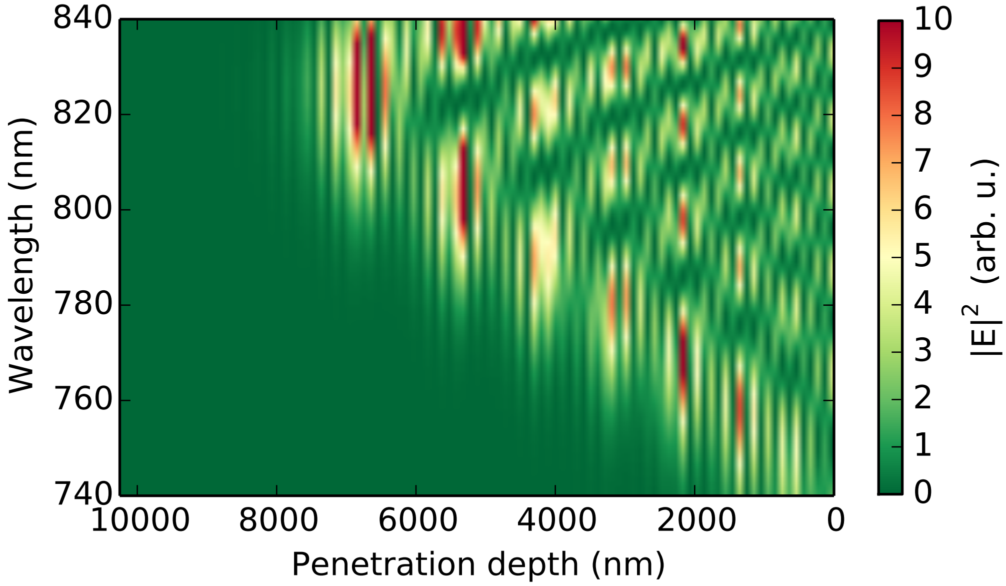

**Figure 3.3:** Typical electric field distribution inside of the layer stack of a dispersive mirror. The light enters the multilayer structure from the left; the interface with the incident medium is at the zero of the $x$-axis. The shorter wavelength components are reflected in the layers near the incident medium. The longer wavelength components penetrate deeper in the mirror and thus gain delay with respect to the shorter ones. Some frequencies undergo "trapping" within certain regions of the layer stack, resulting in additional delay. The enhanced electric field in these regions (yellow to red) is an indication for resonant storage effect. The plotted electric field is normalized with respect to the incident electric field. (Adapted from [91])

## 3.2 Resonance scanning interferometer for dispersion measurements

The most important characteristics of dispersive mirrors are, naturally, the GD and the GDD that they introduce in an impinging laser pulse. For pulses shorter than 50 fs, dispersion of higher orders plays also an important role. Therefore, it is essential to be able to accurately measure these properties in order to check and verify the quality of produced dispersive mirrors. Moreover, precise GD and GDD measurements can give valuable feedback to the production process [93].

## White-light interferometer

Presently, the most widely used techniques for GD and GDD measurements involve white-light interferometer (WLI) [94–97], which are typically based on the Michelson interferometer (Fig. 3.4). The measurement sample is placed in one of the arms of the interferometer, whereas the other arm, the reference arm is scanned, recording the resulting interference patterns (interferograms) at each step. The gathered data is then processed to obtain the GD and GDD of the sample.

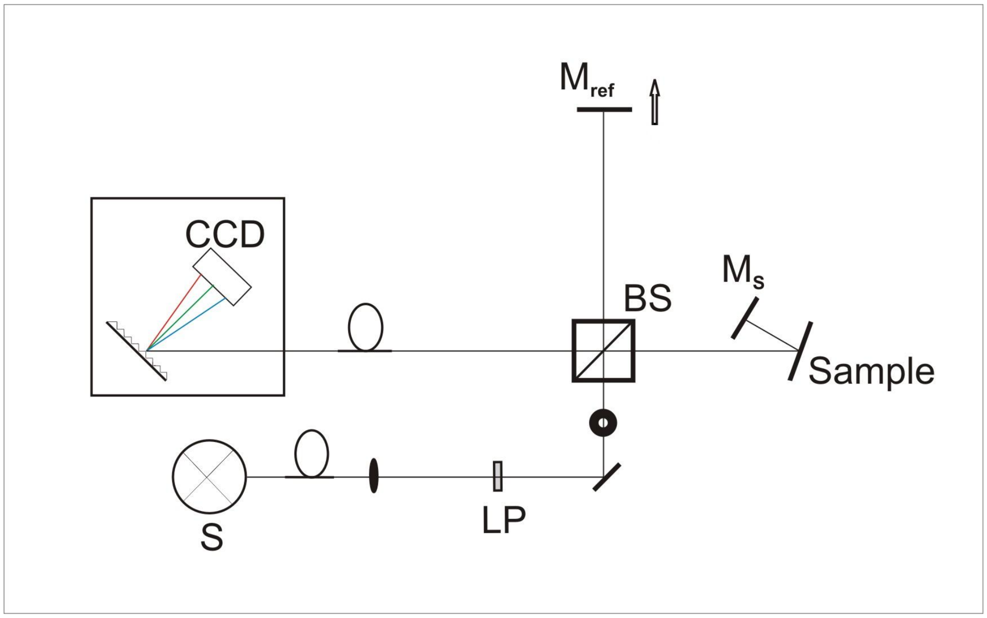

**Figure 3.4:** Michelson-type white-light interferometer for dispersion measurements: S – light source; LP – long-pass filter; BS – beam splitter; $M_s$ – end mirror in the sample arm; $M_{ref}$ – end mirror in the reference arm; CCD – digital sensor inside of a spectrometer (reprinted from [98]).

The noise arising within the light source and the detector, the precision of the step motor scanning the reference arm, as well as micrometer-scale vibrations of the set-up all affect the recorded interferograms [99]. This makes the evaluation of GD and GDD a difficult problem, which has been subject of several studies [94–97, 99, 100]. In addition, the wavelength and GDD resolution of the WLI approach is rather poor, especially for applications with high demands on the dispersion properties of the mirrors. Some of these applications require mirrors with large amount of GDD, e.g. high-energy mode-locked oscillators [37, 40, 46]; others like enhancement cavities need mirrors with as little as possible dispersion [50, 51]; and yet others such as the generation of near-single-cycle optical pulses rely upon ultra-broadband dispersive mirrors [15, 38].

### Resonance scanning interferometer

An alternative approach for GD and GDD measurements based on determination of the resonance frequencies of a Fabry-Pérot interferometer was suggested by Osvay *et al.* [101]. The mirrors forming the interferometer were the mirrors to be measured. Their GD was determined using a formula relating the difference between adjacent resonant frequencies to the average GD within that frequency interval. The shortcomings of this simple approach are that for small spacer thickness the distances between resonance frequencies are large, resulting in small spectral resolution. On the other hand, if the spacer thickness is increased, the resonant peaks decrease and soon become indistinguishable from noise. A trade-off spacer thickness was often difficult to find and even then it was unable to provide simultaneously good resolution and signal-to-noise ratio. Another problem of this approach was the requirement of accurate determination of the spacer thickness, which was difficult to measure due to its micrometer scale.

To address the limitations of Michelson-type WLI, and recognizing the potential of the method described in [101], we have developed another technique for dispersion measurements [102, 103], which builds upon the one in Ref. [101]. Our method is based on series of measurements of the resonant frequencies for different spacer thicknesses and simultaneous processing of all measurement data. To reflect the fact that the interferometer is being scanned, we called our technique *Resonance Scanning Interferometer (RSI)*. One of its advantages is that it does not require setting the spacer thickness precisely nor its determination. The only requirement is the parallel alignment of the interferometer and its stability during the measurement process. With this improvement, RSI has been able to surpass WLI in terms of both simplicity and compactness, while at the same time providing greater accuracy of the GD/GDD measurements.

### 3.2.1 Experimental set-up

The measurement set-up consists of a light source, a spectrometer, and a pair of parallel mirrors, one of which is mounted on a translation stage (Fig. 3.5). Measurements can be performed either in transmission mode (Fig. 3.5(a)) resembling a Fabry-Pérot interferometer or in reflection (Fig. 3.5(b)) resembling a GTI. In both cases, the GD and GDD could be determined at an arbitrary combination of angle of incidence and polarization.

We used a grating spectrometer with a different detector or a different light source depending on the measurement spectral range. A 250 W tungsten lamp was used as light source for wavelengths above 450 nm, whereas a 75 W xenon lamp was used for shorter wavelengths. For measurements below 1050 nm the detector was a CCD camera (grid step: 0.37 nm), and for measurements deeper in the IR we used an InGaAs photodiode array (grid step: 0.61 nm).

The sample was mounted on a motorized linear translation stage, which allowed us to vary the spacer thickness, thus scanning the interferometer without changing the alignment

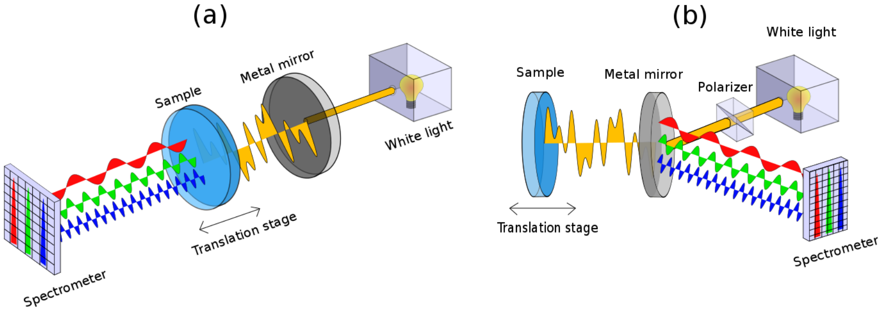

**Figure 3.5:** Schematic representation of the resonant scanning interferometer (a) in transmission- and (b) in reflection mode (reprinted from [102]).

otherwise. However, the term "measurement scan" is used below in the sense of a scan in frequency domain, i.e. it denotes the procedure of determination of the resonance frequencies for a certain spacer thickness.

### 3.2.2 Theory

Let us consider two parallel mirrors with air spacer between them, as shown in Fig. 3.5. One of the mirrors has known properties: we have used an aluminum mirror with virtually zero GD [94] and reflectance of about 90 %, whereas the second mirror is the sample with unknown GD.

The total transmittance of the system is [86, 104].

$$T = \frac{T_m T_s}{\left(1 - \sqrt{R_m^- R_s^+}\right)^2 + 4 R_m^- R_s^+ \, \sin^2\left(\frac{\phi_m + \phi_s + \delta}{2}\right)} \tag{3.1}$$

where $T_m$ and $T_s$ are respectively the transmittances of the metal mirror and the sample mirror; $R_m^-$ is the reflectance of the metal mirror in opposite direction of the incident beam, and $R_s^+$ is the reflectance of sample in direction of the beam; $\phi_m$ and $\phi_s$ are the phase-shifts gained at reflection upon the metal mirror and the sample, respectively; and $\delta$ is given by:

$$\delta = \frac{2\omega d_s n_s \cos\theta_s}{c}, \tag{3.2}$$

where $c$ is the speed of light in vacuum. Physically, $\delta$ represents the phase-shift gained by an electromagnetic wave of angular frequency $\omega$ per round-trip through a spacer of thickness $d_s$ and refractive index $n_s$ at angle $\theta_s$.

The resonance frequencies must satisfy the resonance condition:

$$\frac{\phi_m + \phi_s + \delta}{2} = k\pi, \qquad k = 1,\, 2,\, \ldots \tag{3.3}$$

Here $k$ is integer and denotes the resonance order. Let us now consider two adjacent resonance frequencies $\omega_j$ and $\omega_{j+1}$ with phases $\varphi_j$ and $\varphi_{j+1}$, respectively. The phase difference between them will then be given by:

$$\Delta\varphi_j \equiv \varphi_{j+1} - \varphi_j = \frac{2d_s n_s \cos\theta_s}{c}(\omega_{j+1} - \omega_j) - 2\pi. \tag{3.4}$$

Using (2.22) we get:

$$\overline{GD}_j = \frac{2d_s n_s \cos\theta_s}{c} - \frac{2\pi}{\Delta\omega_j}, \tag{3.5}$$

where

$$\Delta\omega_j = \omega_{j+1} - \omega_j;$$

and

$$\overline{GD}_j = \frac{1}{\Delta\omega_j}\int\limits_{\omega_j}^{\omega_{j+1}} GD(\omega)\, d\omega$$

is the average GD in the interval $\omega \in [\omega_j,\, \omega_{j+1}]$.

Since there are no trivial ways to measure the spacer thickness $d_s$ in Eq. (3.5) with the necessary nanometer precision, it would be worthwhile to exclude it from the calculations. This can be done by taking into consideration the difference between the values of the average GD within two adjacent frequency intervals, namely within $[\omega_j,\, \omega_{j+1}]$ and $[\omega_{j+1},\, \omega_{j+2}]$:

$$\overline{GD}_{j+1} - \overline{GD}_j = 2\pi\left(\frac{1}{\Delta\omega_j} - \frac{1}{\Delta\omega_{j+1}}\right). \tag{3.6}$$

This recursive formula gives consecutively the average GD for each interval. Since adding a constant GD term is irrelevant, we can safely choose as initial condition $\overline{GD}_1 = 0$. By expanding the recursion (3.6) it can be shown that:

$$\overline{GD}_j = 2\pi\left(\frac{1}{\Delta\omega_1} - \frac{1}{\Delta\omega_j}\right). \tag{3.7}$$

It is worth noting that Eqs. (3.7) give the averaged GD values with precision directly related to the precision of determination of the resonance frequencies. This is in contrast with the expression for GD given in [101], which is only an approximation and as such it introduces uncertainty in addition to the experimental one. Furthermore, Eqs. (3.7) do not depend on the spacer thickness $d_s$, and can be used with an arbitrary step size.

If the distances between adjacent resonance frequencies $\Delta\omega_j$ are small enough, the sequence $\overline{GD}_j$ will approach the spectral dependence of group delay $GD(\omega)$. However, while it is possible to increase the density of the resonance frequencies by increasing the spacer thickness, this comes at the expense of reducing the amplitude of resonant peaks. As the amplitude of the resonant peaks approaches the noise level, it becomes increasingly more difficult to accurately determine their position. On the other hand, when their

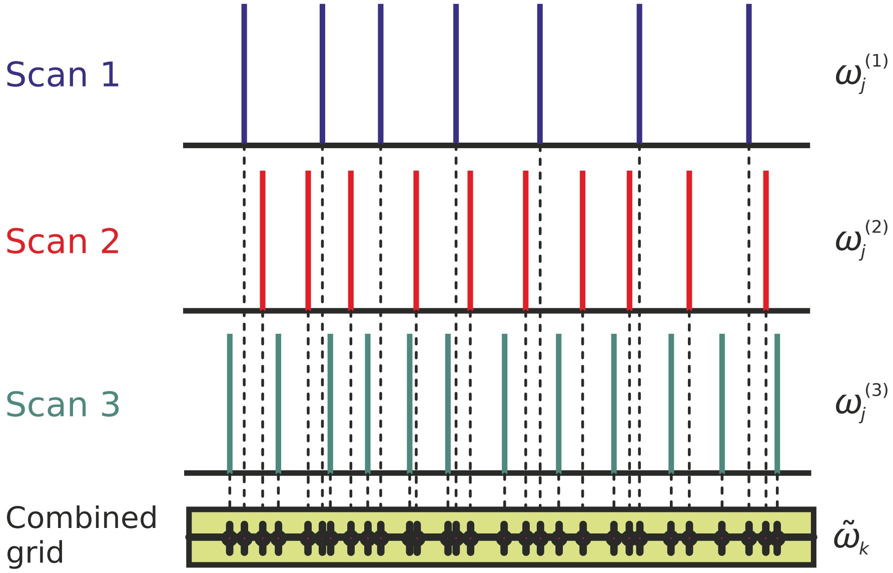

**Figure 3.6:** Merging data from measurements with different spacer thicknesses into a combined grid. (Reprinted from [102])

amplitude is sufficiently high, the resonant peaks are too sparse for obtaining $GD(\omega)$ with high resolution.

Alternatively, to increase the density of the frequency grid, we can combine measurements with different spacer thicknesses as shown in Fig. 3.6. This will allow us to achieve significantly higher spectral resolution.

Let the total number of scans be $L$, where the $i$-th scan has number of resonance peaks $N_i$, and let $M = \sum N_i$ denote the total number of maxima. Then Eq. (3.7) transforms into:

$$\overline{GD}_{i,j} = 2\pi \left( \frac{1}{\Delta\omega_{i,1}} - \frac{1}{\Delta\omega_{i,j}} \right), \tag{3.8}$$

where $i = 1, \ldots, L$ and $j = 2, \ldots, N_i - 1$. Also, let us denote with $\{\tilde{\omega}_k\}_{k=1,\ldots,M}$ the set of combined resonance frequencies from all scans. Then the average GD between two resonance frequencies $\omega_{i,j}$ and $\omega_{i,j+1}$ from the $i$-th measurement scan will be equal to:

$$\overline{GD}_{i,j} = \frac{1}{\Delta\omega_{i,j}} \sum_k \Delta\tilde{\omega}_k \, \overline{GD}_k, \tag{3.9}$$

where the summation is over the set of all indices $k$ for which $[\tilde{\omega}_k, \tilde{\omega}_{k+1}] \subset [\omega_{i,j}, \omega_{i,j+1}]$.

We can combine Eqs. (3.8) and (3.9) to obtain a system of linear algebraic equations (SLAE):

$$\frac{1}{\Delta\omega_{i,j}} \sum_k \Delta\tilde{\omega}_k \, \overline{GD}_k = 2\pi \left( \frac{1}{\Delta\omega_{i,1}} - \frac{1}{\Delta\omega_{i,j}} \right), \tag{3.10}$$

which can also be expressed in matrix form:

$$\mathbf{A}\mathbf{x} = \mathbf{b}. \tag{3.11}$$

Here the vector $\mathbf{x}$ is composed of the unknown elements $x_k = \overline{GD}_k$; $\mathbf{b}$ contains the right-hand side of (3.10); and the matrix $\mathbf{A}$ takes the form:

$$A_{i,j,k} = \frac{\Delta\tilde{\omega}_k}{\Delta\omega_{i,j}}.$$

Equation (3.11) is a system of $M-2L$ equations, since the number of intervals between the $N_i$ resonance frequencies in each measurement scan $i$ is only $N_i - 1$. An additional equation is lost due to the exclusion of the spacer thickness. On the other hand, the number of unknowns $\overline{GD}_k$ is $M-2$. Except for the case of a single scan, i.e. $L = 1$, this makes the SLAE (3.11) underdetermined. Thus, finding $\mathbf{x}$ is an inverse ill-posed problem, the solution of which can be found by application of a regularization theory [105]. The question of how to apply this theory to the problem at hand is discussed in some detail in ref. [103] and will not be considered here.

The approach described so-far has two major deficiencies: the potential non-uniformity of the combined grid and the discreetness of the obtained spectral dependence of $GD(\omega)$. The latter problem gives rise to difficulties related to the differentiation of $GD(\omega)$, which is required in order to obtain the parameter of practical interest $GDD(\omega)$. These shortcomings can be overcome by approximating the obtained $GD(\omega)$ with a cubic spline function. Let us introduce a new uniform frequency grid $\{y_i\}_{i=1,\ldots,K}$, such that its boundary points coincide with the boundary points of the non-uniform combined frequency grid, i.e.: $y_1 = \tilde{\omega}_1$, $y_K = \tilde{\omega}_M$. Now we can represent $GD(\omega)$ as a cubic spline function with coefficients $a_i$, $b_i$, $c_i$, and $d_i$ [106]:

$$GD(\omega) = a_i + b_i(\omega - y_i) + c_i(\omega - y_i)^2 + d_i(\omega - y_i)^3, \quad \omega \in [\tilde{\omega}_i, \tilde{\omega}_{i+1}). \tag{3.12}$$

If we substitute Eq. (3.12) into Eq. (3.10), we will obtain a SLAE analogous to Eq. (3.11), where $\mathbf{x}$ will contain the coefficients $a_i$, $b_i$, $c_i$, and $d_i$. Solving this SLAE, we will obtain continuous spectral dependence $GD(\omega)$, which can be differentiated analytically to obtain $GDD(\omega)$.

### 3.2.3 Experimental results

In addition to the simplicity of RSI set-up with respect to WLI, the new technique offers improved spectral and GD/GDD resolution. To demonstrate that, let us consider a few examples.

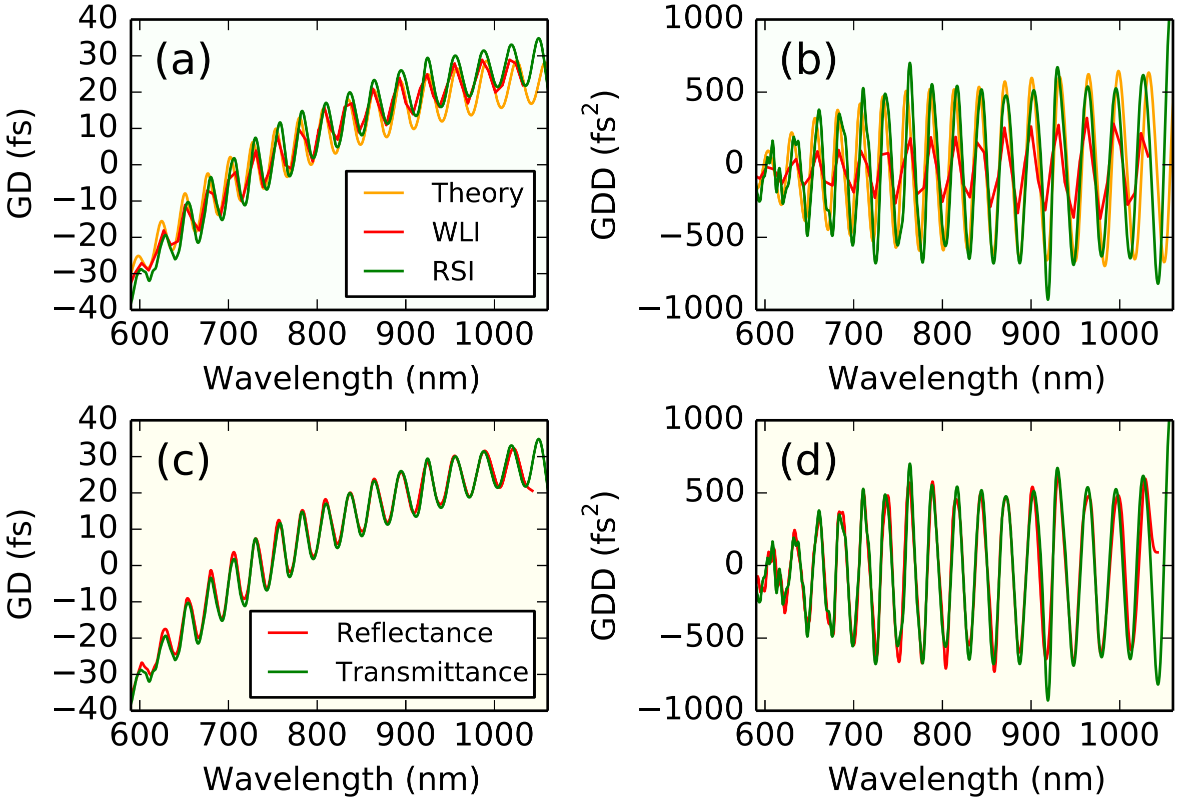

**Figure 3.7:** (a) and (b): GD and GDD measured using RSI in transmission (green curves) compared to WLI results (red curves) and theoretical data (orange curves). (c) and (d): Comparison of GD and GDD data obtained using RSI in reflection (red curves) and in transmission (green curves).

## Measurements in reflection vs transmission

The first example demonstrates the consistency of measurements performed in transmission and reflection. The sample is a broadband dispersive mirror with working range from 600 nm to 1050 nm.

The GD and GDD spectral dependencies are compared respectively in Fig. 3.7(a) and Fig. 3.7(b) with theoretical data and with measurements carried out using a WLI. Some deviations of measured GD and GDD curves from the theoretical one are to be expected due to inevitable deposition errors in layer thicknesses. However, a good correspondence between the measurements performed using WLI and RSI should be noted. Additionally, the RSI technique was able to resolve the oscillations in the GDD spectral dependence much better than WLI.

The feasibility of performing equally accurate measurements both in transmission and in reflection is demonstrated in Fig. 3.7(c) and Fig. 3.7(d). Moreover, the remarkable correspondence between these two independent measurements performed in two different regimes provides an additional verification of the RSI method.

## Broadband mirrors

Few-optical cycle pulses require mirrors that support spectrum spanning about or even more than one optical octave. Furthermore, part of this spectrum might be outside the working range of a single spectrometer. The dispersion characterization of such broadband mirrors is challenging in its own right. The following example shows that with RSI it is possible to acquire measurement data in two different but partially overlapping spectral ranges and then process the obtained data simultaneously.

In this example, the sample is a broadband dispersive mirror with working range from 650 nm to 1350 nm. Since this range is not covered by any single spectrometer available in the lab, we split the spectral band into two overlapping parts: the range from 650 nm to 1060 nm is measured using the CCD spectrometer; from 850 nm to 1350 nm is covered by the InGaAs photodiode array.

Two measurement scans for the ranges from 650 nm to 1060 nm and from 850 nm to 1350 nm are shown in Fig. 3.8(a) and Fig. 3.8(b), respectively. The difference of peak values is due to variation of the spectral responses of the used spectrometers, both of which are operated near the edge of their respective working ranges.

All experimental data gathered in both wavelength ranges was processed simultaneously resulting in the GD and GDD spectral dependencies shown in Fig. 3.8(c) and Fig. 3.8(d), respectively. The results are in good overall agreement with the theoretical expectation. The small discrepancies can be assigned to manufacturing errors.

## High-dispersive, narrow-band mirrors

The operation of Yb:YAG mode-locked femtosecond oscillators requires low-loss high-dispersive mirrors [37, 40]. The challenge in characterizing such mirrors lies in their relatively narrow wavelength ranges of 5 nm to 20 nm, which are difficult to resolve using WLI.

Here, we consider a high-dispersive mirror [40] with nominal GDD of $-3000\,\mathrm{fs}^2$ and reflectance $> 99.95\,\%$ in the range from 1015 nm to 1030 nm. Using the RSI technique, mirrors with such reflectivity can only be measured in reflection (Fig. 3.5(b)), since the signal in transmission would be indistinguishable from noise. Thus the following measurements were carried out in reflection.

The dispersion properties of the sample have been measured in the range from 940 nm to 1100 nm. Figure 3.9 compares the GD and GDD spectral dependencies obtained using RSI to the respective curves retrieved using WLI as well as to the theoretical curves. The small shift of the measured curves towards shorter wavelengths can be attributed to a slight under-deposition of the layers of the mirror during manufacturing. Besides this variation,

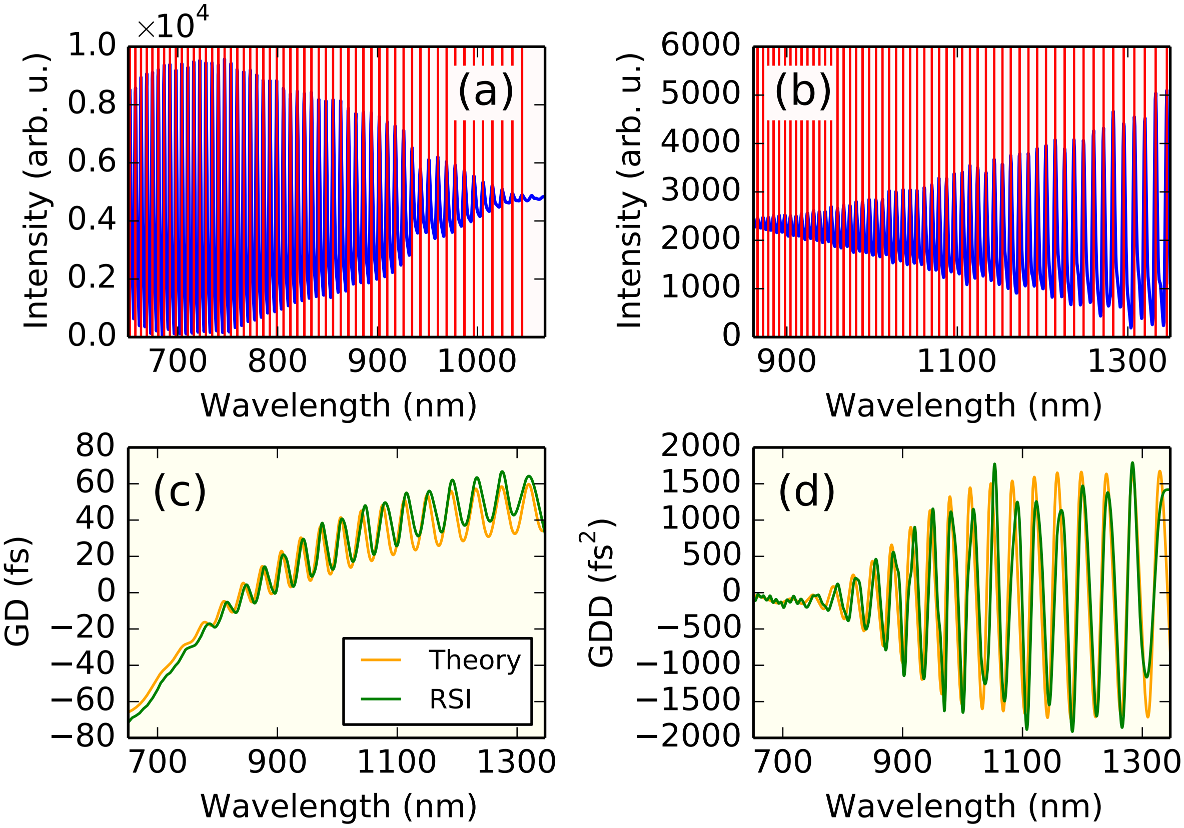

**Figure 3.8:** (a) and (b): Resonance peaks of measurement scans in reflection in ranges: (a) 650 nm to 1060 nm and (b) 850 nm to 1350 nm. (c) and (d): GD and GDD wavelength dependencies of a broadband dispersive mirror, covering a spectral range larger than one octave (650 nm to 1350 nm). The measured data (green curve) is compared to the theoretical prediction (orange curve).

the RSI measurements have properly reconstructed the resonant features around 960 nm and 1080 nm, while WLI has failed to detect them (Fig. 3.9(a) and Fig.3.9(b)).

The same data set has been processed once again, this time limiting the wavelength range to 1000 nm to 1050 nm, allowing us to obtain a more detailed picture of the GD and GDD curves around the working range of the mirror (Fig. 3.9(c) and Fig. 3.9(d)). The same shift towards shorter wavelengths is visible also in these figures. The oscillations in the measured GDD curve (Fig. 3.9(d)) should also be attributed to inevitable deposition errors in layer thicknesses. The fact that RSI measurements show these features shows that the new technique has superior spectral and GD/GDD resolution compared to WLI.

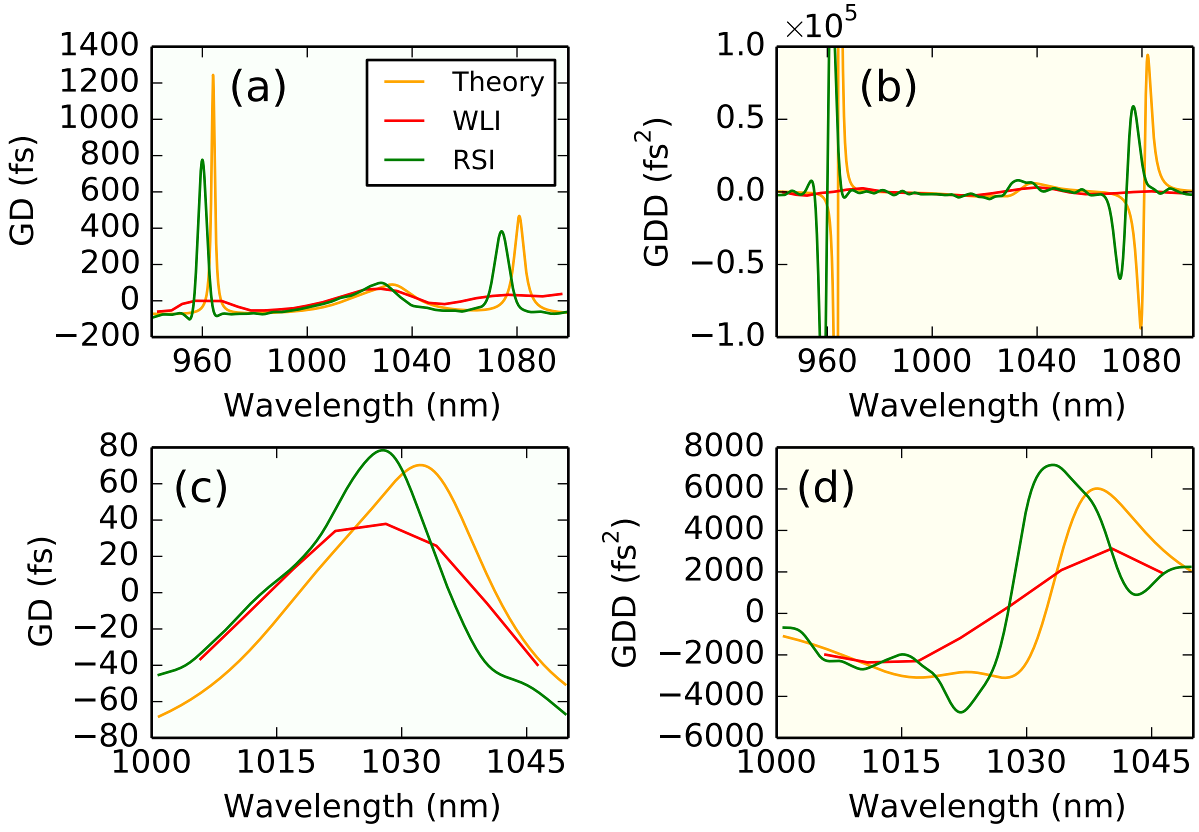

**Figure 3.9:** (a) and (b): GD and GDD results in a wide range from 940 nm to 1100 nm obtained using WLI (red curves) and RSI (green curves) are compared to theoretical data (orange curves). (c) and (d): Similarly, for the narrower range from 1000 nm to 1040 nm.

## 3.3 Conclusion

The generation of ultrashort pulses requires precise control over dispersion. Dispersive mirrors are attractive tools for managing GDD as well as third-order dispersion and facilitate the attainment of the shortest possible pulse duration. The interplay between the resonant storage effect and the wavelength-dependent penetration is the working mechanism of modern dispersive mirrors.

Before dispersive mirrors are put to use, however, their dispersion properties have to be measured. This information also provides valuable feedback to the production process. Currently, the conventional method for dispersion measurements is based on WLI, which has insufficient wavelength- and GDD resolution for some more demanding applications of dispersive mirrors.

We have developed a novel technique for dispersion measurements of multilayer mirrors, we have called it RSI. It is based on a Fabry-Pérot interferometry and draws on a concept initially proposed in Ref. [101]. However, in contrast to the stationary interferometer used in Ref. [101], in our method we have recorded transmission or reflection spectra for a number of different spacer widths and have processed all gathered data simultaneously. This has enabled us not only to exclude knowledge regarding the spacer thickness from the evaluation, but has also allowed us to reach unprecedented precision of the measured GD. We have demonstrated that RSI has been able to surpass WLI in terms of both spectral and GDD resolution. We expect that the new technique will facilitate the efforts in pushing the frontiers dispersive mirror technology.

# Chapter 4

# Mirror characterization techniques

Ultrafast laser systems, as well as experiments which rely on such lasers demand special optics. For instance, it is generally necessary that the mirrors used in an ultrafast laser to have very high reflectivity (often larger than 99.9 %) and some particular amount of GDD. The production of such optics is thus a demanding and challenging process. A number of characterization techniques are essential to provide feedback to the manufacturing process and to make sure that the produced optical elements meet the specifications. Some of these methods are needed also for the investigation of laser-induced damage in multilayer thin films. Here, we briefly describe the most relevant characterization techniques.

## 4.1 Spectrophotometry

Spectrophotometry is the quantitative measurement of the reflection or transmission properties of a material as a function of wavelength $\lambda$ [107]. We use a spectrophotometric approach to measure the transmission $T(\lambda)$ of produced thin film assemblies. Then the reflectivity $R(\lambda)$ can be estimated in the following way. When there is no optical gain in the material, the following relation holds due to energy conservation:

$$T + R + A + S = 1, \tag{4.1}$$

where $A$ and $S$ are the absorption and scattering coefficients, respectively. However, in the case of dielectric materials with large band gap $U_I$ compared to the photon energy $\hbar\omega$, i.e. $U_I \gg \hbar\omega$, the absorption is negligible $A \approx 0$. For samples with root mean square (RMS) surface roughness $\rho \ll \lambda$, the scattering is also negligible $S \approx 0$. Therefore, the reflectivity is simply:

$$R = 1 - T. \tag{4.2}$$

Figure 4.1 shows and example of a spectrophotometric measurement of the transmission of two dielectric mirrors having high reflectivity in the region from 1000 nm to 1200 nm.

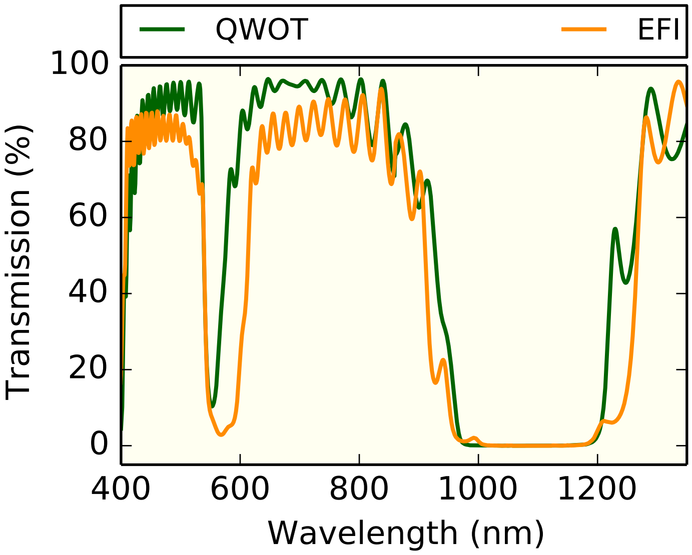

**Figure 4.1:** Example spectrophotometric measurement of the transmission of a QWOT stack (green curve) and a mirror optimized for electric field distribution (EFI) – orange curve.

Spectrophotometric measurements provide a good overall representation of the spectral performance of a thin-film assembly, and thus they provide fundamental feedback to the coating production. However, the accuracy of the reflectivity values obtained by this method is often limited to fraction of a percent ($\sim 0.1\,\%$). Better accuracy is provided by the ring-down technique for measurement of total losses.

## 4.2 Ring-down method for measurement of total losses

Let us imagine a light pulse travelling in an optical cavity. If the pulse has a narrow spectral bandwidth, we can safely ignore any effects related to dispersion. Then with each round trip, a fraction of the intensity of the pulse will be lost due to transmission, absorption, and scattering. It is intuitively clear that the pulse intensity will decay in a stepwise manner: the width of the step being equal to the round-trip time, and the step size – proportional to the total losses inside the cavity. If the losses are small, the decay will be exponential with time constant inversely proportional to the cavity total losses. A rigorous mathematical treatment of the above is given in Ref. [108]. Here, we will just give the final result for the total losses $L$:

$$L = T + A + S = \frac{l}{c\,\tau_c}, \tag{4.3}$$

where $l$ is the optical round-trip path, $c$ is the speed of light in vacuum, and $\tau_c$ is the decay time. By measuring the pulse intensity as a function of time $I(t)$ the decay time can be found as a fitting parameter:

$$I(t) = I(0)\, e^{-t/\tau_c}. \tag{4.4}$$

This method allows accurate measurements of mirrors with total losses on the scale of a few parts per million (ppm) [108]. On the down side however, Eq. (4.3) is only valid in the low-loss approximation when $L < 1\,\%$. Further limitations on the ring-down technique are imposed by the speed of the electronic equipment with which the decay time is measured, making cavities with total losses larger than $0.1\,\%$ difficult to measure.

## 4.3 Calorimetric absorption measurements

In the linear regime, absorption in dielectrics at optical frequencies is very low, provided that $U_I \gg \hbar\omega$. Nevertheless, hypothetically, absorption might take a notable part in the damage mechanism in the high average power. To confirm or disprove this supposition, absorption has to be measured when investigating the LIDT at high average power, as in the experiment described in Chapter 7.

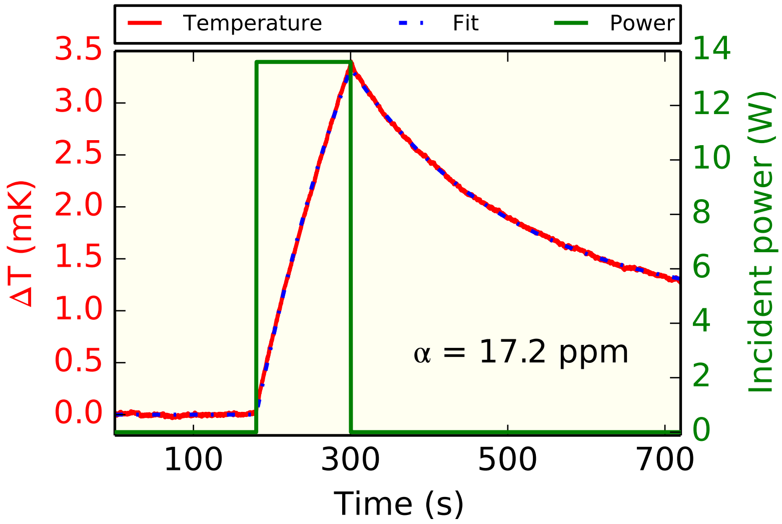

**Figure 4.2:** Example calorimetric measurement of absorption. The average power (green curve) and the temperature (red curve) are recorded as functions of time. Two exponential functions (blue dash-dot curve) are fitted to the measurement data: one when the the sample was illuminated with the laser beam and another after the beam was blocked.

There are three main approaches to determine the absorption losses [109]: by measuring transmission, while neglecting or accounting for losses due to reflection and scattering; by emissometry, because at thermal equilibrium, emittance is equal to absorbance; and by calorimetry, where the temperature increase due to the absorbed radiation is measured.

We used a commercially available calorimeter, which measures absorption losses according to ISO 11551 [110].

An example of a calorimetric measurement of absorption is shown in Fig. 4.2. The change in temperature $\Delta T$ of the sample and the average laser power incident on it are recorded as functions of time. Initially, the laser beam is blocked by a shutter. At some moment $t_0$ the beam is unblocked and illuminates the sample, which starts to heat up. At a moment $t_1$ the shutter is closed again and the sample begins to cool down. The function $\Delta T(t)$ can be fitted with an exponential function for the period of heating ($t_0 < t < t_1$) [111]:

$$\Delta T(t) = A_h + B_h\, e^{-\gamma t}, \tag{4.5}$$

where $A_h$, $B_h$, and $\gamma$ are fitting parameters. The period of cooling ($t > t_1$) can be fitted in a similar way. It can be shown that the absorption coefficient $\alpha$ is equal to [111]:

$$\alpha = \frac{\gamma C_{\text{eff}} A_h}{P}, \tag{4.6}$$

where $C_{\text{eff}}$ is the effective heat capacity and $P$ is the average laser power incident on the sample.

# Chapter 5

# Damage threshold metrology

The laser-induced damage is a sophisticated phenomenon. It depends not only on the properties of the material, such as the band gap, but also on various parameters of the beam: pulse duration, central wavelength, number of pulses, beam width, and, as it will be shown in Chapter 7, on repetition rate. All that makes laser-induced damage difficult to study, and comparisons to literature need to be carefully made. It is thus crucial to define the conditions under which a damage threshold value has been obtained. This Chapter aims to fulfill that purpose.

We studied the laser-induced damage in dielectrics at two different wavelengths: 800 nm and 1030 nm. In the first case, the pulse duration was 30 fs, whereas in the latter it was on the order of one picosecond. Because of the differences in the characteristics of the beam in both cases, we had to use two different set-ups sharing the same basic concept. Here, we shall describe the issues common to both set-ups. Details specific to each particular case will be given later.

## 5.1 Set-up scheme

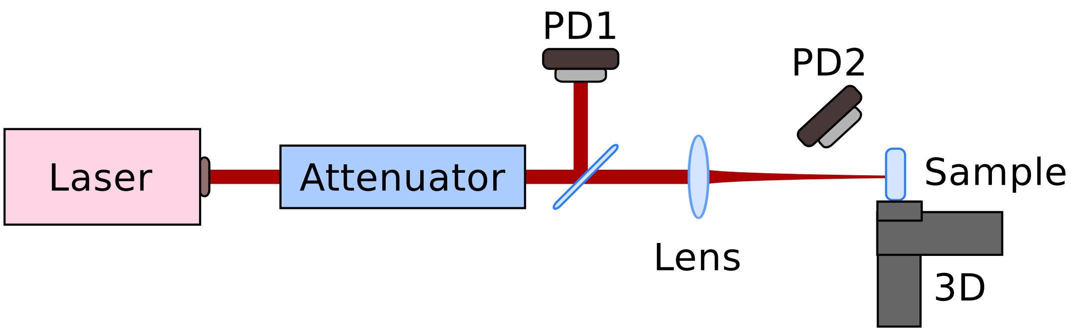

**Figure 5.1:** General scheme of a damage threshold set-up. PD1 – calibrated photodiode; PD2 – photodiode to measure scattered light; 3D – three dimensional translation stage.

A general scheme of a damage threshold set-up, valid for both set-ups, is given in Fig. 5.1. The laser beam passes through an adjustable attenuator, allowing control over the fluence illuminating the sample. Afterwards, a small part of the beam is separated and directed to a calibrated photodiode, which allows *in situ* measurements of the incident power. The rest of the beam is focused on the sample. A second photodiode is placed near the sample in order to detect damage, which would be indicated by a rapid increase of the scattered light coming from the surface of the sample, as explained in more detail in Section 5.2.

## 5.2 Measurement algorithm and definition of damage

To determine when damage occurred, a photodiode was placed near the sample to monitor the light scattered off its surface, as shown in Fig. 5.1. The sample was placed in the focal plane of the laser beam in such way that an undamaged site was irradiated (Fig. 5.2(a)) and the light scattered off the sample was monitored for a certain time interval. Then the fluence was increased and the scattered light was measured again for the same period of time, while illuminating the same spot on the sample. That routine was iterated to cover a certain fluence range, within which the damage threshold lay. The damage threshold was defined as the fluence at which the behavior of scattering signal with respect to laser fluence changed rapidly. As soon as damage occurred (Fig. 5.2(b)) the scattered signal increased rapidly (Fig. 5.3).

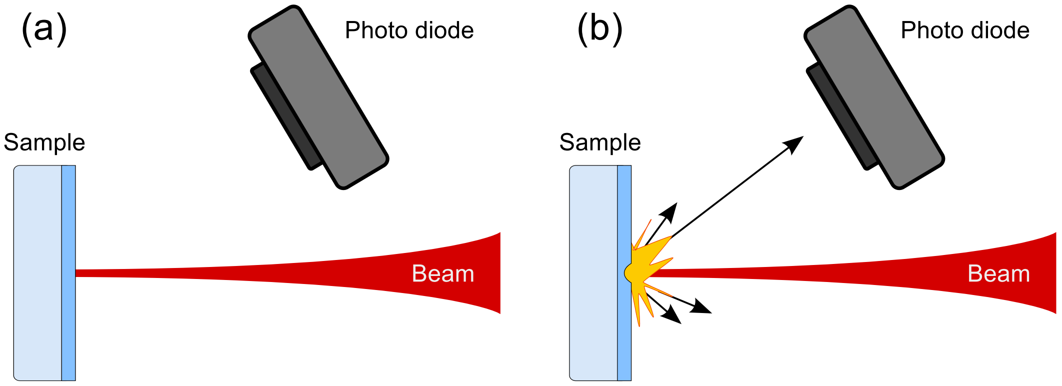

**Figure 5.2:** Damage detection by monitoring the scattered: (a) non-damaged site and low scattering; (b) damaged site, causing increased scattering.

A typical recording of scattering signal as a function of laser fluence is given in Fig. 5.3. The fluence value after which the scattering signal starts to grow rapidly defines the damage threshold fluence.

Scattered light has been used for damage detection successfully in the past [112–114] and is one of the damage detection methods recommended by ISO 21254:2011. It is worth

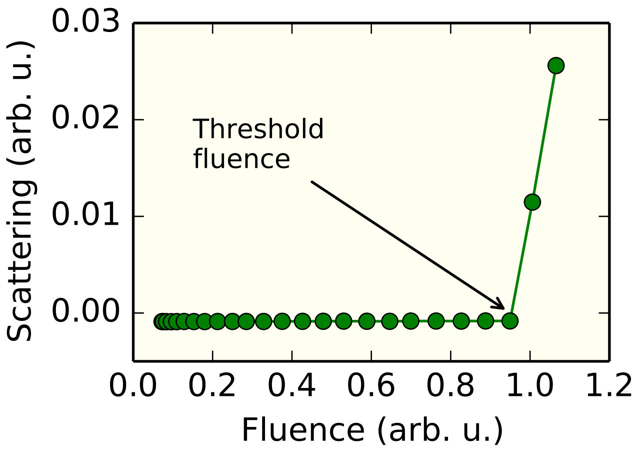

**Figure 5.3:** Scattering signal versus fluence: example damage threshold measurement. The arrow points to the fluence at which damage occurred.

noting however, that according to our measurement procedure, the same site of the sample is illuminated by a range of fluence values, whereas ISO 21254:2011 stipulates that the sample should be illuminated on a different site for each particular fluence value. That is being done in order to avoid various incubation effects [67, 112, 115, 116]. Since such preconditioning effects are part of the long term damage process, we consider that by embracing these incubation effects our measurements have actually yielded more realistic threshold values for damage, which occur under real conditions. Moreover, although our measurements are not ISO-compliant, the detailed description of the measurement procedure and the set-up allows the reproduction of the obtained results.

## 5.3 Calibration

The LIDT is usually given in units of fluence, which is defined as the energy possessed by an optical pulse divided by the area, over which this energy is distributed. The pulse energy can be obtained by dividing the average power carried by the beam on the repetition rate of the laser. To measure *in situ* the incident average power, we deflected a small portion of the beam to a photodiode (PD1 in Fig. 5.1), which was calibrated with an optical power meter in the beginning of every measurement session.

Figure 5.4 shows an example of a calibration of a photodiode. Since the measured average power $\bar{P}$ scales linearly with the voltage $U$ produced by the photodiode. By applying a linear fit to the measurement data, we obtain the fit parameters $a$ and $b$, which allow us to calculate the average power $\bar{P}$ from the measured voltage $U$:

$$\bar{P} = a + b\,U. \tag{5.1}$$

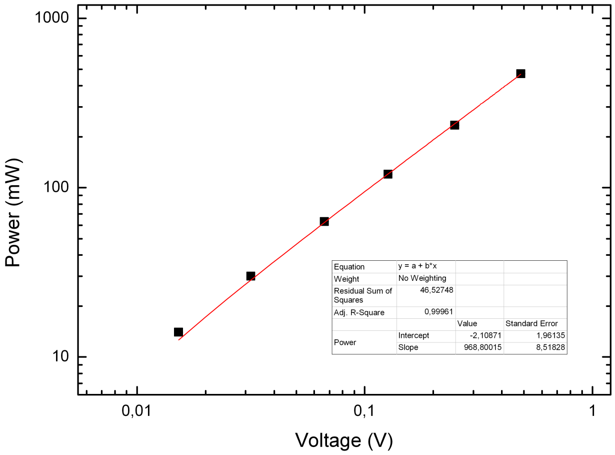

**Figure 5.4:** Example calibration measurement of the photodiode, allowing consequent *in situ* measurements of incident power.

If we divide the average power $\bar{P}$ on the repetition rate $f_{\mathrm{rep}}$, we will obtain energy per pulse.

## 5.4 Focus characterization

When characterizing the laser beam around the focal plane, we found that the foci of the two main axes of the beam did not coincide in space, which suggested astigmatism of the laser beam. That meant that the finding of a focus position with good rotational symmetry would be very challenging. Instead, we assumed that the beam had an elliptical profile with main axes, which were Gaussian in space.

For Gaussian beam propagating through a focus the variation of beam radius $w(z)$ is given by

$$w(z) = w_0\sqrt{1+\left(\frac{z-z_0}{z_R}\right)^2}, \tag{5.2}$$

where $z_0$ is the position of the focus, $w_0$ is the radius of the beam at the waist, and $z_R$ is the Raleigh length. In this work the radius of a Gaussian beam is taken as the distance from the optical axis in transversal plane at which the intensity drops down to a value of $1/e^2$ of the peak intensity.

We translated a CCD camera along the focus and measured the beam diameter with a step of 0.5 mm. By plotting the beam width versus the position along the $z$-axis and fitting it using Eq. (5.2), we were able to retrieve the beam parameters. An example measurement, fit and extracted beam parameters are shown in Figure 5.5.

In order to estimate the peak fluence of the incident beam, we calculated the area $A_\perp$

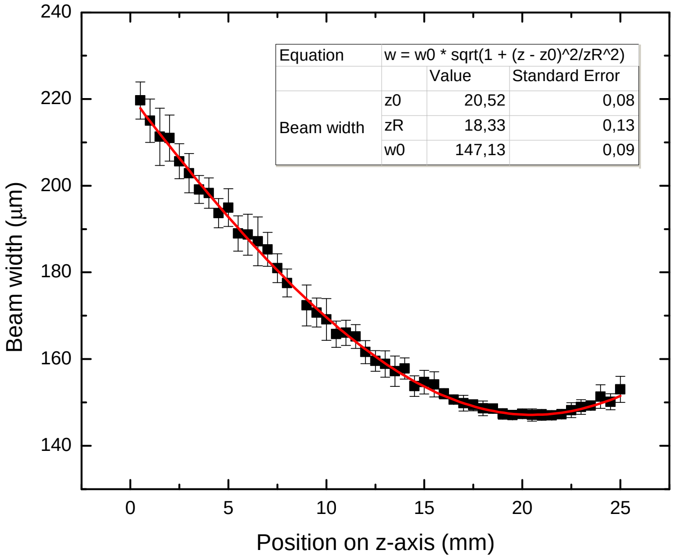

**Figure 5.5:** Measurement of the beam width across one of the foci. The experimental data was fitted with the Gaussian beam width $w(z)$ as a function of the axial distance $z$ (Eqn. 5.2).

of an elliptical cross section perpendicular to the propagation axis:

$$A_\perp(z) = \pi\, w_x(z)\, w_y(z), \tag{5.3}$$

where $w_x(z)$ and $w_y(z)$ are the two main axes of the ellipse at position $z$ along the beam.

However, the damage threshold set-up was able to perform measurements at an arbitrary angle of incidence $\theta$. For $\theta \neq 0$ the area of the sample $A$ illuminated by the beam is effectively larger than $A_\perp$. In order to take that into account, Eq. (5.3) has to be modified by introducing an additional term as follows:

$$A(z) = \frac{A_\perp(z)}{\cos\theta}. \tag{5.4}$$

The pulse energy, when divided by the area illuminated by the laser beam $A(z)$ determines the laser fluence at point $z$ on the optical axis, as shown in the next section.

## 5.5 Calculation of peak fluence

As mentioned previously in Section 5.3, in our set-up we actually measured the voltage $U$ yielded by a photodiode in order to determine the average power $\bar{P}$ of the incoming beam by using (5.1). To calculate then the peak fluence $\hat{J}$ the following expression could be used (see appendix A):

$$\hat{J} = 2\,\frac{\bar{P}}{f_{\mathrm{rep}}\, A_\sigma}, \tag{5.5}$$

where $f_{\text{rep}}$ is the repetition rate of the laser and $A_\sigma$ is the area of a circle with center on the optical axis and radius $w$.

However, as discussed previously, in our case the beam was astigmatic and we also corrected the area for an arbitrary angle of incidence. Thus, substituting (5.2) and (5.3) in (5.4) we obtained the following expression for the area illuminated by the beam at position $z$ on the optical axis:

$$A(z) = \frac{\pi}{\cos\theta}\, w_0^x \sqrt{1 + \left(\frac{z - z_0^x}{z_R^x}\right)^2}\; w_0^y \sqrt{1 + \left(\frac{z - z_0^y}{z_R^y}\right)^2}. \tag{5.6}$$

Note that indices $x$ and $y$ in superscript do not mean rise to power here. Rather they denote the corresponding parameters of the beam within the two main axes.

After inserting equations (5.1) and (5.6) in (5.5) we obtain the final expression for calculation of the peak fluence:

$$\hat{J}(z) = \frac{2(a + b\,U)\,\cos\theta}{f_{\text{rep}}\pi\, w_0^x \sqrt{1 + \left(\frac{z - z_0^x}{z_R^x}\right)^2}\; w_0^y \sqrt{1 + \left(\frac{z - z_0^y}{z_R^y}\right)^2}}. \tag{5.7}$$

This expression connects the photodiode calibration parameters $a$ and $b$, the focus characterization parameters $w_0$, $z_0$ and $z_R$, the repetition rate $f_{\text{rep}}$, and allows us to reconstruct the peak fluence from the voltage readings $U$ of the photodiode.

## 5.6 Measurement example

Let us summarize the damage threshold measurement process. First, to measure the incident power on the sample, a photodiode is calibrated according to Section 5.3. The calibration allows the retrieval of the linear parameters $a$ and $b$, which can be used to calculate the average power from the voltage values given by the photodiode (PD1 in Figure 5.1).

Afterwards, a certain range around the focus is scanned along the $z$-axis and the beam widths in two mutually perpendicular planes are recorded for each position. That way, by retrieving the beam parameters in $x$-$z$ and $y$-$z$ planes as shown in Section 5.4, it is possible to take into account the astigmatism of the laser beam.

Following the measurement algorithm described in Section 5.2, we gradually increase the initially low fluence while recording at each step the voltage signals given by both photodiodes: one measuring the incident power and the other monitoring the scattered light from the sample. The collected data is processed by substituting the previously determined parameters $a$, $b$, $w_0$, $z_0$ and $z_R$[1] into (5.7). The data evaluated in such way can be plotted as scattered signal versus fluence, and the threshold fluence can be determined visually from the resulting figure. An example of such damage threshold measurement is given in Figure 5.3.

---

[1] Parameters $w_0$, $z_0$ and $z_R$ were determined for two mutually perpendicular planes.

# Chapter 6

# Femtosecond optical breakdown of dispersive coatings

Ultrafast lasers are a versatile tool not only in science, but they also have many industrial as well as medical applications [9]. Ultrashort pulses have allowed scientists to explore ultrafast relaxation processes in the microcosm [10–12]. Few-cycle pulses have enabled time-resolved studies of molecular [13] and electron dynamics in molecules and atoms [16, 17]. More recently, researchers have also successfully used the optical field of ultrashort pulses to induce and control electric current in dielectrics [18–20]. Furthermore, currently the feasibility of using laser-driven ion accelerators as ion sources for cancer therapy is under active investigation [21–24]. This is promising, because the high peak intensities accessible by focusing energetic ultrashort pulses allow for more efficient energy transfer from laser photons to ions [25–27].

One of the major challenges in generation of ultrashort pulses is that it demands a laser beam with broad electromagnetic spectrum, the components of which have to be in phase with each other in order to form and maintain the shape of the pulse and its duration [28]. That in turn means that the spectral phase of the pulse has to be accurately controlled and the dispersion gained during propagation through a dispersive medium has to be compensated. An appealing way to do that is offered by dispersive mirrors [32–34]. Their advantages include: (i) relative alignment simplicity [37], (ii) ability to control dispersion over a broad spectral range [38, 39] and (iii) low losses for narrow-band applications [37, 40].

In this Chapter, we investigate the ultrashort pulse damage in single layer coatings of metals and dielectrics, in quarter-wave optical thickness (QWOT) stacks, and in dispersive mirrors. Particular attention is paid to dispersive mirrors, because of their widespread usage in ultrafast science, on one side, and because of the scarcity of literature on LIDT of dispersive mirrors, on the other. These results were also published in Ref. [117].

## 6.1 Samples

We investigated high-reflectors, dispersive mirrors, a fused silica substrate and single layer coatings of metal and dielectric materials. All of the sample designs were coated on fused silica substrates with 25 mm diameter and 6 mm thickness. Information about the different coatings is summarised in Table 6.1. The metal coatings were deposited using electron beam evaporation (EB), whereas the dielectric coatings were produced using plasma-ion assisted magnetron sputtering (MS).

| Sample name | Materials | Layers | Thickness (nm) | Process | LIDT (J/cm$^2$) |
|---|---|---|---|---|---|
| *Single layer dielectric coatings:* | | | | | |
| $Ta_2O_5$ (80 %) | 80 % $Ta_2O_5$/20 % $SiO_2$ | 1 | 320 | MS | $0.41 \pm 0.04$ |
| $Ta_2O_5$ (90 %) | 90 % $Ta_2O_5$/10 % $SiO_2$ | 1 | 300 | MS | $0.35 \pm 0.04$ |
| $Ta_2O_5$ | $Ta_2O_5$ | 1 | 300 | MS | $0.31 \pm 0.03$ |
| $Nb_2O_5$ | $Nb_2O_5$ | 1 | 300 | MS | $0.23 \pm 0.02$ |
| $SiO_2$ | $SiO_2$ | 1 | 400 | MS | $1.14 \pm 0.10$ |
| *Metal coatings:* | | | | | |
| Silver | Ag | 1 | 120 | EB | $0.25 \pm 0.03$ |
| Gold | Au | 1 | 120 | EB | $0.22 \pm 0.02$ |
| *High reflectors:* | | | | | |
| HDT1 | 80 % $Ta_2O_5$/$SiO_2$ | 41 | 5000 | MS | $0.34 \pm 0.03$ |
| HDT2 | $Ta_2O_5$/$SiO_2$ | 41 | 4700 | MS | $0.25 \pm 0.03$ |
| *Dispersive mirrors:* | | | | | |
| HD63 | $Ta_2O_5$/$SiO_2$ | 63 | 9680 | MS | $0.26 \pm 0.03$ |
| HD64 | $Ta_2O_5$/$SiO_2$ | 39 | 10 460 | MS | $0.35 \pm 0.04$ |
| HD72 | $Ta_2O_5$/$SiO_2$ | 40 | 10 175 | MS | $0.36 \pm 0.04$ |
| HD73 | $Ta_2O_5$/$SiO_2$ | 71 | 10 990 | MS | $0.25 \pm 0.03$ |
| RHD5 | $Ta_2O_5$/$SiO_2$ | 67 | 11 300 | MS | $0.25 \pm 0.03$ |
| PC49_C | $Nb_2O_5$/$SiO_2$ | 89 | 8260 | MS | $0.25 \pm 0.03$ |
| PC60_S | $Nb_2O_5$/$SiO_2$ | 88 | 12 530 | MS | $0.29 \pm 0.03$ |
| PC60_L | $Nb_2O_5$/$SiO_2$ | 84 | 12 140 | MS | $0.27 \pm 0.03$ |

**Table 6.1:** General description and breakdown threshold fluences of the studied samples. The given thicknesses are physical.

Single layer depositions of $Nb_2O_5$, $Ta_2O_5$ and $SiO_2$ as well as mixtures of the latter two were investigated in terms of LIDT. The mixtures of $Ta_2O_5 : SiO_2$ had ratios of $80 : 20$ and $90 : 10$ and are denoted here as $Ta_2O_5$ 80 % and $Ta_2O_5$ 90 %, respectively.

Both the silver and the gold coatings had physical thicknesses of about 120 nm and were deposited using electron beam evaporation. The samples designed as highly reflecting mirrors, i.e. HDT1 and HDT2, consisted of a QWOT stack with $Ta_2O_5$ 80 % and $Ta_2O_5$ as high refractive index materials, respectively.

$SiO_2$ was used as low refractive index material for all of the dielectric mirrors presented here. Some of the dispersive coatings employed $Ta_2O_5$ as high refractive index material, whereas for others $Nb_2O_5$ was used, depending on the desired performance of the particular coating.

The goal of a dispersive coating is to control the spectral phase of a pulse. This functionality is achieved by a combination of wavelength dependent penetration and resonance effect of Gires-Tournois cavities. Both of these effects influence significantly the electric field distribution inside of the layer stack. Thus generally dispersive mirrors possess much more complicated electric field distribution in comparison to quarter wave thickness stacks. An example of electric field distribution inside a dispersive coating is shown in Figure 3.3.

Each sample among the dispersive mirrors had a unique design in order to meet the specific requirements of the experiment for which it was intended. Thus the electric field distribution inside the layer stack varied significantly from one dispersive sample to another.

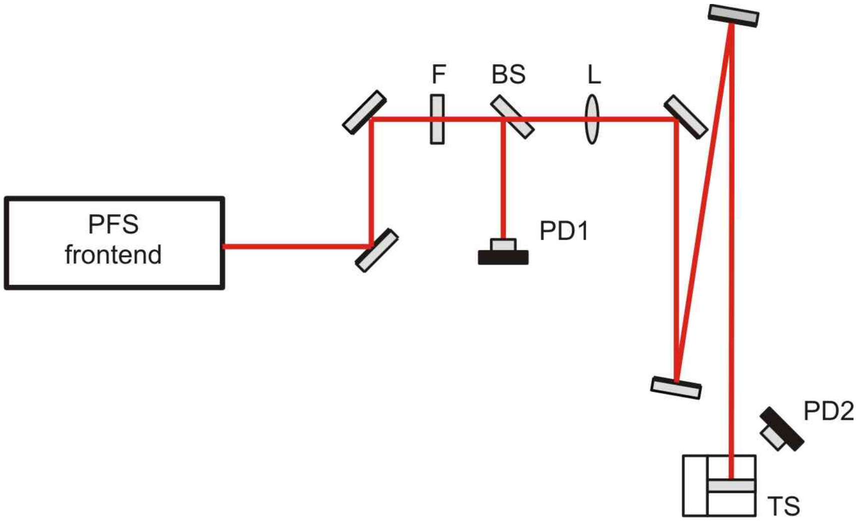

**Figure 6.1:** Layout of the set-up: F – gradient neutral density filter wheel; BS – beam splitter; L – 1500 mm convex lens; PD1 – calibrated photodiode; PD2 – photodiode to detect scattered light; TS – 3D translation stage (reprinted from [119]).

## 6.2 Set-up

To measure the threshold of laser-induced damage we used an experimental set-up, which was developed previously within the framework of a bachelor thesis [119]. Its layout is given in Figure 6.1. The beam first went through a motorized filter wheel with an azimuthal gradient distribution of the optical density. By rotating the filter wheel we were able to control the illuminating fluence on the sample. After passing the neutral density filter, a small part of the beam was reflected by the beam splitter. It was then sent to a calibrated photodiode, which allowed us to measure *in situ* the incident power. The rest of the beam was focused on the sample. A second photodiode was placed near the sample in order to detect the occurrence of damage indicated by a rapid increase of the scattered light coming from the surface of the sample, as explained in more detail in Section 5.2.

As a laser source we have used the front end of the Petawatt Field Synthesizer (PFS) system which is currently under development at the Max Planck Institute of Quantum Optics. The main goal of the PFS project is to deliver few-cycle laser pulses ($\sim 5$ fs with spectrum spanning from 700 nm to 1400 nm) with energies larger than 3 J at a repetition rate of 10 Hz and with controlled carrier-envelope phase [120].

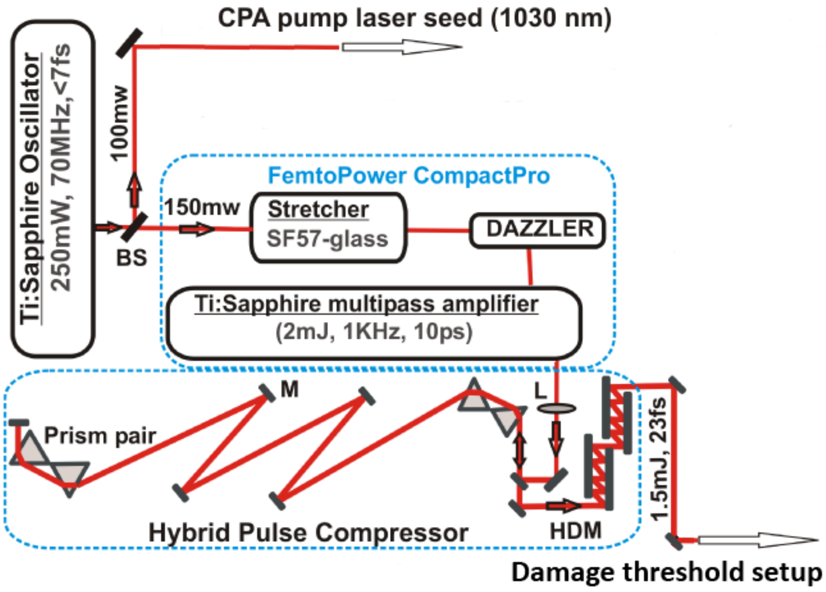
CPA pump laser seed (1030 nm)
Ti:Sapphire Oscillator
250mW, 70MHz,<7fs
100mw
FemtoPower CompactPro
150mw
BS
Stretcher
SF57-glass
DAZZLER
Ti:Sapphire multipass amplifier
(2mJ, 1KHz, 10ps)
M
L
Prism pair
1.5mJ, 23fs
Hybrid Pulse Compressor
HDM
Damage threshold setup

**Figure 6.2:** Layout of the relevant part of the PFS front end system (shortened from [120]).

However, only a small portion of the power mentioned above was sufficient for the carried-out damage threshold measurements. Thus, only a part of the whole PFS system was used as a laser source. It delivered to the damage threshold set-up pulses with energy of 1 mJ and pulse duration of about 30 fs at central wavelength of 790 nm with a repetition rate of 500 Hz. A schematic layout of the relevant part of the PFS front end is shown in Figure 6.2.

By having a maximal pulse energy of 1 mJ and a focal spot on the sample with diameter of about 140 µm measured at level $1/e^2$ of the maximal intensity, we were able to reach fluences of up to 13 J/cm$^2$.

## 6.3 Results and discussion

This section presents the results from the damage threshold measurements with femtosecond pulses. The measured threshold fluences are divided into four groups in order to expose the different findings and dependencies of the damage threshold on various factors.

### 6.3.1 Single layer depositions

We investigated the dependence of the threshold of damage induced by ultrashort pulses on the band gap of the materials. For that purpose we measured the damage threshold of single layer coatings of $Nb_2O_5$, $Ta_2O_5$ and $SiO_2$. The respective band gaps and refractive indices of these materials are given in Table 6.2. Additionally, single layer mixtures of $Ta_2O_5$ and $SiO_2$ in ratios 80 : 20 and 90 : 10 were also measured. The optical breakdown thresholds of single layer depositions are shown in Fig. 6.3.

| Material | $E_g$ (eV) | $n_0$ |
|---|---|---|
| $Nb_2O_5$ | 3.4 [121] | 2.25 |
| $Ta_2O_5$ | 3.8 [68] | 2.10 |
| $SiO_2$ | 8.3 [68] | 1.45 |

**Table 6.2:** Band gap energies ($E_g$) and refractive indices at 800 nm ($n_0$) of the investigated materials.

It must be noted that the samples coated using mixtures—$Ta_2O_5$ 80 % and $Ta_2O_5$ 90 %—were produced by simultaneous sputtering of pure targets of $Ta_2O_5$ and $SiO_2$ at different rates in order to obtain the desired proportion. The dielectric response of these mixtures can be described by applying an effective-medium approximation which is valid if the wavelength is much larger than the grains of pure material in the mixture [70]. The effective band gap of such compound material increases with increase of the concentration of $SiO_2$. Thus, for example, a single layer of $Ta_2O_5$ 80 % has larger band gap than a single layer of $Ta_2O_5$ 90 %.

As evident from Fig. 6.3, for ultrashort pulses the laser-induced damage threshold is proportional to the band gap of the material. This is in agreement with previously reported results by others [68, 113]. Also, the values of the threshold fluences for the fused silica substrate and deposited single layer of $SiO_2$ were close to each other, suggesting good quality of the deposition process.

### 6.3.2 Dispersive mirrors versus their high-index materials

Based on the results obtained for single layers, given in Section 6.3.1, one can draw a conclusion that in a multilayer thin-film structure the high-index layers are the weak spot

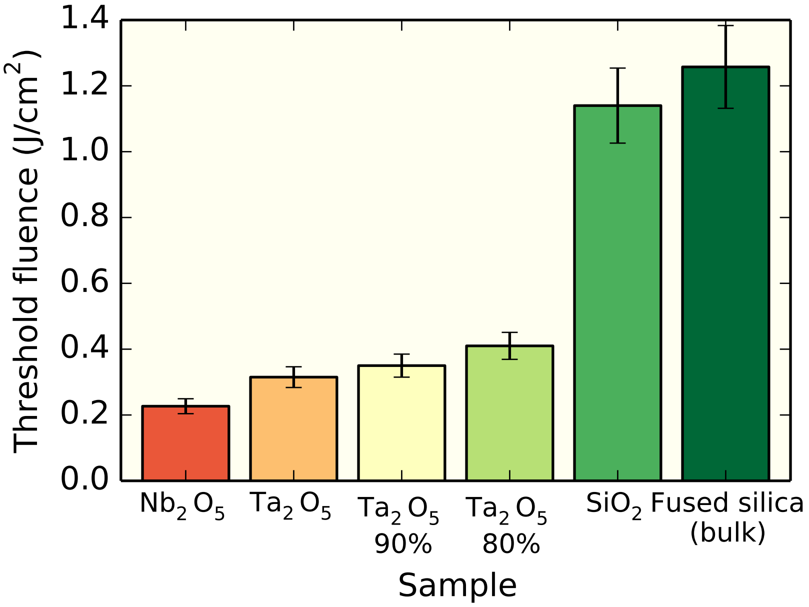

**Figure 6.3:** Threshold fluences of single layer depositions and fused silica substrate.

of a layer stack in terms of damage threshold. Therefore we measured and compared the damage threshold values of various dispersive mirrors produced using the same high-index materials, but with different designs. They were also compared to the damage threshold of a single layer of the high refractive index material used to compose that set of dispersive mirrors.

Figure 6.4 shows two sets of such comparisons. $Nb_2O_5$ was used in the dispersive coatings shown in Figure 6.4(a), whereas $Ta_2O_5$ was used for the coatings shown on Figure 6.4(b). As seen in the figure, the damage threshold of the dispersive coatings is close to that of a single layer of the respective high refractive index material used. In the case of $Nb_2O_5$ the breakdown threshold of the single layer coating was actually a bit lower than that of dispersive mirrors employing that material. One of the reasons for that might be the lower quality substrate used for that particular coating.

Each of the mirrors shown in Figure 6.4 was intended for a different experiment than the others, meaning that each had a separate combination of reflectivity bandwidth, central wavelength and GDD. For instance, the "PC" mirrors have been designed to support broad spectral bandwidth and function by employing mainly the wavelength dependent penetration effect described in Section 3.1. In contrast, the "HD" mirrors support a narrow bandwidth of only few tens of nm and exploit dominantly the resonance effect to reach high values of GDD per reflection. As shown in Fig. 3.2 in Section 3.1, the resonance effect results in field enhancement inside the multilayer stack for the resonance frequency. Furthermore, there are major differences between the members of each mirror family: mirrors PC60_S

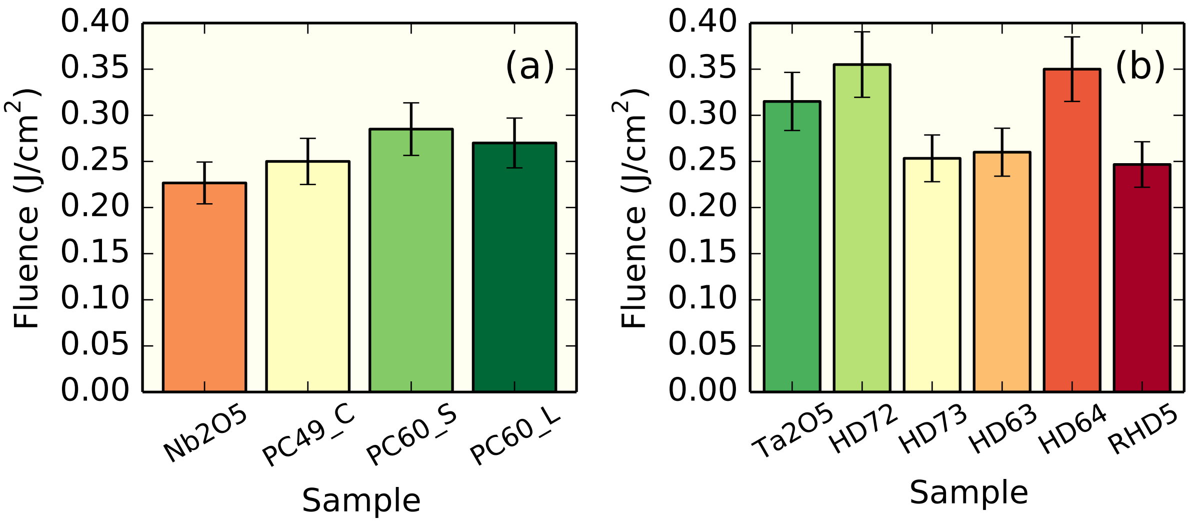

**Figure 6.4:** Comparisons between: (a) a single layer of $Nb_2O_5$ and dispersive coatings employing $Nb_2O_5$ as high- and $SiO_2$ as low index materials, respectively; (b) a single layer of $Ta_2O_5$ and dispersive coatings of $Ta_2O_5/SiO_2$.

and PC60_L constitute a complementary pair[1], whereas PC49_C is a standalone dispersive mirror. We studied mirrors with so much different layer compositions to illustrate the dependence of LIDT on the electric field distribution.

On one hand, each of the studied dispersive mirrors had unique layer structure and therefore unique electric field distribution for the central frequency. On the other hand, all dispersive mirrors made with the same pair of materials have demonstrated similar LIDT. Therefore, it would be easy to conclude that the LIDT of dispersive mirrors in the femtosecond regime does not depend on the electric field distribution. The problem with this picture is that a Gaussian pulse as short as 30 fs must have spectrum spanning more than 14.6 THz, while the electric field distribution inside a dispersive mirror can vary significantly for two separate frequencies from such bandwidth. In fact, dispersive mirrors work thanks to the different pathways of different frequencies (Fig. 3.3). Clearly, this invalidates the single frequency approximation. Instead, the LIDT of dispersive mirrors should be studied as a function of time-domain electric field distribution.

### 6.3.3 QWOT stacks versus their high-index materials

It was shown in Section 6.3.1 that the damage threshold scales with the band gap of the material and the results presented in Section 6.3.2 suggest that the damage threshold of a dispersive coating is constrained by the band gap of the high-index material. By mixing two materials during the deposition process, however, one can obtain layers with custom refractive indices and respectively, band gaps. Thus, it would be of interest to see if the damage threshold of a layer structure as a whole can be influenced by using a mixture of materials for the high-index layers.

---

[1] The complementary mirror pair approach to dispersion compensation is discussed, e.g., in Ref. [122].

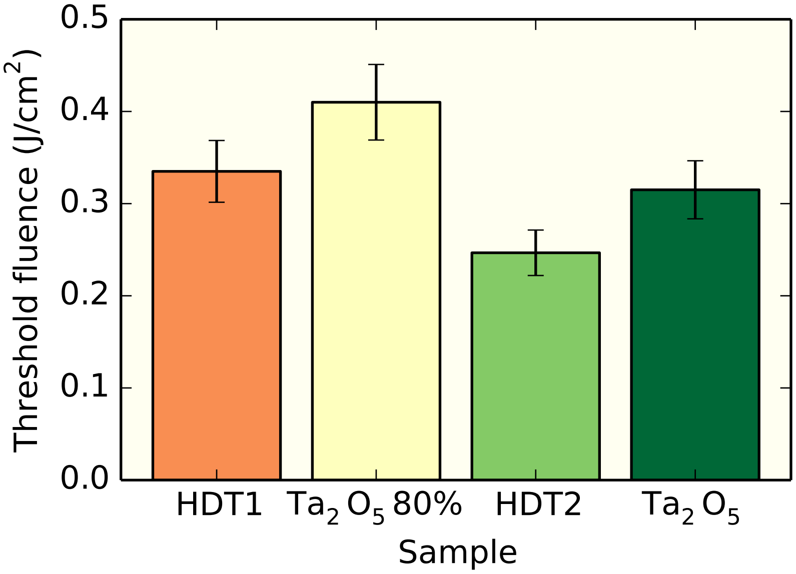

**Figure 6.5:** Threshold fluences of QWOTs compared to that of single layer depositions of different high-refractive index materials.

In order to estimate the effect of mixing the high refractive index material (in this case it was $Ta_2O_5$) with $SiO_2$ on the damage threshold of standard QWOT stacks, we coated designs where the initially pure high refractive index material was mixed with $SiO_2$. Then we measured the LIDT of this special coating and compared it with the LIDT of a QWOT consisted of layers of pure $Ta_2O_5$ and $SiO_2$.

In Figure 6.5 the threshold fluences of two QWOT stacks, i.e. HDT1 and HDT2, are compared with the single layers of the corresponding high index materials ($Ta_2O_5$ 80 % and $Ta_2O_5$).

Two observations could be made here. First, the produced high reflectors have damage thresholds close to that of the respective high-index materials which are used for their production. Second, comparing the threshold fluences of the two QWOT stacks, it can be seen that the one employing the $Ta_2O_5$ 80 % mixture as high index material, i.e. HDT1, has about 20 % larger damage threshold. Such improvement of the breakdown threshold of a thin-film structure by mixing the high index material with $SiO_2$ has been reported previously [70, 123].

However, the refractive index of the mixture becomes smaller as the concentration of $SiO_2$ in it increases, which effectively reduces the contrast ratio between the refractive indices of $Ta_2O_5$ and $SiO_2$. In turn this affects the achievable performance such as reflectivity bandwidth and GDD. Thus, the approach of mixing the high refractive index material with $SiO_2$ can be applied only to some certain extent and only in cases, where the application does not impose great demands on the performance of the coating.

### 6.3.4 Metal versus dielectric mirrors

It is often thought in high-power laser community that metallic mirrors have damage threshold of about an order of magnitude lower compared to dielectric ones. That way of thinking comes from experience with pulses longer than some tens or hundreds of picoseconds. Indeed, in that regime, metal mirrors damage much earlier than dielectric ones [124]. However, this might not be the case in the ultrafast regime when the pulse duration is of the order of tens of femtoseconds.

To test if such a dramatical difference in damage thresholds of metallic and dielectric mirrors still holds for femtosecond pulses, we measured both types of mirrors in our set-up. A comparison between the optical breakdown thresholds of metal and dielectric coatings is shown in Figure 6.6.

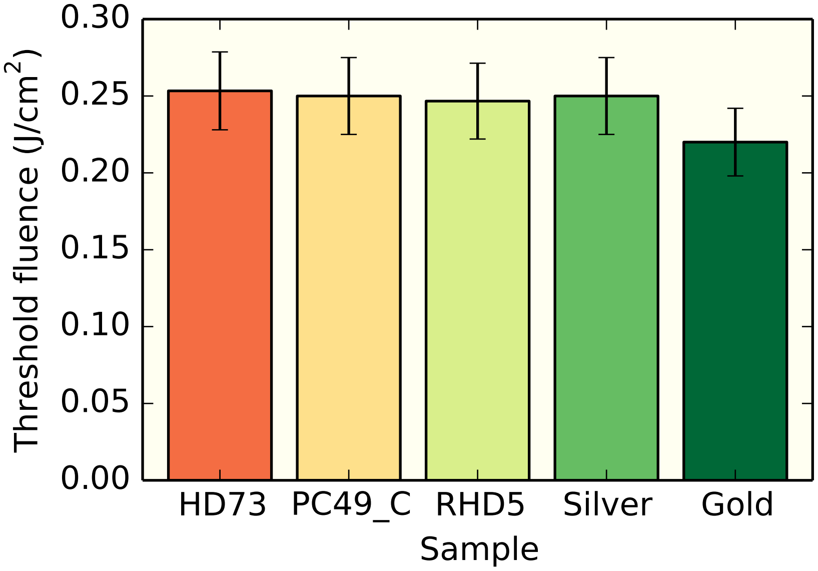

**Figure 6.6:** Comparison between the threshold fluences of metal and dielectric mirrors.

As evident from our measurements with femtosecond pulses the damage threshold of metallic mirrors was found to be comparable and in fact very similar to the damage threshold of dielectric mirrors. This small difference between damage thresholds of both types of coatings was an important finding, because previous studies of laser-induced damage for pulse duration in the order of 0.1 ns show a significantly larger difference between the breakdown thresholds of metals and dielectrics [124].

The reason why the difference in LIDT between metal mirrors and dielectric ones becomes smaller at shorter pulse durations, must be related to the different damage mechanisms of the two types of material. While the breakdown in metals is caused by absorption of laser light, heating up, and subsequent melting, the breakdown in dielectrics is more complicated and involves initial ionization until a critical density of electrons in the conduction band is reached. The possible mechanisms of ionization include MPI, tunneling, and avalanche ionization. As shown in Section 2.3, Eq. (2.36), the critical density of electrons in the conduction band depends on the frequency of the laser field and on the effective electron mass in the dielectric. For fused silica at 800 nm, the critical density is of the order of $10^{21}\,\mathrm{cm}^{-3}$. When it is reached, the plasma frequency becomes equal to the laser frequency and the formed plasma starts to absorb strongly the incident light leading to ablation. Peak intensities sufficient to reach the critical density of electrons in the conduction band are attained at much higher fluences for pulse durations of the order of 100 ps or longer than for pulse durations of the order or 30 fs. On the other hand, metals absorb the same fraction of the laser fluence disregarding the pulse duration. Because of this, the LIDTs of metal and dielectric mirrors differ much less when measured with femtosecond pulses than when they are measured with pulses in the order of hundreds of picoseconds.

### 6.3.5 Precision of the damage threshold measurements

The measurements were conducted in different sessions spread across several months. By the date of writing, the laser system was still under development and in order to operate properly, alignment adjustments were required on a daily basis. Such realignments led to a slightly different path of the beam in the damage threshold set-up, which in turn meant that our set-up had to be aligned before each measurement session. All of the above resulted in slightly different calibration parameters and focus position, leading to a systematic day-to-day error of up to 10 %.

## 6.4 Conclusion

This Chapter presents a systematic study of dispersive mirrors in terms of femtosecond LIDT. The LIDT measurements were carried out using 30 fs pulses coming out of a Ti:Sapphire system with spectrum centered at 790 nm and repetition rate of 500 Hz. The laser beam was focused down on the samples to a relatively large spot size of 140 µm. The experimental set-up and the measurement procedure were described in detail, allowing one to trace and understand how the results were obtained.

The LIDT of various single layer metal and dielectric coatings, QWOT stacks, as well as a number of dispersive mirrors were measured and compared. The damage threshold of single layer dielectric coatings was found to be dependent on the band gap of the material used. Both QWOT stacks and dispersive coatings had damage thresholds close to that of a single layer of the high index material used for the respective coating. In addition, using layers of a mixture between a high-index material ($Ta_2O_5$) and a low-index material ($SiO_2$) was found to increase the LIDT of the coating. Finally, the difference between the breakdown thresholds of metal mirrors with respect to that of dielectric ones was found to be much smaller compared to previous measurements, conducted with nanosecond pulses.

On one hand, both dispersive coatings and QWOT stacks have damage thresholds close to the damage threshold of a single layer of the used high-index material, on the other hand the LIDT of single layers was found to be proportional to the band gap of the material. Therefore in order to increase the LIDT of the coating, one has to choose materials with broad band gaps. However, materials with broader band gaps have lower refractive indices and the usage of such materials in a thin-film coating results in lower refractive index contrast and therefore in lesser achievable combination of bandwidth, reflectance and dispersion. Hence a compromise must be sought and mixing the high-index material with a low-index material would allow one to fine-tune the band gap and thus to obtain the right balance between the LIDT of a multilayer thin-film coating and its performance.

# Chapter 7

# Picosecond optical breakdown at MHz and kHz rates

The weakest parts of ultrafast laser systems with respect to laser-induced damage are often the multilayer mirrors. This fact has motivated extensive studies of ultrashort-pulse-induced optical breakdown of thin-films [66, 68–70, 72, 73]. All of them have been carried out by measuring the damage threshold at a low average power, either in single-shot mode or by using a pulse train at a kHz repetition rate.

However, recently developed oscillators and amplifiers, based on fiber [41], innoslab [42, 43], and thin-disk technology [44–46], are capable of generating subpicosecond pulses with energies of several tens of µJ at repetition rates of more than 10 MHz, resulting in several hundreds of watts of average output power and multiple megawatts of peak power. Optical damage is among the challenges towards scaling up the power of such systems. Moreover, their output is often intensified further in regenerative amplifiers [47], OPA stages [48], and inside enhancement cavities [50, 51]. The latter can reach average intracavity power of several tens of kW, which is limited by the damage threshold of optical coatings [50, 52].

The straightforward way to deal with optical breakdown is to increase the beam size. However, that requires larger optics and increases the overall footprint of the system, hence the costs rise substantially. In addition, the larger the size of the optics, the more difficult it becomes to provide uniform surface quality. Furthermore, the damage threshold of the whole optical element is as low as the damage threshold of its weakest spot. Thus, before undertaking the approach of increasing the size of the optical components, it would be beneficial first to try to increase their damage threshold. It is essential, therefore, to study the ultrafast damage behavior of thin-films not only in the single-shot and kHz repetition rate regimes, but also for MHz repetition rates at high average power.

In this chapter, we explore the dependence of MHz ultrashort pulse damage threshold of multilayer thin-films on the band gap and on the electric field distribution. We demonstrate that by suppressing the electric field in high-index layers and shifting its maxima to low-index layers the damage threshold can be increased by 30 %. We also give a criterion for optimal electric field distribution. In addition, we compare the results obtained at MHz rate with measurements performed at kHz repetition rate. This will allow us to study any possible influence of thermal or other incubation effects related to the high repetition rate, which might play an essential role in MHz-rate laser-induced damage.

Part of the research presented in this chapter, namely the part on MHz-rate optical breakdown was published in Ref. [125].

| Sample | Materials | Design | Process | Layers |
|---|---|---|---|---|
| *High-reflectors ($R > 99.9\,\%$):* | | | | |
| $TiO_2$ | $TiO_2/SiO_2$ | QWOT | EB | 33 |
| $Ta_2O_5$ | $Ta_2O_5/SiO_2$ | QWOT | EB | 35 |
| $HfO_2$ | $HfO_2/SiO_2$ | QWOT | EB | 43 |
| $Al_2O_3$ | $Al_2O_3/SiO_2$ | QWOT | MS | 71 |
| *NBP filters:* | | | | |
| C-$TiO_2$ | $TiO_2/SiO_2$ | NBP | EB | 33 |
| C-$Ta_2O_5$ | $Ta_2O_5/SiO_2$ | NBP | EB | 35 |
| C-$HfO_2$ | $HfO_2/SiO_2$ | NBP | EB | 43 |
| *EFI coatings:* | | | | |
| EFI-$TiO_2$ | $TiO_2/SiO_2$ | EFI | EB | 33 |
| EFI-$Ta_2O_5$ | $Ta_2O_5/SiO_2$ | EFI | EB | 35 |

**Table 7.1:** General description of samples studied with picosecond pulses. The narrow-band pass (NBP) samples were designed to have enhanced electric field inside a high-index layer and were expected to have lower LIDT. Contrariwise, the electric field optimized (EFI) samples were designed with a suppressed electric field inside the high-index layers with intention to increase their LIDT. All of the investigated coatings were prepared using EB, except for the $Al_2O_3$ QWOT stack for which MS technique was used.

## 7.1 Samples

We investigated the laser-induced damage of three different sets of samples, summarized in Table 7.1. All of them were multilayer thin-film compositions, where $SiO_2$ was used as the low-index material in each coating and the high-index material was $TiO_2$, $Ta_2O_5$, $HfO_2$, or $Al_2O_3$.

The first set consisted of QWOT stacks made using $SiO_2$ and one of each of the aforementioned high-index materials. A typical design of a QWOT stack can be represented by the formula:

$$(HL)^m H, \tag{7.1}$$

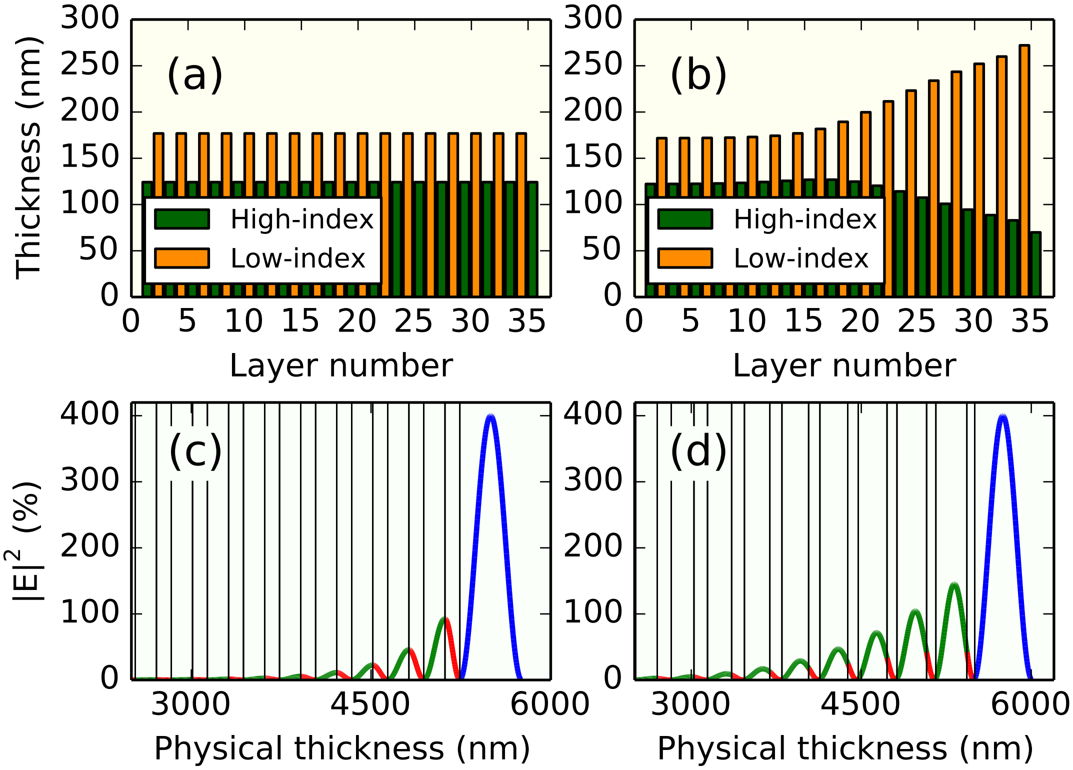

**Figure 7.1:** (a) and (b): Layer thickness profile of a QWOT stack of $Ta_2O_5/SiO_2$ (a) and of a layer stack of $Ta_2O_5/SiO_2$ with reduced electric field intensity (EFI) inside the $Ta_2O_5$ layers (b). (c) and (d): Electric field distributions inside of (a) and (b), respectively. The electric field inside $L$ and $H$ layers is represented accordingly by green and red sections, whereas the field in the incident medium is colored in blue.

where $m = 17$, and $H$ and $L$ denote high- and low-index layers respectively. The layer thickness profile of this 35-layer QWOT stack of $Ta_2O_5/SiO_2$ is given in Fig. 7.1(a) and the electric field distribution inside such stack is given in Fig. 7.1(c). To check whether thermal effects play an important role in the ultrashort-pulse damage process at high repetition rate, we measured absorption and the total losses of the QWOT samples (Fig. 7.2). The absorption was measured using a calorimetric approach [110] (see Section 4.3), whereas the total losses were measured using a cavity ring-down technique [108, 126] (see Section 4.2).

The second set contained NBP 33-layer filters, described by the formula:

$$(HL)^n 2H(LH)^n, \tag{7.2}$$

where $n = 8$. The only difference between the QWOT stacks and the NBP filters was a cavity high-index layer in the middle of the stack with half-wave optical thickness. At the central wavelength the electric field inside the cavity layer is significantly enhanced.

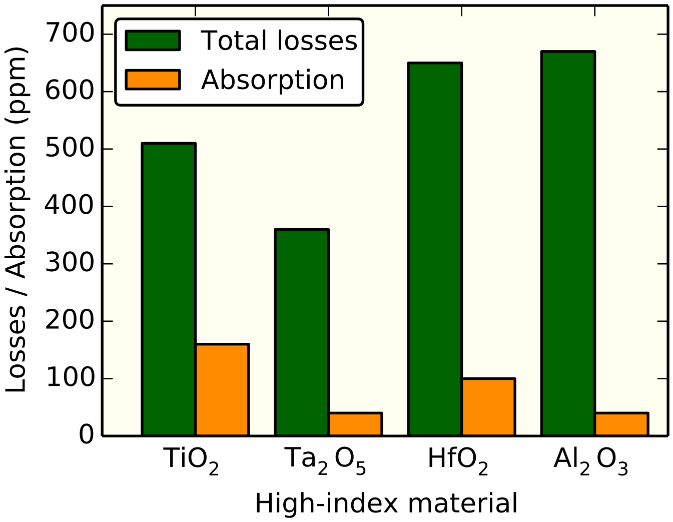

**Figure 7.2:** Absorption and total losses of the QWOT stacks, on which damage threshold measurements were performed.

Therefore, these NBP samples were expected to have lower damage threshold than the QWOT stacks made of the same pair of materials.

The samples in the third set were designed in such way that the electric field within the high-index layers was suppressed and its maxima were shifted to the low-index layers (Fig. 7.1(d)). Dielectric thin-film structure with such electric field distribution was expected to have higher damage threshold than a QWOT, since materials of lower refractive index materials have broader band gaps and previous studies in the ultrashort pulse regime have shown that the breakdown threshold of dielectrics scales with their band gap [68]. The design of these EFI coatings was found numerically by using the commercially available software OptiLayer [127] The resulting layer thickness profile is displayed in Fig. 7.1(b) and its electric field distribution is depicted in Fig. 7.1(d). The obtained EFI design was rather similar to another one, which was retrieved by an analytical approach to the same problem [128].

## 7.2 Measurement set-up and laser sources

### Set-up

The set-up used for damage threshold measurements with picosecond pulses is depicted in Fig. 7.3. The intensity of the incoming beam was controlled by rotating a half-wave plate mounted on a motorized stage and a thin-film polarizer. A small portion of the beam was then deflected to a calibrated photodiode, allowing us to measure *in situ* the incident power. The main part of the beam was focused on the sample down to 25 µm in diameter measured at level $1/e^2$ from the peak intensity, using an antireflection coated spherical lens with 70 mm focal length. A second photodiode was placed near the sample to monitor the light scattered off its surface. An abrupt change in the scattering behavior of the sample was used as an indicator of damage. This method has been applied successfully in the past [112, 114] and is one of the damage detection methods recommended by ISO 21254-4:2011.

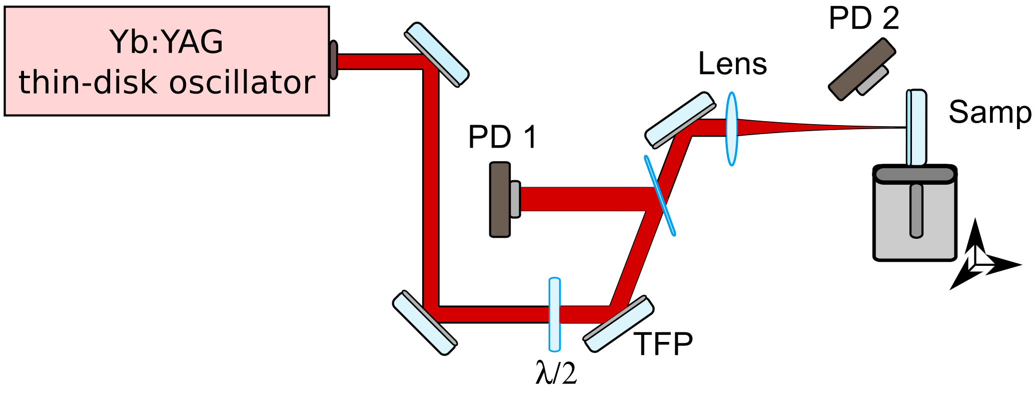

**Figure 7.3:** Measurement set-up: PD – photodiode, $\lambda/2$ – half-wave plate, TFP – thin-film polarizer.

The sample was placed in the focal plane of the laser beam in such way that an undamaged site was irradiated and the light scattered off the sample was monitored for a certain time interval (typically a second). Then the fluence was increased and the scattered light was measured again for the same period of time, while illuminating the same spot on the sample. That routine was iterated until a rapid increase of the scattered light occurred, which designated damage.

It is worth noting that the measurement procedure described in the previous paragraph differs from the recommended by ISO 21254:2011, where the laser beam is positioned on a separate site on the sample for each fluence value. This is done in order to avoid various incubation effects [67]. Since in our case more than 11 million pulses hit the sample each second and incubation effects are part of the damage process anyway, for the sake of simplicity we chose not to comply with ISO 21254:2011. However, the detailed description of the measurement procedure and the set-up allows the reproduction of the obtained results.

## Laser source working at MHz repetition rate

In order to explore the ultrafast damage behavior of multilayer thin-films at MHz repetition rate and high average power, we used a mode-locked Yb:YAG thin-disk oscillator operating

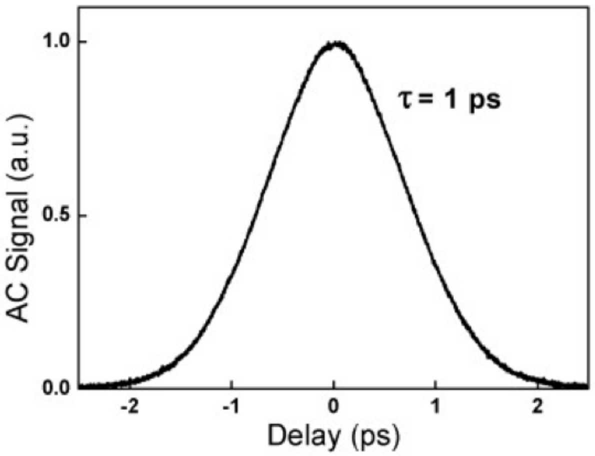

**Figure 7.4:** Autocorrelation trace of a pulse generated by 11.5 MHz mode-locked Yb:YAG thin-disk oscillator. (Reprinted from [49])

at wavelength of 1030 nm and repetition rate of 11.5 MHz. It delivered pulses with energy of 5 µJ and pulse duration of about 1 ps (Fig. 7.4). The resulting maximal average power was equal to 56 W. The laser system is described in more detail in Refs. [49, 129].

## Laser source at kHz repetition rate

The high average power at MHz repetition rate posed the question what role the thermal effects play in the mechanisms of optical damage in this regime. To investigate this, it was necessary to carry out measurements at a lower repetition rate, while keeping the other laser parameters, such as pulse duration and wavelength, similar. One way to achieve this would be to use a pulse picker to select a single pulse out of hundreds or thousands of pulses. However, such device was not available for our MHz laser system. Instead, the set-up was moved to a different laboratory, where a 5 kHz laser system operating at 1030 nm was used as source. It delivered multiple mJ, and only a small fraction of the available power was sufficient to perform the damage threshold measurements. The temporal shape and phase of the pulses were measured using a frequency-resolved optical gating (FROG) technique [130], and are given in Fig. 7.5. The flat phase over the intensity distribution shows Fourier-limited pulse duration of 1.4 ps.

The damage threshold measurements at kHz rate were performed on the same samples measured at 11.5 MHz repetition rate. The different sample sets are described in Section 7.1.

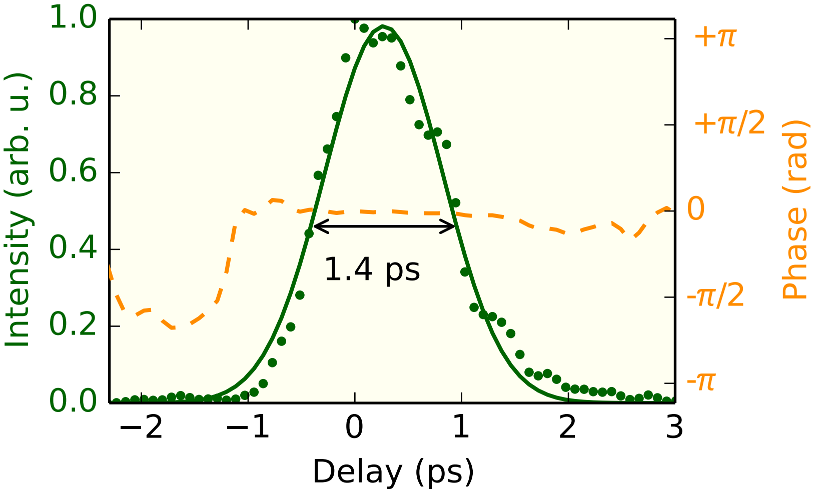

**Figure 7.5:** Temporal intensity profile (green color) and temporal phase (orange dashed curve) of the pulses generated by the kHz laser system measured using a FROG technique [130]. The green dots represent measurement data, and the green curve is a Gaussian fit.

## 7.3 Results and discussion

It has been shown previously that for pulse durations $\tau$ below ten picoseconds the laser-induced damage in dielectrics departs from being thermally-dominated and is instead initiated by a combination of multiphoton, tunneling and avalanche ionisation mechanisms [62]. Therefore here we refer to pulses shorter than 10 ps as ultrashort pulses.

In the ultrashort pulse regime, the damage threshold was found to scale linearly with the band gap of the material [68]. On the other hand, for materials with negligible absorption the real part of the dielectric function, i.e. the refractive index, is inversely proportional to the band gap [131]. Therefore, one can expect that the damage threshold of a QWOT stack is constrained by the breakdown threshold of its high-index material.

Figure 7.6(a) displays the damage threshold fluence of QWOT stacks employing different high-index materials versus the band gap of the respective material. The error bars represent experimental error of 10 % for the obtained damage threshold values. The band gaps of $Ta_2O_5$, $HfO_2$, and $Al_2O_3$ were taken from [72], whereas the band gap of $TiO_2$ was found in [132]. Evidently, even though the breakdown threshold of a quarter-wave stack scales to some extent with the band gap of its high-index material, the dependence is nonlinear. Note, however, that these fluence values were calculated at the front surface of the sample, without taking into account the electric field distribution inside the QWOT stack (Fig. 7.1(c)). If we take that into consideration, we will obtain threshold fluence values, which are characteristic for the layers themselves. We call this “internal” threshold fluence

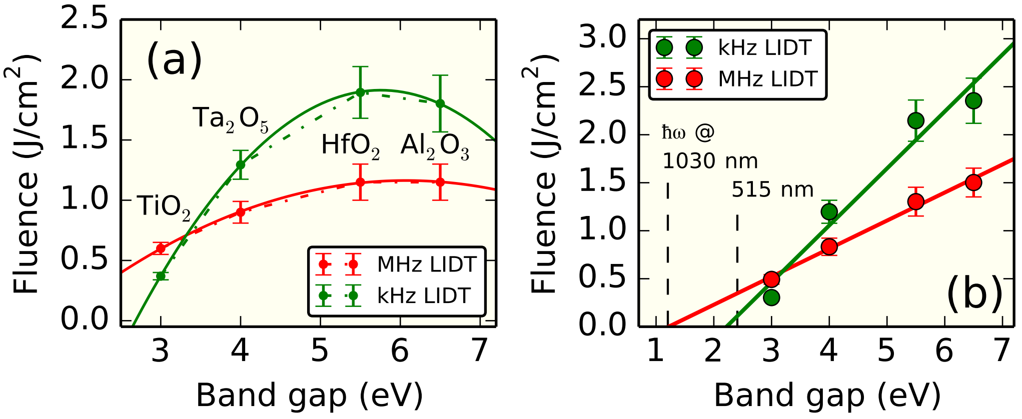

**Figure 7.6:** Damage fluences of different QWOT stacks versus band gap of the respective high-index materials. The measured damage fluences of the samples do not scale linearly with the band gap (a). However, if the electric field distribution inside of the QWOT stacks is taken into account (b), the resulting "internal" damage fluences follow a linear dependence on the band gap. The green color relates to measurements made at kHz rate, whereas the red color relates to measurements at MHz rate; all other measurement parameters were kept similar. The dashed black lines mark the photon energies at 1030 nm and 515 nm, as denoted.

for layer $X$:

$$F_{int}^{X} = \left| \frac{E_{max}^{X}}{E_{inc}} \right|^2 F_{ext}. \tag{7.3}$$

Here $F_{ext}$ is the measured threshold fluence on the front surface of the sample, $E_{inc}$ is the magnitude of the incident electric field and $E_{max}^{X}$ is the magnitude of the maximal electric field inside layer $X$.

In the case of QWOT stacks where the peaks of electric field are positioned on the boundaries between layers (Fig. 7.1(c)), the limiting factor is the internal damage threshold of high-index layers $F_{int}^{H}$, because of their narrower band gap compared to low-index layers. In addition, it can be shown by writing the characterization matrix for a QWOT stack that, at normal incidence, the height of the peak on the first boundary between $H$ and $L$ layers is inversely proportional to the square of the refractive index of the $H$ material. After we make a correction in accordance with Eq. (7.3) and with respect to the high-index layers, plotting the internal threshold fluence versus the band gap of the high-index material reveals a clear linear dependence (Fig. 7.6(b)). This is despite the fact that the $Al_2O_3$ and the $Ta_2O_5$ samples had absorption of 40 ppm, while the absorption of $TiO_2$ was 160 ppm and that of $HfO_2$ was 100 ppm (Fig. 7.2), that is there was up to a factor of four difference in absorption of the samples. Similarly, there was difference in total losses of up to a factor of two.

A couple of observations can be made here. First, it is evident that although the damage threshold does depend on the band gap of the material (Fig. 7.6(b)), there is a certain point beyond which the damage threshold of the whole QWOT stack (Fig. 7.6(a)) cannot be increased any more merely by choosing a high-index material with a broader band gap. Second, even though the different samples absorbed a different amount of the incident light, in some cases by a factor of four (Fig. 7.2), a linear scaling of damage threshold with respect to the band gap of the high-index material could be observed. This is a strong indication that even at MHz repetition rates and at large average power (some tens of watts), thermal effects do not constitute an important part of the damage mechanism in the ultrashort pulse regime ($\tau < 10$ ps).

Ideally, we would like to compare the damage threshold values obtained at 11.5 MHz repetition rate with ones retrieved by using a laser beam with a kHz repetition rate and otherwise similar parameters to ours (i.e., wavelength, pulse duration, and focal spot size).

Evidently, the band gap dependence of the measured (or "external") damage threshold at kHz rates follows a similar trend as in the MHz regime (Fig. 7.6(a)), but the threshold fluences of most samples are higher. Naturally, the internal damage threshold values of $Ta_2O_5$, $HfO_2$, and $Al_2O_3$ measured at kHz rate are also higher than at MHz rate (Fig. 7.6(b)). This is not the case for the sample made with $TiO_2$, which surprisingly shows lower damage threshold at kHz rate than at MHz rate, even though near the error bar. Despite this fact, together with the other kHz rate measurements, it forms a linear dependence, which is notably steeper than the linear dependence formed by the MHz rate measurements. Moreover, it crosses the abscissa at a different point. Understanding the meaning of this result requires further experimental and theoretical investigation.

An interesting fact to point out is that the linear dependence obtained for 11.5 MHz crosses the abscissa at 1.2 eV, which is close to the photon energy at 1030 nm. On the other hand, the photon energy at 515 nm is 2.4 eV, which is within the error bar of the point where the linear band-gap dependence obtained at 5 kHz crosses the abscissa (2.22 eV). Further investigation is required to determine whether these observations have any physical meaning.

The comparison of the damage threshold values of QWOT stacks with the corresponding threshold values of the NBP filters is given in Fig. 7.7. As explained in Section 7.1, there is a field enhancement inside of the cavity high-index layer of the NBP filter. It is illustrated in Fig. 7.7(a) that the MHz LIDT of such coating is lower than that of a QWOT stack with the same high-index material. This provides additional evidence that the distribution of electric field inside the multilayer coating plays an important role in determining its optical resistance.

In contrast to the MHz regime, the damage threshold values of the NBP filters at kHz rate are similar to the respective damage fluences of QWOT stacks (Fig. 7.7(b)). In fact, within the experimental error they are identical. At first glance this finding implies either that the NBP filters have lost their field enhancement properties, which are inherent to their structure; or that the damage threshold is not influenced significantly by the electrical

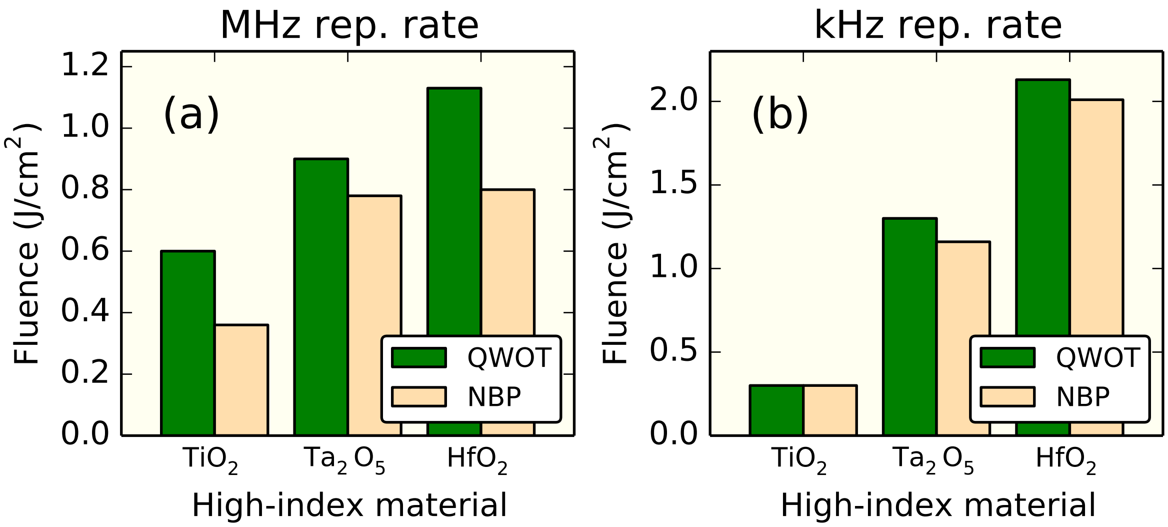

**Figure 7.7:** Damage threshold values of QWOT stacks and NBP filters made of different high-index materials measured: (a) at MHz rate and (b) at kHz rate.

field distribution in this regime. The latter contradicts a number of studies [128, 133, 134], as well as the expectations based on our results at MHz rate (Fig. 7.7(a)). Since the resonance spectral range of the NBP filters is less than a couple of nanometers wide, it is easily possible that the kHz measurements had been performed out of the resonance of the NBPs and hence without enhancement. In any case, further investigations are required to confirm or discard any of these two hypotheses.

It should be noted that due to high sensitivity to deposition errors of the NBP design, the actual distribution of electric field inside the produced coating may deviate substantially from the theoretical one. Thus, no efforts were made to estimate the internal damage fluence of these coatings in analogy to Fig. 7.6(b) and according to Eq. (7.3). Nevertheless, Fig. 7.7(a) provides evidence that the damage threshold of dielectric stacks at pulse durations of 1 ps is dependent on the electric field distribution even at high average power. We explored that dependency to find out whether it can be exploited to improve the damage threshold of our highly reflective coatings and to what extent.

Since in the ultrashort pulse regime the damage behavior of thin-films is mainly dictated by intrinsic material properties [68], the damage threshold itself can also be regarded as an intrinsic property of the thin-film material at a particular combination of wavelength and pulse duration. That is, an assumption can be made, that the threshold fluence of the high-index material $F_{int}^{H}$ is a characteristic property of that material and is not dependent on defects and impurities. Of course, the same also holds for the threshold fluence of the low-index material $F_{int}^{L}$. From that and from Eq. (7.3) it follows that the damage threshold of the whole thin-film stack $F_{ext}$ is governed by

$$F_{ext} = \min\left\{ \left|\frac{E_{inc}}{E^H_{max}}\right|^2 F^H_{int}, \quad \left|\frac{E_{inc}}{E^L_{max}}\right|^2 F^L_{int} \right\}, \tag{7.4}$$

where $E^L_{max}$ is the magnitude of maximum electric field in the low-index material. This expression implies also that if the electric field inside the high-index material is low enough, the electric field inside the low-index material becomes the limiting factor. One can see from Eq. (7.4) that the damage fluence of the assembly $F_{ext}$ has maximum when

$$\left|\frac{E^H_{max}}{E^L_{max}}\right|^2 = \frac{F^H_{int}}{F^L_{int}}. \tag{7.5}$$

To verify that experimentally, we prepared the so-called EFI coatings. A typical EFI design is given in Fig. 7.1(b) and the corresponding field distribution is shown in Fig. 7.1(d). Samples with such designs were manufactured using $TiO_2$ and $Ta_2O_5$ as high-index materials. Their damage thresholds at MHz rate are compared with QWOT stacks of the respective materials (Fig. 7.8(a)). In both cases an improvement of about 30 % was obtained.

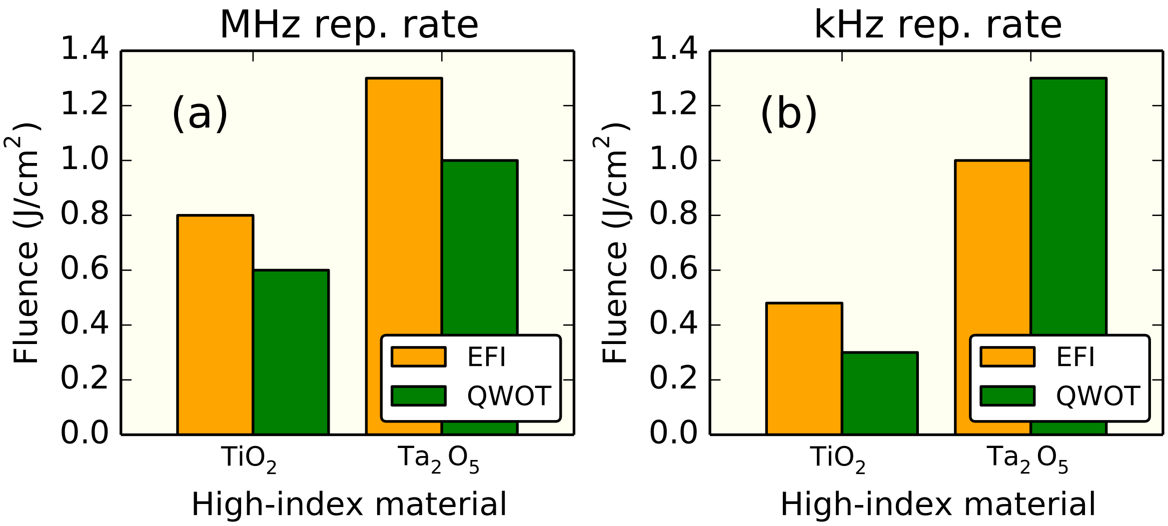

**Figure 7.8:** Damage threshold values of EFI and QWOT stacks measured: (a) at MHz repetition rate and (b) at kHz repetition rate.

The damage fluences of EFI structures, like the one shown in Fig. 7.1, made of $TiO_2$ and $Ta_2O_5$ were measured also at 5 kHz. In Fig. 7.8(b) the results are compared to the respective damage threshold of QWOT stacks made of the same high-index materials. The $TiO_2$ samples behaved in a similar way as in the MHz case: the EFI design showed about 30 % higher damage threshold than its QWOT counterpart. However, the situation was reversed in the case of $Ta_2O_5$: the QWOT stack demonstrated 30 % higher damage threshold than the EFI. Most likely, this inconsistency is related to the different slope of the band gap dependence measured at kHz rate (Fig. 7.6(b)). For instance, due to the aforementioned slope difference, the ratio between the internal damage fluences $F^{H}_{int}$ and $F^{L}_{int}$ is different for kHz rate than for MHz rate, resulting in different optimal condition (Eq. (7.5)). Another suspect for the disagreement in Fig. 7.8 is the fundamental cause standing behind the slope difference itself, a cause, which in turn is not understood at present. At any rate, to identify the reason for this discrepancy more measurements need to be performed both in the kHz and the MHz regimes.

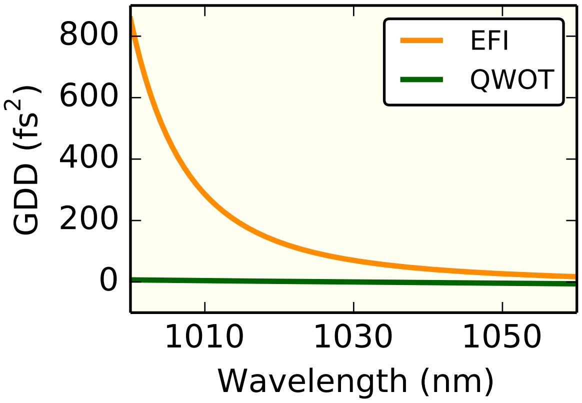

**Figure 7.9:** Theoretical GDD of a QWOT stack and an EFI design around the central wavelength.

Although the EFI coatings generally offer high LIDT, their dispersion properties of the EFI are unfavorable to ultrashort pulses, as such coatings would introduce a relatively large amount of GDD, as well as dispersion of higher orders (Fig. 7.9). These will lead to pulse broadening and the formation of sideband pulses, respectively.

Another interesting example is the damage threshold of the "low-index layer on top (LOT)" design. A LOT design is just like a QWOT stack, but as its name suggests, on top of the stack there is an additional low-index layer, which has thickness of a half QWOT, i.e.:

$$(HL)^m H(L/2). \tag{7.6}$$

Figure 7.10 compares the damage threshold of a LOT to a QWOT stack, both made with $TiO_2$ as high-index material. It demonstrates a factor of two improvement with respect to the simple QWOT stack. This improvement cannot be attributed to different electric field distribution, because the $L/2$ layer on top of the dielectric stack modifies the distribution of electric field only slightly, and does not reduce it by a factor of two in the first $H$ layer.

The increased optical resistance of the mirror due to the overcoating low-index layer can be explained by the fact that the high-index layer is not at the surface of the thin-

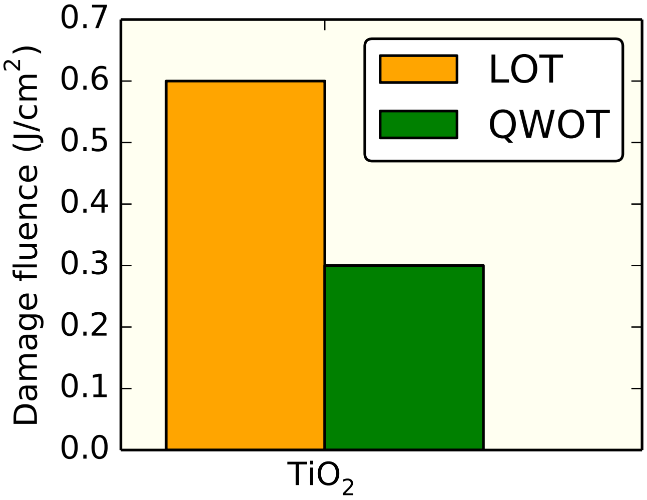

**Figure 7.10:** Comparison of LOT and QWOT designs made with $TiO_2$ as high-index material.

film assembly, but instead it is inside the layer structure. It is well known that optical breakdown occurs at a lower threshold at the surfaces than in the interior [84]. Since the low-index material has broader band gap and thus higher LIDT, the overcoating $L/2$ layer can serve to increase the damage threshold of the mirror.

## 7.4 Conclusion

We have investigated the damage threshold of three different types of coatings made with either $TiO_2$, $Ta_2O_5$, $HfO_2$, or $Al_2O_3$ as high-index material, whereas $SiO_2$ was used as low-index material. The measurements were carried out using a mode-locked Yb:YAG thin-disk oscillator generating at a central wavelength of 1030 nm pulses with duration of 1 ps and energy of 5 µJ at a repetition rate of 11.5 MHz, resulting in 56 W average power. The results have been compared with measurements performed at kHz repetition rate, using an Yb:YAG thin-disk regenerative amplifier. It delivered multi µJ, 1.4 ps pulses at wavelength of 1030 nm. In both regimes, the beam has been focused down to a spot 25 µm in diameter.

We have shown that the damage fluence of QWOT stacks scales linearly with the band gap of the used high-index material, if the damage threshold is normalized with respect to electric field. This suggests that thermal effects do not play a significant part in the ultrashort pulse damage mechanism even with high-average power at MHz repetition rate. This conclusion is complemented by the fact that the linear band gap dependence has not been affected by the different absorption of the samples. Still, the LIDT values obtained at MHz rate scaled differently with band gap with respect to kHz measurements.

Further proof of the importance of the electric field distribution to the ultrafast optical breakdown at MHz is given by NBP filters, where the electric field inside a high-index layer was enhanced. The enhanced electric field effectively reduced the damage threshold of these structures. This dependence on electric field was exploited to produce highly reflective coatings with higher optical resistance by suppressing the electric field inside high-index materials and shifting its maxima to the low index materials. Additionally, a condition for optimal field suppression has been also given. In contrast to the MHz regime, the measurements at kHz rate have shown that the EFI sample coated with $Ta_2O_5$ as high-index material had lower LIDT than a QWOT stack made of the same pair of materials. This might be connected to the different band gap dependence in this regime.

# Chapter 8

# Conclusion and outlook

## Conclusion

Two of the major challenges towards generation of ultrashort pulses with high intensity are: (i) accurate dispersion control over broad spectral bandwidths; (ii) laser-induced damage of the optics. While the first problem has often been tackled using dispersive mirrors, this thesis has attempted to address the second problem by investigating the femtosecond laser-induced damage of dispersive mirrors, as well as that of other multilayer coatings. In addition, a new method for dispersion characterization of multilayer mirrors has been developed.

The newly developed technique for dispersion measurements—RSI—is based on Fabry-Pérot and Gires-Tournois interferometry and follows a concept suggested originally by Osvay *et al.* [101]. The necessity to determine the spacer thickness and the relatively low spectral as well as GD resolution are major drawbacks of the method described in Ref. [101]. In contrast to their stationary interferometer, we have processed simultaneously the transmission or reflection spectra for many different inter-mirror spacer widths. This has allowed us to exclude the spacer thickness from data evaluation and to obtain resolution superseding not only the method described in Ref. [101], but also the resolution of WLI. RSI is expected to facilitate the development of dispersive mirror technology.

In addition to dispersion, we have also systematically studied the femtosecond laser-induced damage of dispersive mirrors. The LIDT measurements have been performed using 30 fs at 790 nm central wavelength and following at repetition rate of 500 Hz. The samples have been of three main types: (i) a variety of single-layer metal, as well as dielectric coatings; (ii) QWOT stacks of different high-index materials; (iii) dispersive mirrors of highly different designs: each design has been tailored to suit a different application.

On one hand, the LIDT of single-layer dielectric coatings has been found to scale with the band gap of the coated material. On the other hand, although being very different in terms of design, all dispersive mirrors and QWOT stacks made of the same high-index material have shown similar LIDT to a single-layer coating of that material. Thus, the femtosecond LIDT can be increased by choosing materials with wider gap. However, materials with wider gap have lower refractive indices and choosing such materials results in a lower refractive index contrast ratio. This in turn limits the performance of the mirror in terms of bandwidth, reflectance and dispersion. An optimal balance between LIDT and performance of a multilayer thin-film can be obtained by tuning the band gap of the high-index material by mixing it with the low-index material.

Another intriguing finding in the femtosecond regime has been the fact that metal mirrors had similar LIDT to dielectric mirrors.

In view of state-of-the-art ultrafast laser systems, which are able to generate multi µJ pulses at high repetition rates, we have also studied the ultrafast optical breakdown of multilayer thin-films at MHz repetition rate and high average power. The LIDT of three different types of coatings has been measured. All samples have been coated with either $TiO_2$, $Ta_2O_5$, $HfO_2$, or $Al_2O_3$ as high-index material and with $SiO_2$ as low-index material. The LIDT results obtained at MHz repetition rate have been compared with measurements carried out using a kHz laser system with otherwise similar parameters.

We have demonstrated that if the LIDT of QWOT stacks is normalized with respect to the maximal electric field distribution inside the layer stack, it scales linearly with the band gap of the high-index material. This indicates that thermal effects do not play a decisive role in the ultrafast optical breakdown even at high average power and MHz repetition rate. This conclusion is emphasized by the fact that the linear absorption of the studied QWOT stacks varied substantially without affecting the linear band gap dependence. However, the measurements performed at kHz rate showed a band gap dependence that was steeper and crossed the abscissa at a higher value than its MHz counterpart.

An additional indication that the electric field distribution is of significance to the ultrafast MHz laser-induced damage has been given by NBP filters. In these structures the electric field inside a high-index layer was enhanced and the LIDT of NBP filters was lower than QWOT stacks. The LIDT dependence on electric field distribution has been utilized to obtain high-reflective coatings with superior optical resistance. This has been achieved by modifying the layer stack of certain samples (EFI) in such way that the electric field inside the high-index material has been reduced and its peaks have been shifted to the wider gap low-index material. However, while in the MHz regime all EFI samples have shown 30 % higher LIDT with respect to QWOT stacks, this has not been the case in the kHz regime. The EFI sample made using $Ta_2O_5$ as high-index material has demonstrated lower LIDT than its QWOT counterpart. This might be related to the different slope of the band gap dependence or to the phenomenon which underlies it.

# Outlook

The comparison of optical breakdown thresholds obtained at kHz and MHz repetition rates has left open some intriguing questions. Perhaps the most interesting among them are posed by the finding of different band gap dependencies measured at kHz and MHz repetition rate: why does the LIDT at MHz rate scale with the band gap differently than at kHz rate? Why at kHz rate the band gap dependence is steeper than at MHz rate, and not vice versa? And, is it a mere coincidence, or is there a physical meaning behind the fact that the MHz gap dependence crosses the abscissa at about the photon energy of the fundamental frequency, and the kHz dependence—at about the photon energy of the second harmonic? What does all of it mean physically?

Although we ask these questions regarding the laser damage mechanism in some particular regimes, the answers might be relevant to the physics of laser-matter interactions. These answers can be sought by performing additional measurements outside the investigated band gap regions and by building a theoretical model around the gathered data. In addition, it might be beneficial to apply the tools of attosecond transient absorption spectroscopy to identify and study the phenomena responsible for this behavior of MHz and kHz optical breakdown.

Another question left open by the comparison of LIDT at different repetition rates concerns the reason for the different behavior of EFI samples in these two regimes. The answer might be related to the different band gap dependencies discussed above, but certainly more measurement data is necessary in order to find out.

One area in the femtosecond optical breakdown of dispersive mirrors has remained largely unexplored. That is the dependence of LIDT on the time-domain electric field distribution inside the multilayer stack. Investigation in this direction will reveal if the LIDT of dispersive mirrors can be increased by modifying the multilayer structure, while using the same constituent materials.

The RSI technique for dispersion measurements has demonstrated promising initial results superseding the resolution of the conventional method (WLI). However, its precision is yet to be properly estimated, and due to the complex algorithms involved in the data evaluation process, this appears to be a challenging task.

# Appendix A

# Fluence of a Gaussian Pulse

Here we derive the equations for peak intensity and peak fluence as functions of average power.

## A.1 Peak intensity

Let us assume we have a pulse with a profile, which is Gaussian both temporally and spacially in transverse direction. Then the equation describing such intensity distribution would be:

$$I(r,t) = \hat{I}\, e^{-\frac{2r^2}{w^2}}\, e^{-2\ln 2\frac{t^2}{\tau^2}}, \tag{A.1}$$

where $\tau$ is the pulse duration and $w$ is the beam radius, defined as the transversal distance from the axis at which the intensity is $1/e^2$ times the peak intensity $\hat{I}$.

The power as a funcion of time $P(t)$ is nothing else but the beam intensity distribution integrated over a plane $D$ perpendicular to the direction of beam propagation:

$$P(t) = \iint\limits_{D} I(r,t)\,\mathrm{d}A, \tag{A.2}$$

which can be represented in cylindrical coordinates as:

$$P(t) = \int\limits_{0}^{2\pi}\int\limits_{0}^{\infty} I(r,t)\, r\,\mathrm{d}r\,\mathrm{d}\theta. \tag{A.3}$$

If we substitute (A.1) in (A.3) we will obtain the power as function of time:

$$P(t) = \hat{I}\,\frac{\pi w^2}{2} e^{-2\ln 2t^2/\tau^2}. \tag{A.4}$$

Since a powermeter measures the average power $\bar{P}$ over some interval of time $\Delta t$, we would like to express the peak intensity $\hat{I}$ with $\bar{P}$. Thus we average (A.4) over time

$$\bar{P} = \frac{1}{\Delta t} \int\limits_{t}^{t+\Delta t} P(t)\,\mathrm{d}t. \tag{A.5}$$

By solving (A.5) we obtain the average power:

$$\bar{P} = \hat{I}\, f_{\mathrm{rep}}\, w^2 \tau \left(\frac{\pi}{2}\right)^{\frac{3}{2}}, \tag{A.6}$$

where $f_{\mathrm{rep}}$ is the repetition rate of the laser.

Finally, when we express the peak intensity using the average power, we get:

$$\hat{I} = \left(\frac{\pi}{2}\right)^{-\frac{3}{2}} \frac{\bar{P}}{f_{\mathrm{rep}}\, w^2\, \tau}. \tag{A.7}$$

## A.2 Peak fluence

In the previous section we integrated beam intensity over a transverse plane and we obtained the optical power of the beam as a function of time. Now if we integrate (A.1) over time instead, we will get

$$J(r) = \int\limits_{-\infty}^{\infty} I(r,t)\,\mathrm{d}t, \tag{A.8}$$

where $J(r)$ is the fluence, i.e. the energy flow, at radial distance $r$ from the propagation axis. By solving the integral we obtain

$$J(r) = \sqrt{\frac{\pi}{2}}\, \hat{I}\, \tau\, e^{-2r^2/w^2}. \tag{A.9}$$

The peak of a Gaussian beam lies on the propagation axis, i.e. where $r = 0$. Thus the peak fluence $\hat{J} = J(r = 0)$ or

$$\hat{J} = \sqrt{\frac{\pi}{2}}\, \hat{I}\, \tau. \tag{A.10}$$

Substituting the peak intensity from (A.7) in (A.10) we obtain the final expression to calculate the peak fluence from the measured average power:

$$\hat{J} = \frac{2\,\bar{P}}{\pi w^2\, f_{\mathrm{rep}}}. \tag{A.11}$$

This result is essentially the pulse energy $E_p$ divided by the area $A_\sigma = \pi w^2$ within which the intensity of the beam is larger than $\hat{I}/e^2$:

$$\hat{J} = 2\,\frac{E_p}{A_\sigma}. \tag{A.12}$$

The correction factor of two in (A.12) is due to the Gaussian profile of the pulse in transversal plane [1].

---

[1] For a pulse with a rectangular transverse profile the correction factor is unity.

# Appendix B

# Data Archiving

The experimental raw data, evaluation files, and original figures can be found on the Data Archive Server of the Laboratory for Attosecond Physics at the Max Planck Institute of Quantum Optics:

`/afs/ipp/mpq/lap/publication_archive/Theses/2014/Angelov Ivan/`

The list below contains paths to all relevant folders given with respect to the archive folder of the thesis. In each folder which contains data used in a figure, there is a `README.txt` file. It contains a thorough description of the contents of that folder along with the necessary steps to generate the respective figure.

**Figure 3.7**

- Data (evaluated by Michael Trubetskov with his program for RSI evaluation):
  `Fig3.7/Fig3.7{a,b,c,d}.txt`
- Python program plotting the figure:
  `Fig3.7/BB.py`
- Plot:
  `Fig3.7/RSI-BB.pdf`

**Figure 3.8**

- Data (evaluated by Michael Trubetskov with his program for RSI evaluation):
  `Fig3.8/Fig3.8{a,b,c,d}.txt`
- Python program plotting the figure:
  `Fig3.8/UBB-mirror.py`
- Plot:
  `Fig3.8/RSI-UBB.pdf`

**Figure 3.9**

- Data (evaluated by Michael Trubetskov with his program for RSI evaluation):
  `Fig3.9/Fig3.9{a,b,c,d}.txt`

- Python program plotting the figure:
  `Fig3.9/HD.py`
- Plot:
  `Fig3.9/RSI-HD.pdf`

**Figure 6.3 through Figure 6.6**

- Data:
  `Fig6.3-6.6/raw_data/`
- Processing program:
  `Fig6.3-6.6/DTeval.py`
- Processed and summarized data:
  `Fig6.3-6.6/fs_LIDT.opj`
  Exported in plain text to be plotted:
  `Fig6.3-6.6/SingleLayers.csv`
  `Fig6.3-6.6/Niobia.csv`
  `Fig6.3-6.6/Tantala.csv`
  `Fig6.3-6.6/HDTs.csv`
  `Fig6.3-6.6/Metals.csv`
- Python programs plotting the data:
  `Fig6.3-6.6/SingleLayers.py`
  `Fig6.3-6.6/Nb-Ta.py`
  `Fig6.3-6.6/HDTs.py`
  `Fig6.3-6.6/Metals.py`
- Plots:
  `Fig6.3-6.6/SLs.pdf`
  `Fig6.3-6.6/Nb-Ta.pdf`
  `Fig6.3-6.6/HDTs.pdf`
  `Fig6.3-6.6/Metals.pdf`

**Figure 7.1**

- Theoretical data generated using OptiLayer software:
  `Fig7.1/index_profile-QWOT.csv`
  `Fig7.1/index_profile-EFI.csv`
  `Fig7.1/HR-Ta2O5-35L.csv`
  `Fig7.1/EFI-Ta2O5-35L.csv`

- Python program plotting the figure:
  `Fig7.1/designs-efield.py`
- Plot:
  `Fig7.1/designs-efield.pdf`

**Figure 7.2**

- Data:
  `Fig7.2/raw_data/`
- Python program plotting the figure:
  `Fig7.2/losses_barchart.py`
- Plot:
  `Fig7.2/losses.pdf`

### Figure 7.5

- Data (FROG measurement):
  `final23mm 22102013.bin.Ek.dat`
  `Fig7.5/raw_data/` (contains all files from the FROG measurement)
- Python program plotting the figure:
  `Fig7.5/frog-fit.py`
- Plot:
  `Fig7.5/frog-5kHz-fit.pdf`

### Figure 7.6 through Figure 7.10

- Data:
  `Fig7.6-7.10/raw_data/`
- Processing program:
  `Fig7.6-7.10/DTeval.py`
- Processed and summarized data:
  `Fig7.6-7.10/MHz-LIDT.opj`
  `Fig7.6-7.10/kHz-LIDT.opj`
- Python programs plotting the data:
  `Fig7.6-7.10/DTvsBandgap.py`
  `Fig7.6-7.10/DT_NBP.py`
  `Fig7.6-7.10/DT_EFI.py`
  `Fig7.6-7.10/EFI-GDD.py`
  `Fig7.6-7.10/DT_LOT.py`
- Plots:
  `Fig7.6-7.10/DTvsBandgap-linear.pdf`
  `Fig7.6-7.10/DT-NBP.pdf`
  `Fig7.6-7.10/DT-EFI.pdf`
  `Fig7.6-7.10/gdd-efi.pdf`
  `Fig7.6-7.10/DT-LOT.pdf`

# Bibliography

[1] J. D. B. Stillman, E. Muybridge. *The horse in motion as shown by instantaneous photography, with a study on animal mechanics founded on anatomy and the revelations of the camera, in which is demonstrated the theory of quadrupedal locomotion*. In collab. with University of California Libraries (J. R. Osgood and Co., Boston, 1882). 322 pp.

[2] P. Krehl, S. Engemann. *August Toepler — The first who visualized shock waves*. Shock Waves **5**, 1–18 (1995).

[3] A. Schawlow, C. Townes. *Infrared and Optical Masers*. Physical Review **112**, 1940–1949 (1958).

[4] T. H. Maiman. *Stimulated Optical Radiation in Ruby*. Nature **187**, 493–494 (1960).

[5] N. G. Basov, O. N. Krokhin, Y. M. Popov. *Generation, amplification, and detection of infrared and optical radiation by quantum-mechanical systems*. Soviet Physics Uspekhi **3**, 702–728 (1961).

[6] F. Träger, ed. *Springer Handbook of Lasers and Optics* (Springer, New York, 2007). 1332 pp. isbn: 0387955798.

[7] E. P. Ippen, C. V. Shank, A. Dienes. *Passive mode locking of the cw dye laser*. Applied Physics Letters **21**, 348–350 (1972).

[8] R. L. Fork, B. I. Greene, C. V. Shank. *Generation of optical pulses shorter than 0.1 psec by colliding pulse mode locking*. Applied Physics Letters **38**, 671–672 (1981).

[9] J.-C. Diels, W. Rudolph. *Ultrashort laser pulse phenomena: fundamentals, techniques, and applications on a femtosecond time scale*. 2nd ed. Optics and photonics (Elsevier / Academic Press, Amsterdam ; Boston, 2006). 652 pp. isbn: 0122154932.

[10] T. Brabec, F. Krausz. *Intense few-cycle laser fields: Frontiers of nonlinear optics*. Reviews of Modern Physics **72**, 545–591 (2000).

[11] U. Keller. *Recent developments in compact ultrafast lasers*. Nature **424**, 831–838 (2003).

[12] F. Krausz, M. Ivanov. *Attosecond physics*. Reviews of Modern Physics **81**, 163–234 (2009).

[13] A. H. Zewail. *Femtochemistry: Atomic-Scale Dynamics of the Chemical Bond*. The Journal of Physical Chemistry A **104**, 5660–5694 (2000).

[14] M. Hentschel, R. Kienberger, C. Spielmann, G. A. Reider, N. Milosevic, T. Brabec, P. Corkum, U. Heinzmann, M. Drescher, F. Krausz. *Attosecond metrology*. Nature **414**, 509–513 (2001).

[15] E. Goulielmakis, M. Schultze, M. Hofstetter, V. S. Yakovlev, J. Gagnon, M. Uiberacker, A. L. Aquila, E. M. Gullikson, D. T. Attwood, R. Kienberger, F. Krausz, U. Kleineberg. *Single-Cycle Nonlinear Optics*. Science **320**, 1614–1617 (2008).

[16] E. Goulielmakis, Z.-H. Loh, A. Wirth, R. Santra, N. Rohringer, V. S. Yakovlev, S. Zherebtsov, T. Pfeifer, A. M. Azzeer, M. F. Kling, S. R. Leone, F. Krausz. *Real-time observation of valence electron motion*. Nature **466**, 739–743 (2010).

[17] A. Wirth, M. T. Hassan, I. Grguraš, J. Gagnon, A. Moulet, T. T. Luu, S. Pabst, R. Santra, Z. A. Alahmed, A. M. Azzeer. *Synthesized light transients*. Science **334**, 195–200 (2011).

[18] A. Schiffrin, T. Paasch-Colberg, N. Karpowicz, V. Apalkov, D. Gerster, S. Mühlbrandt, M. Korbman, J. Reichert, M. Schultze, S. Holzner, J. V. Barth, R. Kienberger, R. Ernstorfer, V. S. Yakovlev, M. I. Stockman, F. Krausz. *Optical-field-induced current in dielectrics*. Nature **493**, 70–74 (2013).

[19] M. Schultze, E. M. Bothschafter, A. Sommer, S. Holzner, W. Schweinberger, M. Fiess, M. Hofstetter, R. Kienberger, V. Apalkov, V. S. Yakovlev, M. I. Stockman, F. Krausz. *Controlling dielectrics with the electric field of light*. Nature **493**, 75–78 (2013).

[20] F. Krausz, M. I. Stockman. *Attosecond metrology: from electron capture to future signal processing*. Nature Photonics **8**, 205–213 (2014).

[21] S. V. Bulanov, V. S. Khoroshkov. *Feasibility of using laser ion accelerators in proton therapy*. Plasma Physics Reports **28**, 453–456 (2002).

[22] C.-M. Ma, I. Veltchev, E. Fourkal, J. S. Li, W. Luo, J. Fan, T. Lin, A. Pollack. *Development of a laser-driven proton accelerator for cancer therapy*. Laser Physics **16**, 639–646 (2006).

[23] T. Tajima, D. Habs, X. Yan. *Laser Acceleration of Ions for Radiation Therapy*. Reviews of Accelerator Science and Technology **02**, 201–228 (2009).

[24] H. Daido, M. Nishiuchi, A. S. Pirozhkov. *Review of laser-driven ion sources and their applications*. Reports on Progress in Physics **75**, 056401 (2012).

[25] R. A. Snavely, M. H. Key, S. P. Hatchett, T. E. Cowan, M. Roth, T. W. Phillips, M. A. Stoyer, E. A. Henry, T. C. Sangster, M. S. Singh, S. C. Wilks, A. MacKinnon, A. Offenberger, D. M. Pennington, K. Yasuike, A. B. Langdon, B. F. Lasinski, J. Johnson, M. D. Perry, E. M. Campbell. *Intense High-Energy Proton Beams from Petawatt-Laser Irradiation of Solids*. Physical Review Letters **85**, 2945–2948 (2000).

[26] S. D. Kraft, C. Richter, K. Zeil, M. Baumann, E. Beyreuther, S. Bock, M. Bussmann, T. E. Cowan, Y. Dammene, W. Enghardt, U. Helbig, L. Karsch, T. Kluge, L. Laschinsky, E. Lessmann, J. Metzkes, D. Naumburger, R. Sauerbrey, M. Schürer, M. Sobiella. *Dose-dependent biological damage of tumour cells by laser-accelerated proton beams*. New Journal of Physics **12**, 085003 (2010).

[27] J. Bin, K. Allinger, W. Assmann, G. Dollinger, G. A. Drexler, A. A. Friedl, D. Habs, P. Hilz, R. Hoerlein, N. Humble, S. Karsch, K. Khrennikov, D. Kiefer, F. Krausz, W. Ma, D. Michalski, M. Molls, S. Raith, S. Reinhardt, B. Röper. *A laser-driven nanosecond proton source for radiobiological studies*. Applied Physics Letters **101**, pages (2012).

[28] R. L. Fork, C. H. Brito Cruz, P. C. Becker, C. V. Shank. *Compression of optical pulses to six femtoseconds by using cubic phase compensation.* Optics Letters **12**, 483–485 (1987).

[29] E. Treacy. *Optical pulse compression with diffraction gratings.* IEEE Journal of Quantum Electronics **5**, 454–458 (1969).

[30] R. L. Fork, O. E. Martinez, J. P. Gordon. *Negative dispersion using pairs of prisms.* Optics Letters **9**, 150–152 (1984).

[31] J. Heppner, J. Kuhl. *Intracavity chirp compensation in a colliding pulse mode-locked laser using thin-film interferometers.* Applied Physics Letters **47**, 453–455 (1985).

[32] R. Szipöcs, K. Ferencz, C. Spielmann, F. Krausz. *Chirped multilayer coatings for broadband dispersion control in femtosecond lasers.* Optics Letters **19**, 201–203 (1994).

[33] R. Szipöcs, A. Köházi-Kis, S. Lakó, P. Apai, A. Kovács, G. DeBell, L. Mott, A. Louderback, A. Tikhonravov, M. Trubetskov. *Negative dispersion mirrors for dispersion control in femtosecond lasers: chirped dielectric mirrors and multi-cavity Gires–Tournois interferometers:* Applied Physics B **70**, S51–S57 (2000).

[34] B. Golubovic, R. Austin, M. Steiner-Shepard, M. Reed, S. Diddams, D. Jones, A. Van Engen. *Double Gires–Tournois interferometer negative-dispersion mirrors for use in tunable mode-locked lasers.* Optics Letters **25**, 275–277 (2000).

[35] S. Kane, J. Squier. *Grism-pair stretcher-compressor system for simultaneous second- and third-order dispersion compensation in chirped-pulse amplification.* Journal of the Optical Society of America B **14**, 661–665 (1997).

[36] V. Pervak, V. Fedorov, Y. A. Pervak, M. Trubetskov. *Empirical study of the group delay dispersion achievable with multilayer mirrors.* Optics Express **21**, 18311–18316 (2013).

[37] V. Pervak, C. Teisset, A. Sugita, S. Naumov, F. Krausz, A. Apolonski. *High-dispersive mirrors for femtosecond lasers.* Optics Express **16**, 10220–10233 (2008).

[38] V. Pervak, A. Tikhonravov, M. Trubetskov, S. Naumov, F. Krausz, A. Apolonski. *1.5-octave chirped mirror for pulse compression down to sub-3 fs.* Applied Physics B **87**, 5–12 (2006).

[39] V. Pervak, I. Ahmad, M. K. Trubetskov, A. V. Tikhonravov, F. Krausz. *Double-angle multilayer mirrors with smooth dispersion characteristics.* Optics Express **17**, 7943–7951 (2009).

[40] V. Pervak, O. Pronin, O. Razskazovskaya, J. Brons, I. B. Angelov, M. K. Trubetskov, A. V. Tikhonravov, F. Krausz. *High-dispersive mirrors for high power applications.* Optics Express **20**, 4503 (2012).

[41] T. Eidam, S. Hanf, E. Seise, T. V. Andersen, T. Gabler, C. Wirth, T. Schreiber, J. Limpert, A. Tünnermann. *Femtosecond fiber CPA system emitting 830 W average output power.* Optics Letters **35**, 94–96 (2010).

[42] P. Russbueldt, T. Mans, J. Weitenberg, H. D. Hoffmann, R. Poprawe. *Compact diode-pumped 1.1 kW Yb:YAG Innoslab femtosecond amplifier.* Optics Letters **35**, 4169–4171 (2010).

[43] M. Schulz, R. Riedel, A. Willner, T. Mans, C. Schnitzler, P. Russbueldt, J. Dolkemeyer, E. Seise, T. Gottschall, S. Hädrich, S. Duesterer, H. Schlarb, J. Feldhaus, J. Limpert, B. Faatz, A. Tünnermann, J. Rossbach, M. Drescher, F. Tavella. *Yb:YAG Innoslab amplifier: efficient high repetition rate subpicosecond pumping system for optical parametric chirped pulse amplification*. Optics Letters **36**, 2456–2458 (2011).

[44] C. J. Saraceno, F. Emaury, O. H. Heckl, C. R. E. Baer, M. Hoffmann, C. Schriber, M. Golling, T. Südmeyer, U. Keller. *275 W average output power from a femtosecond thin disk oscillator operated in a vacuum environment*. Optics Express **20**, 23535–23541 (2012).

[45] D. Bauer, I. Zawischa, D. H. Sutter, A. Killi, T. Dekorsy. *Mode-locked Yb:YAG thin-disk oscillator with 41 uJ pulse energy at 145 W average infrared power and high power frequency conversion*. Optics Express **20**, 9698–9704 (2012).

[46] O. Pronin, J. Brons, C. Grasse, V. Pervak, G. Boehm, M.-C. Amann, V. L. Kalashnikov, A. Apolonski, F. Krausz. *High-power 200 fs Kerr-lens mode-locked Yb:YAG thin-disk oscillator*. Optics Letters **36**, 4746–4748 (2011).

[47] T. Metzger, A. Schwarz, C. Y. Teisset, D. Sutter, A. Killi, R. Kienberger, F. Krausz. *High-repetition-rate picosecond pump laser based on a Yb:YAG disk amplifier for optical parametric amplification*. Optics Letters **34**, 2123–2125 (2009).

[48] S. Klingebiel, C. Wandt, C. Skrobol, I. Ahmad, S. A. Trushin, Z. Major, F. Krausz, S. Karsch. *High energy picosecond Yb: YAG CPA system at 10 Hz repetition rate for pumping optical parametric amplifiers*. Optics Express **19**, 5357–5363 (2011).

[49] H. Fattahi, C. Y. Teisset, O. Pronin, A. Sugita, R. Graf, V. Pervak, X. Gu, T. Metzger, Z. Major, F. Krausz, A. Apolonski. *Pump-seed synchronization for MHz repetition rate, high-power optical parametric chirped pulse amplification*. Optics Express **20**, 9833–9840 (2012).

[50] I. Pupeza, T. Eidam, J. Rauschenberger, B. Bernhardt, A. Ozawa, E. Fill, A. Apolonski, T. Udem, J. Limpert, Z. A. Alahmed. *Power scaling of a high-repetition-rate enhancement cavity*. Optics Letters **35**, 2052–2054 (2010).

[51] I. Pupeza, S. Holzberger, T. Eidam, H. Carstens, D. Esser, J. Weitenberg, P. Rußbüldt, J. Rauschenberger, J. Limpert, T. Udem, A. Tünnermann, T. W. Hänsch, A. Apolonski, F. Krausz, E. Fill. *Compact high-repetition-rate source of coherent 100 eV radiation*. Nature Photonics **7**, 608–612 (2013).

[52] H. Carstens, S. Holzberger, J. Kaster, J. Weitenberg, V. Pervak, A. Apolonski, E. Fill, F. Krausz, I. Pupeza. *Large-mode enhancement cavities*. Optics Express **21**, 11606 (2013).

[53] N. Bloembergen. *Laser-induced electric breakdown in solids*. IEEE Journal of Quantum Electronics **10**, 375–386 (1974).

[54] E. Yablonovitch, N. Bloembergen. *Avalanche Ionization and the Limiting Diameter of Filaments Induced by Light Pulses in Transparent Media*. Physical Review Letters **29**, 907–910 (1972).

[55] E. Bliss, D. Milam, R. Bradbury. *Dielectric mirror damage by laser radiation over a range of pulse durations and beam radii*. Applied Optics **12**, 677–689 (1973).

[56] N. Bloembergen. *Role of cracks, pores, and absorbing inclusions on laser induced damage threshold at surfaces of transparent dielectrics.* Applied Optics **12**, 661–664 (1973).

[57] M. R. Lange, J. K. McIver, A. H. Guenther. *Pulsed laser damage in thin film coatings: Fluorides and oxides.* Thin Solid Films **125**, 143–155 (1985).

[58] A. A. Manenkov, A. M. Prokhorov. *Laser-induced damage in solids.* Soviet Physics Uspekhi **29**, 104 (1986).

[59] J.-Y. Natoli, L. Gallais, H. Akhouayri, C. Amra. *Laser-induced Damage of Materials in Bulk, Thin-film, and Liquid forms.* Applied Optics **41**, 3156–3166 (2002).

[60] D. Du, X. Liu, G. Korn, J. Squier, G. Mourou. *Laser-induced breakdown by impact ionization in SiO2 with pulse widths from 7 ns to 150 fs.* Applied Physics Letters **64**, 3071–3073 (1994).

[61] B. C. Stuart, M. D. Feit, A. M. Rubenchik, B. W. Shore, M. D. Perry. *Laser-Induced Damage in Dielectrics with Nanosecond to Subpicosecond Pulses.* Physical Review Letters **74**, 2248–2251 (1995).

[62] B. C. Stuart, M. D. Feit, S. Herman, A. M. Rubenchik, B. W. Shore, M. D. Perry. *Nanosecond-to-femtosecond laser-induced breakdown in dielectrics.* Physical Review B **53**, 1749–1761 (1996).

[63] M. Lenzner, J. Krüger, S. Sartania, Z. Cheng, C. Spielmann, G. Mourou, W. Kautek, F. Krausz. *Femtosecond Optical Breakdown in Dielectrics.* Physical Review Letters **80**, 4076–4079 (1998).

[64] M. Lenzner, F. Krausz, J. Krüger, W. Kautek. *Photoablation with sub-10 fs laser pulses.* Applied Surface Science **154-155**, 11–16 (2000).

[65] T. Apostolova, Y. Hahn. *Modeling of laser-induced breakdown in dielectrics with subpicosecond pulses.* Journal of Applied Physics **88**, 1024 (2000).

[66] J. Jasapara, A. Nampoothiri, W. Rudolph, D. Ristau, K. Starke. *Femtosecond laser pulse induced breakdown in dielectric thin films.* Physical Review B **63**, 045117 (2001).

[67] M. Mero, B. Clapp, J. C. Jasapara, W. Rudolph, D. Ristau, K. Starke, J. Krüger, S. Martin, W. Kautek. *On the damage behavior of dielectric films when illuminated with multiple femtosecond laser pulses.* Optical Engineering **44**, pages (2005).

[68] M. Mero, J. Liu, W. Rudolph, D. Ristau, K. Starke. *Scaling laws of femtosecond laser pulse induced breakdown in oxide films.* Physical Review B **71**, 115109 (2005).

[69] M. Jupé, L. Jensen, A. Melninkaitis, V. Sirutkaitis, D. Ristau. *Calculations and experimental demonstration of multi-photon absorption governing fs laser-induced damage in titania.* Optics Express **17**, 12269 (2009).

[70] A. Melninkaitis, T. Tolenis, L. Mažule, J. Mirauskas, V. Sirutkaitis, B. Mangote, X. Fu, M. Zerrad, L. Gallais, M. Commandré, S. Kičas, R. Drazdys. *Characterization of zirconia- and niobia-silica mixture coatings produced by ion-beam sputtering.* Applied Optics **50**, C188–C196 (2011).

[71] D. N. Nguyen, L. A. Emmert, P. Schwoebel, D. Patel, C. S. Menoni, M. Shinn, W. Rudolph. *Femtosecond pulse damage thresholds of dielectric coatings in vacuum.* Optics Express **19**, 5690–5697 (2011).

[72] B. Mangote, L. Gallais, M. Commandré, M. Mende, L. Jensen, H. Ehlers, M. Jupé, D. Ristau, A. Melninkaitis, J. Mirauskas, V. Sirutkaitis, S. Kičas, T. Tolenis, R. Drazdys. *Femtosecond laser damage resistance of oxide and mixture oxide optical coatings.* Optics Letters **37**, 1478–1480 (2012).

[73] M. Mende, S. Schrameyer, H. Ehlers, D. Ristau, L. Gallais. *Laser damage resistance of ion-beam sputtered Sc2O3/SiO2 mixture optical coatings.* Applied Optics **52**, 1368–1376 (2013).

[74] J. C. Jasapara. *Characterization of a femtosecond laser and its application to the study of breakdown in dielectric thin films.* PhD thesis, The University of New Mexico (2001).

[75] C. B. Schaffer. *Interaction of Femtosecond Laser Pulses with Transparent Materials.* PhD thesis, Harvard University (2001).

[76] M. Mero. *Femtosecond Laser Induced Breakdown in Dielectric Films.* PhD thesis, The University of New Mexico (2005).

[77] E. Jones, T. E. Oliphant, P. Peterson. *SciPy: Open source scientific tools for Python.* (2014) `http://www.scipy.org/` (visited on 03/19/2014).

[78] T. E. Oliphant. *Python for Scientific Computing.* Computing in Science & Engineering **9**, 10–20 (2007).

[79] S. D. Team. *SymPy: Python library for symbolic mathematics.* (2014) `http://www.sympy.org/` (visited on 03/19/2014).

[80] J. D. Hunter. *Matplotlib: A 2D Graphics Environment.* Computing in Science and Engineering **9**, 90–95 (2007).

[81] F. Perez, B. E. Granger. *IPython: A System for Interactive Scientific Computing.* Computing in Science and Engineering **9**, 21–29 (2007).

[82] W. A. Stein. *Sage Mathematics Software.* (2014) `http://www.sagemath.org/` (visited on 03/19/2014).

[83] J. D. Jackson. *Classical Electrodynamics.* 3rd ed. (Wiley, New York, 1999). ISBN: 047130932X.

[84] R. W. Boyd. *Nonlinear Optics.* 3rd ed. (Academic Press, Amsterdam ; Boston, 2008). 613 pp. ISBN: 9780123694706.

[85] A. E. Siegman. *Lasers* (University Science Books, Mill Valley, California, 1986). ISBN: 9780935702118.

[86] H. A. Macleod. *Thin-Film Optical Filters.* 4th ed. Optics and optoelectronics (CRC Press, Boca Raton, 2010). ISBN: 9781420073027.

[87] S. A. Furman, A. V. Tikhonravov. *Basics of Optics of Multilayer Systems* (Editions Frontières, Gif-sur-Yvette, France, 1992). ISBN: 9782863321102.

[88] L. V. Keldysh. *Ionization in the field of a strong electromagnetic wave*. Soviet Physics JETP **20**, 1307 (1965).

[89] V. Pervak, O. Razskazovskaya, I. B. Angelov, K. L. Vodopyanov, M. Trubetskov. *Dispersive mirror technology for ultrafast lasers in the range 220–4500 nm*. Advanced Optical Technologies **3**, 55–63 (2014).

[90] F. Gires, P. Tournois. *Interféromètre utilisable d'impulsions lumineuses modulées en fréquence*. Comptes Rendus de l'Académie des Sciences Paris, 6112–6115 (1964).

[91] V. Pervak, I. Ahmad, S. A. Trushin, Z. Major, A. Apolonski, S. Karsch, F. Krausz. *Chirped-pulse amplification of laser pulses with dispersive mirrors*. Optics Express **17**, 19204–19212 (2009).

[92] R. Szipőcs, A. Kőházi-Kis. *Theory and design of chirped dielectric laser mirrors*. Applied Physics B: Lasers and Optics **65**, 115–135 (1997).

[93] T. V. Amotchkina, M. K. Trubetskov, V. Pervak, B. Romanov, A. V. Tikhonravov. *On the reliability of reverse engineering results*. Applied Optics **51**, 5543–5551 (2012).

[94] W. H. Knox, N. M. Pearson, K. D. Li, C. A. Hirlimann. *Interferometric measurements of femtosecond group delay in optical components*. Optics Letters **13**, 574–576 (1988).

[95] K. Naganuma, K. Mogi, H. Yamada. *Group-delay measurement using the Fourier transform of an interferometric cross correlation generated by white light*. Optics Letters **15**, 393–395 (1990).

[96] W. H. Knox. *Dispersion measurements for femtosecond-pulse generation and applications*. Applied Physics B **58**, 225–235 (1994).

[97] A. Gosteva, M. Haiml, R. Paschotta, U. Keller. *Noise-related resolution limit of dispersion measurements with white-light interferometers*. Journal of the Optical Society of America B **22**, 1868–1874 (2005).

[98] D. Grupe. *Measuring Group Delay Dispersion in the UV-VIS-IR range by White-Light Interferometry*. Diplomarbeit, Ludwig-Maximilians-Universität München (2008).

[99] T. V. Amotchkina, A. V. Tikhonravov, M. K. Trubetskov, D. Grupe, A. Apolonski, V. Pervak. *Measurement of group delay of dispersive mirrors with white-light interferometer*. Applied Optics **48**, 949–956 (2009).

[100] S. Diddams, J.-C. Diels. *Dispersion measurements with white-light interferometry*. Journal of the Optical Society of America B **13**, 1120–1129 (1996).

[101] K. Osvay, R. Szipőcs, G. Kurdi, J. Hebling, A. P. Kovács, Z. Bor. *Measurement of the group delay of laser mirrors by a Fabry-Perot interferometer*. Optics Letters **20**, 2339–2341 (1995).

[102] M. K. Trubetskov, M. Pechmann, I. B. Angelov, K. L. Vodopyanov, F. Krausz, V. Pervak. *Measurements of the group delay and the group delay dispersion with resonance scanning interferometer*. Optics Express **21**, 6658–6669 (2013).

[103] M. Pechmann. *Resonance Scanning Interferometer for Group Delay Dispersion Measurements*. Diplomarbeit, Ludwig-Maximilians-Universität München (2013).

[104] M. Born, E. Wolf. *Principles of Optics: Electromagnetic Theory of Propagation, Interference and Diffraction of Light.* 7th expanded ed. (Cambridge University Press, Cambridge, New York, 1999). 952 pp. ISBN: 0521642221.

[105] A. N. Tikhonov. *Solutions of ill-posed problems.* In collab. with V. I. Arsenin. Scripta series in mathematics (Winston ; distributed solely by Halsted Press, Washington : New York, 1977). 258 pp. ISBN: 0470991240.

[106] J. H. Ahlberg, E. N. Nilson, J. L. Walsh. *The Theory of Splines and Their Applications* (Academic Press, New York, 1967). ISBN: 9780080955452.

[107] NIST. *Spectrophotometry.* National Institute of Standards and Technology (NIST). `http://www.nist.gov/pml/div685/grp03/spectrophotometry.cfm` (visited on 02/12/2014).

[108] D. Z. Anderson, J. C. Frisch, C. S. Masser. *Mirror reflectometer based on optical cavity decay time.* Applied Optics **23**, 1238–1245 (1984).

[109] A. Hordvik. *Measurement techniques for small absorption coefficients: recent advances.* Applied Optics **16**, 2827–2833 (1977).

[110] T. C. International Organization for Standardization. *ISO 11551: Test Method for Absorptance of Optical Laser Components.* 1997.

[111] K. Starke. *Ubertragung von Standardmessverfahren zur Charakterisierung optischer Beschichtungen in den Bereich ultrakurzer Laserpulse.* PhD thesis, Universität Hannover (2004).

[112] A. Rosenfeld, M. Lorenz, R. Stoian, D. Ashkenasi. *Ultrashort-laser-pulse damage threshold of transparent materials and the role of incubation.* Applied Physics A: Materials Science & Processing **69**, S373–S376 (1999).

[113] D. Nguyen, L. A. Emmert, I. V. Cravetchi, M. Mero, W. Rudolph, M. Jupe, M. Lappschies, K. Starke, D. Ristau. $Ti_xSi_{1-x}O_2$ *optical coatings with tunable index and their response to intense subpicosecond laser pulse irradiation.* Applied Physics Letters **93**, 261903 (2008).

[114] A. Melninkaitis, J. Mirauskas, V. Sirutkaitis. *Adaptive laser-induced damage detection.* In Proceedings of SPIE, Vol. 7504, 75041F (2009). Edited by G. J. Exarhos, V. E. Gruzdev, D. Ristau, M. J. Soileau, and C. J. Stolz.

[115] D. Ashkenasi, M. Lorenz, R. Stoian, A. Rosenfeld. *Surface damage threshold and structuring of dielectrics using femtosecond laser pulses: the role of incubation.* Applied Surface Science **150**, 101–106 (1999).

[116] M. Lenzner, J. Krüger, W. Kautek, F. Krausz. *Incubation of laser ablation in fused silica with 5-fs pulses.* Applied Physics A **69**, 465–466 (1999).

[117] I. B. Angelov, A. Conta, S. A. Trushin, Z. Major, S. Karsch, F. Krausz, V. Pervak. *Investigation of the laser-induced damage of dispersive coatings.* In Proceedings of SPIE, Vol. 8190, 81900B (2011). Edited by G. J. Exarhos, V. E. Gruzdev, J. A. Menapace, D. Ristau, and M. J. Soileau.

[118] I. B. Angelov. *Manuscript submitted to Ludwig-Maximilians-Universitaet Muenchen.* 2013.

[119] A. Conta. *Characterization of the laser induced damage threshold of mirrors in the ultra short pulse regime.* BSc thesis, Hochschule München (2010).

[120] I. Ahmad, S. A. Trushin, Z. Major, C. Wandt, S. Klingebiel, T.-J. Wang, V. Pervak, A. Popp, M. Siebold, F. Krausz, S. Karsch. *Frontend light source for short-pulse pumped OPCPA system*. Applied Physics B **97**, 529–536 (2009).

[121] K. Yoshimura, T. Miki, S. Iwama, S. Tanemura. *Characterization of niobium oxide electrochromic thin films prepared by reactive d.c. magnetron sputtering*. Thin Solid Films **281-282**, 235–238 (1996).

[122] F. X. Kärtner, U. Morgner, R. Ell, T. Schibli, J. G. Fujimoto, E. P. Ippen, V. Scheuer, G. Angelow, T. Tschudi. *Ultrabroadband double-chirped mirror pairs for generation of octave spectra*. Journal of the Optical Society of America B **18**, 882–885 (2001).

[123] M. Jupé, M. Lappschies, L. Jensen, K. Starke, D. Ristau. *Improvement in laser irradiation resistance of fs- dielectric optics using silica mixtures*. In Proceedings of SPIE, Vol. 6403, 64031A (2006). Edited by G. J. Exarhos, A. H. Guenther, K. L. Lewis, D. Ristau, M. J. Soileau, and C. J. Stolz.

[124] D. Milam. *Laser-induced damage at 1064 nm, 125 psec*. Applied Optics **16**, 1204–1213 (1977).

[125] I. B. Angelov, M. Pechmann, M. K. Trubetskov, F. Krausz, V. Pervak. *Optical breakdown of multilayer thin-films induced by ultrashort pulses at MHz repetition rates*. Optics Express **21**, 31453–31461 (2013).

[126] A. O'Keefe, D. A. G. Deacon. *Cavity ring-down optical spectrometer for absorption measurements using pulsed laser sources*. Review of Scientific Instruments **59**, 2544 (1988).

[127] A. V. Tikhonravov, M. K. Trubetskov. *OptiLayer thin-film software*. `http://www.optilayer.com/` (visited on 03/19/2014).

[128] J. H. Apfel. *Optical coating design with reduced electric field intensity*. Applied optics **16**, 1880–1885 (1977).

[129] C. Y. Teisset. *Few-Cycle High-Repetition-Rate Optical Parametric Ampliers And Their Synchronisation Schemes*. PhD thesis, Technischen Universität Berlin (2009).

[130] R. Trebino, K. W. DeLong, D. N. Fittinghoff, J. N. Sweetser, M. A. Krumbügel, B. A. Richman, D. J. Kane. *Measuring ultrashort laser pulses in the time-frequency domain using frequency-resolved optical gating*. Review of Scientific Instruments **68**, 3277–3295 (1997).

[131] H. G. Tompkins and E. A. Irene, eds. *Handbook of Ellipsometry* (Springer, Norwich, NY : Heidelberg, Germany, 2005). 870 pp. isbn: 0815514999.

[132] V. Mikhelashvili, G. Eisenstein. *Optical and electrical characterization of the electron beam gun evaporated TiO2 film*. Microelectronics Reliability **41**, 1057–1061 (2001).

[133] O. Arnon, P. Baumeister. *Electric field distribution and the reduction of laser damage in multilayers*. Applied Optics **19**, 1853–1855 (1980).

[134] G. Abromavicius, R. Buzelis, R. Drazdys, A. Melninkaitis, V. Sirutkaitis. *Influence of electric field distribution on laser induced damage threshold and morphology of high reflectance optical coatings*. In Proceedings of SPIE, Vol. 6720, 67200Y (2007). Edited by G. J. Exarhos, A. H. Guenther, K. L. Lewis, D. Ristau, M. J. Soileau, and C. J. Stolz.

# Acronyms

**EB** electron beam evaporation. 42, 54

**EFI** Electric FIeld optimized mirror (a design name). 54, 56, 63, 64, 66, 68, 69

**FROG** frequency-resolved optical gating. 58

**GD** group delay. 7, 14–25, 27, 67

**GDD** group delay dispersion. 7, 14–18, 22–27, 29, 46, 49, 64

**GTI** Gires-Tournois interferometer. 14, 15, 18

**GV** group velocity. 7

**GVD** group velocity dispersion. 7

**LIDT** laser-induced damage threshold. 3, 4, 31, 35, 41, 42, 47, 48, 50, 51, 54, 61, 64–69

**LOT** Low-index layer On Top (a design name). 64

**MPI** multiphoton ionization. 10, 11, 50

**MS** magnetron sputtering. 42, 54

**NBP** Narrow-Band Pass filter (a design name). 54–56, 61, 62, 66, 68

**NIR** near ifrared. 10

**OPA** optical parametric amplification. 2, 53

**ppm** parts per million ($2\,\text{ppm} = 2 \times 10^{-6}$). 31

**QWOT** quarter-wave optical thickness. 41, 43, 48, 50, 51, 54–56, 59–68

**RMS** root mean square. 29

**RSI** Resonance Scanning Interferometer. 18, 22–27, 67, 69

**SLAE** system of linear algebraic equations. 21, 22

**WLI** white-light interferometer. 17, 18, 22–27, 67, 69

# Acknowledgments

During my stay in Garching, I have had the chance to meet and work with extraordinary people. Here, I would like to express my gratitude to all these colleagues and friends who have helped me with my work or who have otherwise significantly influenced my life in a positive way.

First and foremost, I would like to thank Prof. Ferenc Krausz for giving me the privilege to pursue my PhD in his group at the Max-Planck-Institute of Quantum Optics, thereby providing me access to a world-class scientific environment. I was often inspired by his ability to coordinate so many different projects, stay up-to-date with all of them, and give competent and insightful ideas to each one.

I am in great debt of my direct advisor and friend Vladimir Pervak, who, starting from day zero, was always there for me. His door was ever open for discussions of arbitrary type—from scientific disputes to friendly advices. Moreover, his help and guidance had a great impact on my work. I am also thankful to Vladimir for conveying so much of his professional and personal experience. His assistance in adapting to the life in Germany was invaluable, as were his constant support and his great patience with a stubborn fellow like me. And I will always remember the countless evenings spent together on the ice rink, in the gym, or in the boulder hall.

Next I wish to thank Olga Razskazovskaya for her help in the preparation of many of the studied samples. But I am even more grateful to her for the numerous of useful advices and fruitful conversations about science, life, and everything else; for the many days spent hiking or skiing in the Alps; for the trips to distant cities; as well as for sparkling my desire to travel. You added much joy to my life here in Munich, thank you!

Many thanks also to Michael Trubetskov for all the scientific discussions and theoretical advices, as well as for the number of modifications he introduced to the practical OptiLayer software in order to meet my specific needs. This allowed me to focus on the more on the essential part of my research.

I also received some additional theoretical support from Vladislav Yakovlev, who was always ready to share his knowledge. I also enjoyed hacking around with his ACD software. This activity not only exercised my programming skills, but also gave me insight into various optimization algorithms.

In the lab, I had the chance to learn from young, but gifted and highly motivated experimentalists. Aaron von Conta introduced me to the concepts of optical breakdown.

His set-up and the ideas behind it underlaid all damage threshold measurements carried out in this work. Oleg Pronin thought me how to operate and to maintain the Yb:YAG thin-disk oscillator in my lab.

I am very grateful to Elena Fedulova and Maximilian von Pechmann for carrying out quite a few measurements of absorption, losses, and dispersion on my behalf. Additionally, I thank Maximilian for the number of insightful conversations we have had and also Lena for being such a nice and responsible flat mate.

I would like to thank Sergei Trushin, Alexander Kessel, and Christoph Skrobol from the PFS project for allowing me to work with their system, and for the time they have spent preparing it for me. I also thank Zsuzsanna Major, Helena Barros, Martin Gorjan, Moritz Ueffing, and Lenard Vamos from LEX for the given opportunity to use their regenerative amplifier for my measurements.

I received great help with administrative and bureaucratic matters from Klaus Franke, Katharina Adler, Franziska Hoss, Ramona Neulinger, Martin Groß, and Mrs. Wild.

Special thanks to Alexander Gliserin for his help with my German, his sarcastic humor, and for all the amusements, especially the quaking ones.

I have also had uncountable number of interesting and exciting discussions on a wide variety of topics with: Fabian Lücking, Simon Holzberger, Daniel Kreier, Kellie Pearce, Henning Karstens, Waldemar Schneider, Nikolai Lilienfein, Marcus Seidel, Jonathan Brons, Sabine Keiber, Matthias Kübel, Henning Carstens, Florian Habel, Matt Walbran, Elisabeth Bothschafter, and Hanieh Fattahi.

The group of Prof. Krausz is so large, that most certainly I am missing someone in the list above. Hence, I would like to thank all colleagues for the stimulating and friendly environment.

Finally, I am grateful to my family for always encouraging my curiosity, stimulating my hunger for knowledge, and for supporting me throughout all these years.